# INVESTIGATION INTO USING LIQUID CRYSTAL THERMOGRAPHY AS PRIMARY TEMPERATURE MEASUREMENT TECHNIQUE FOR OBTAINING LOCAL WALL TEMPERATURES AND HEAT TRANSFER COEFFICIENTS IN TUBE-IN-TUBE HEAT EXCHANGERS.

Jacob E. van der Westhuizen

UP student number: 28043767

Study leaders:

Dr Jaco Dirker and Prof Josua P. Meyer

*Submitted in partial fulfilment of the requirements for the degree*

MASTER OF ENGINEERING

*in the*

Department of Mechanical and Aeronautical Engineering

Faculty of Engineering, Built Environment and Information Technology

University of Pretoria

November 2014

UNIVERSITEIT VAN PRETORIA
UNIVERSITY OF PRETORIA
YUNIBESITHI YA PRETORIA

## Abstract

The feasibility of obtaining local wall temperatures by using liquid crystal thermography (LCT) in a counter-flow tube-in-tube heat exchanger was investigated. Local annulus-side heat transfer coefficients at the inlet and thermodynamically and hydrodynamically underdeveloped regions were also obtained while operating at steady conditions.

The heat transfer coefficients of the tube-in-tube heat exchanger are, however, disputed in the literature, as conflicting sources are easily found. In most literature sources the problem is simplified by assuming constant heat transfer coefficients throughout the length of the heat exchanger and the boundary layer growth is generally ignored at inlet regions.

Thermocouples pose practical problems when measuring temperatures in heat exchangers. LCT is investigated as alternative surface temperature measurement technique. This study aims to develop a methodology for directly measuring wall temperatures inside a tube-in-tube heat exchanger. These temperatures were further used to calculate local heat transfer coefficients.

In this study, a 1m long tube-in-tube test section with an annulus diameter ratio of 0.54 (ratio of the inner wall of the annulus to its outer wall) was constructed, in which liquid crystal thermography was employed as an alternative wall temperature measurement technique to thermocouples. Temperature-sensitive paint was applied to the inner wall of the annulus in order to measure the wall temperatures non-intrusively. Complete temperature maps could be constructed for different thermal conditions which indicated differences of up to 10 °C in wall temperature at the inlet regions, which would have been difficult to capture with thermocouples. This study covered a total of nine different annular flow and thermal conditions for cooled and heated cases. The annular flow conditions ranged from laminar (Re = 1000) flow to fully turbulent flow (Re = 13 800).

In general, the heat transfer coefficients were found not to be constant along the length of the heat exchanger. The averaged heat transfer coefficients at the inlet were compared with existing correlations in the literature for full-length heat exchangers and were found to be higher by an average of 44 % over the data presented. Uncertainties on the local heat transfer coefficient were found to be approximately 80% for the cooled annulus cases and 45% for a heated annulus. This was mostly due to the practical laboratory restrictions imposed by fluid temperature limits.

It was found that liquid crystal thermography could be used successfully for directly measuring the wall temperatures of tube-in-tube heat exchangers with very low surface temperature uncertainties (0.03 °C). With the approach developed in this study, a method was found for determining local heat transfer coefficients without introducing wall thermocouples or any other disturbances in the passage of the annular fluid.

Publications resulting from this investigation:

**JE van der Westhuizen**, J Dirker, JP Meyer. *"Investigation of heat transfer and temperature profiles at inlets and undeveloped flow regions using liquid crystal thermography"*, Proceedings of the 2nd Southern Africa Solar Energy Conference (SASEC 2014), Port Elizabeth, South Africa, Paper Number 16, 26 – 29 January 2014

**JE van der Westhuizen**, J Dirker, JP Meyer. *"Investigation into using liquid crystal thermography for measuring heat transfer and temperature profiles at inlets and underdeveloped regions"*, Proceedings of the 10th International Conference on Heat Transfer, Fluid Mechanics and Thermodynamics (HEFAT 2014), Orlando, Florida, USA, Paper Number 1569878271, 14-16 July 2014.

A journal article manuscript based on the study has been submitted to Experimental Heat Transfer for review (Submission number: UEHT – 2014 – 0107):

**JE van der Westhuizen**, J Dirker, JP Meyer. "*Implementation of Liquid Crystal Thermography to Determine Wall Temperatures and Heat Transfer Coefficients in a Tube-in-Tube Heat Exchanger*".

Acknowledgements:

To God. For giving me the opportunity and ability to develop my talents and interests.

My family and friends. For their keen interest in my studies and for always asking how it is going.

My fellow “Fishbowl” students. For turning a long workday into a pleasant experience. For always lending an ear when tough problems needed simple solutions.

Dr Dirker. The calm and patient manner in which you guided me throughout this study is inspired. For hours of stimulating discussions and the needed support and knowledge.

Prof. Meyer. Thank you for accepting me to study in your Thermofluids group and providing me with a much-needed bursary.

The funding obtained from the NRF, TESP, University of Stellenbosch/ University of Pretoria, SANERI/SANDENI, CSIR, EEDSM Hub and NAC is gratefully acknowledged and deeply appreciated.

# Nomenclature

| Symbol | Quantity | SI Units |
|---|---|---|
| $A$ | Area | $m^2$ |
| $a$ | Annular diameter ratio | dimensionless |
| $B$ | Bias of measurement equipment | dimensionless |
| $Bw$ | Bandwidth | °C |
| $C_p$ | Heat capacity (specific heat) | J/kgK |
| $CV$ | Control Volume | |
| $D$ | Diameter | m |
| $D_h$ | Hydraulic diameter | m |
| $eb$ | Energy balance | % |
| $F$ | Force | N |
| $f$ | Friction coefficient | dimensionless |
| $H, S, Val$ | HSV (Hue, Saturation, Value colour system) | degrees, -, - |
| $h$ | Convective heat transfer coefficient | $W/m^2K$ |
| $k$ | Thermal conductivity | W/mK |
| $L$ | Length | m |
| $M$ | Mass | kg |
| $\dot{m}$ | Mass flow rate | kg/s |
| $n$ | Number of samples | dimensionless |
| $Nu$ | Nusselt number | dimensionless |
| $P$ | Precision of measurement instrument | dimensionless |
| $Pr$ | Prandtl number | dimensionless |
| $\dot{Q}$ | Heat transfer rate | W |
| $\dot{q}$ | Heat flux | $W/m^2$ |
| $R$ | Thermal resistance | K/W |
| $R, G, B$ | RGB (Red, Green, Blue colour system) | dimensionless |
| $Re$ | Reynolds number | dimensionless |
| $S$ | Result of measurement | dimensionless |
| $SE_x$ | Standard error | |
| $s$ | Standard deviation of sample | |
| $T$ | Fluid temperatures | °C |
| $T_a$ | Annulus fluid temperature | °C |
| $T_{ii}$ | Inner fluid temperature | °C |
| $T_w$ | Wall temperatures | °C |
| $t$ | Time | s |
| $U$ | Overall heat transfer coefficient | $W/m^2K$ |
| $u$ | Velocity | m/s |
| $V$ | Volume | $m^3$ |
| $\dot{V}$ | Volume flow rate | $m^3/s$ |
| $x$ | Uncertainty entity Measurement | dimensionless |

| **Greek symbols** | | |
|---|---|---|
| $\tau$ | Thickness | m |
| $\delta$ | Uncertainty | |
| $\theta$ | Angle (plane) | degrees |
| $\mu$ | Dynamic viscosity | kg/ms |
| $\rho$ | Density | $kg/m^3$ |
| $\nu$ | Kinematic viscosity | $m^2/s$ |

| **Subscripts** | |
|---|---|
| $a$ | Annulus fluid |
| $b$ | Bulk fluid |
| CA | Related to a cooled annulus |
| $c$ | Cross-sectional |
| $cond$ | Conductive property |
| $conv$ | Convective property |
| $f$ | Fluid |
| HA | Related to a heated annulus |
| $h$ | Hydraulic dimension |
| $hx$ | Relating to the whole heat exchanger |
| $j, 1,2,3\ etc.$ | Control volume (CV) designation |
| $ii$ | Inner tube fluid property |
| $in$ | Inlet |
| $out$ | Outlet |
| $w$ | Wall |

# Contents

# List of Figures

# List of Tables

# Chapter 1: Introduction

## 1.1. Background

Heat transfer is an important phenomenon and occurs whenever there is a difference in temperature between two entities. It plays a crucial role in modern technology and in nature. Only a few modern processes or devices do not require adequate thermal management for proper operation. For that reason it is vital to understand heat transfer sufficiently and consider it correctly. Heat exchangers are often used to transfer heat and their use has been recorded in history since the early 1800s. Heat exchanger devices were vital for the development of the thermodynamic cycles. Most notable were those by Sadi Carnot as documented in his book: “Reflections on the Motive Power of Fire” in 1824, which relied on heat transferred to and/or from a fluid.

Of the three heat transfer modes (namely conduction, convection and radiation), conductive and convective heat transfer are important in the majority of fluid-based heat exchangers. There are several types of heat exchangers, ranging in size from a heat sink in a cellular telephone to a condenser used in power stations designed to transfer heat at significantly higher rates. Without the development of heat exchangers, much modern equipment, including power plants, automobiles or even personal computers, would not function.

One specific type of heat exchanger, the tube-in-tube heat exchanger, is widely used in various industries as this type is relatively inexpensive to build and to maintain. These heat exchangers usually consist of two tubes of different diameters, where the one is placed approximately concentrically inside the other. The passage between the two tubes forms the annulus, and along with the inner tube, there are flow paths for the heat transfer media (water, glycerine, salt solutions, etc.). Heat is thus exchanged between the two fluids of different temperatures across the wall of the inner tube, without the two media mixing.

The quantities for measuring the performance of heat transfer in certain geometries are readily described by the convective heat transfer coefficient. It is defined as the rate of heat transferred per unit of surface area per unit of temperature difference between the heat transfer surface and the bulk temperature of the fluid. The higher the convective heat transfer coefficient value, the better the performance of the heat exchanger. Experimental values obtained for the heat transfer coefficient, also described by means of the dimensionless Nusselt number, may be used in the design of a heat exchanger fit for a specific task or heat transfer requirements.

The magnitude of the heat transfer coefficient to be expected for a particular geometry and operating condition is often described by means of correlations based on experimental results. Such correlations enable thermal designers to properly size the heat exchangers. For

that reason it is essential to have accurate and trustworthy data from which such correlations can be derived.

Unfortunately, heat transfer data and correlations in the existing literature for heat exchangers are not always in agreement. Publications have been found with conflicting descriptions of heat transfer coefficients and correlations, which can show large discrepancies from one study to another. Most of the investigations in the literature only focus on the overall heat transfer performance, based on the entire length of a heat exchanger and disregard what happens on a point-to-point basis inside the heat exchanger. The reason is that it is relatively difficult to take measurements of local bulk fluid and wall temperatures. As a result, most of the correlations in the literature, especially for the annular side of tube-in-tube heat exchangers, make predictions for “effective” semi-constant heat transfer coefficients, disregarding the entrance lengths and the impact of the inlet configuration.

It is known that the heat transfer coefficient does not stay constant along the length of the heat exchanger because the fluid is bound by the no-slip boundary condition against a stationary wall [1]. This behaviour can be described by the boundary layer theory presented by Ludwig Prandtl in 1904. The dimensionless number named after him describes the ratio of the viscous diffusion rate (convective or mixing heat transfer through the fluid) against the thermal diffusion rate (conduction heat transfer through the fluid). As the boundary layer grows due to the no slip boundary condition, the slower moving fluid contained inside the boundary layer reduces the heat transfer ability, because the heat transfer at the boundary is more reliant on the (weaker) thermal conductance of the fluid.

Some temperature measurements of the fluid as well as the heat transfer surface are required in order to capture the effects of the boundary layer at the inlet and at regions where the boundary layer is not yet fully developed. Traditionally, thermocouples are used to measure the temperature of the bulk fluid temperature and, if applicable, also to measure approximately the surface temperature on the heat transfer wall. However, when measuring any observable quantity in a system, such as temperature, the presence of the measuring device alters the system in respect of its normal operation.

If one considers thermocouples, these measuring probes affect the system (for instance the heat exchanger operation) as follows: Firstly, the thermocouple wires introduced into the heat exchanger can be disruptive to the natural flow of the medium inside the heat exchanger and the convective heat transfer ability of the surfaces under consideration. Secondly, the thermocouple wires conduct heat through their own conductors to or from the junction where the temperature is measured, altering the local temperature and therefore the measured temperature value. Based on these weaknesses, alternative techniques for measuring surface temperature should also be considered.

One alternative measurement technique is that of thermal imaging, which relies on the infrared radiation emitted from a body with a known local emissivity. This is, however, not feasible for use in a water-based heat exchanger as these systems are unable to detect infrared radiation through a body of water. Infrared thermography is only able to register the surface temperatures of the surface closest to it even if that surface happens to be visually transparent. A regular pane of glass, for example, will always appear as the ambient temperature, even if something at a different temperature is located behind it [2].

Liquid crystal thermography (LCT) is another temperature measurement technique with similar results to those of a thermal imaging camera. LCT is a technique for obtaining local temperature values by using thermochromic liquid crystals (TLC). TLCs are temperature-sensitive and change their reflected colour as a function of the crystal's temperature when viewed in the presence of white light. Images containing a captured colour field on the surface of the model can be obtained and these colours can then be interpreted as temperature values [3].

TLCs have been used to measure temperatures as part of heat transfer studies on horizontal micro tubes, plate and fin heat exchangers as well as other heat exchanger and general flow geometries. Reasonable temperature uncertainties can be achieved when using TLC for surface temperature measurements, comparable to and in some cases even better than the accuracy of thermocouples. Surface temperature measurement paint containing TLCs can be applied onto practically any surface of interest. By capturing photographs of such surfaces, local wall temperatures and temperature distributions may be obtained.

## 1.2. Problem statement

The problem statement considered in this study can be summarised as follows:

- Current correlations for heat transfer do not necessarily take into account local heat transfer data, including wall temperatures, especially at those inlet regions where flow is thermally developing.
- Measuring localised wall temperatures in heat exchangers poses a practical problem and an alternative local temperature measurement technique to thermocouples should be sought.

## 1.3. Research objectives

The research objectives of this study can be summarised as follows:

- To implement and develop a methodology for using LCT for direct surface temperature measurements for the inner tube of a tube-in-tube heat exchanger.
- To use the surface temperature data to calculate localised heat transfer data at the inlet and underdeveloped regions of the heat exchanger.
- To develop a data analysis sequence in order to present interpretable, useful data and trends derived from the above methodologies.

## 1.4. Dissertation statement

Growing boundary layers suggest that the inlet region of a tube-in-tube heat exchanger has higher heat transfer capabilities than those that are traditionally stated in the literature from correlations. The hypothesis investigated in this paper is therefore as follows:

It is possible to determine the wall temperature distributions with reasonable accuracy using LCT in order to calculate local heat transfer coefficients.

## 1.5. Delineation and limitations

- Only the annular passage heat transfer of a traditional tube-in-tube heat exchanger will be investigated, with liquid water as the working fluid.
- Only wall temperatures between 20 °C and 40 °C will be considered.

## 1.6. Significance of the study

The significance of the study lies in showcasing and implementing a wall temperature measurement technique as an alternative to thermocouples, which may be used to obtain more reliable trends for heat transfer in heat exchangers, which in turn may be used to design more cost-effective and space-efficient heat exchangers.

## 1.7. Chapter overview of the dissertation

Chapter 2 gives details of the literature review, with a brief overview of the basic theories at play in this investigation. This chapter covers topics such as: the boundary layer theory, previous work in annulus heat transfer for tube-in-tube heat exchangers, and the applications and use of TLCs.

Chapter 3 describes the experimental setup in detail. Aspects such as the experimental facility, the design and construction process and all the required sub-systems are discussed. Also discussed here are all the test cases as well as the data capturing procedure followed.

Chapter 4 covers the data analysis procedure. This chapter details the post-processing of the data gathered during the testing procedure. This includes interpreting the photographs captured of the TLC surface and the reduction thereof. The chapter also covers the mathematics behind determining all the heat transfer coefficients, and describes how to estimate the heat transfer coefficients of the inner tube and the uncertainties thereof.

Chapter 5 presents the experimental results of the heat exchanger data gathered.

Chapter 6 summarises the findings and contributions made in this investigation, along with recommendations for future research relating to the current topic.

Appendix A contains details of an experiment conducted as part of this study to obtain the thermal conductivity of the resin system used in the heat exchanger.

Appendix B outlines the uncertainty principles used in the present study and shows detailed examples of the respective uncertainty calculations.

Appendix C presents the organised data sets obtained from this study.

Appendix D shows the calibration data for all the thermocouples used in this study.

# Chapter 2: Literature review

## 2.1. Introduction

This section presents the literature relevant to the topic of investigation. The techniques and methods available in the literature relating to the current study are discussed. This includes the phenomenon of heat transfer; the physical phenomena that influence it, how it is quantified as well as the techniques used to estimate it.

The literature review is structured as follows:

- Convection heat transfer and boundary layer effects
- Previous annulus heat transfer investigations
- Previous work relating to local heat transfer
- LCT as temperature measurement technique
- Previous work using LCT for heat transfer research
- Short summary

## 2.2. Boundary layer

Boundary layers are formed when slow moving particles are close to a stationary surface. These boundary layers form due to the non-slip boundary condition present on the surface [1]. This boundary layer also grows in thickness as the fluid flows along the surface because the adjacent molecules of the fluid slow one another down. This is called the velocity boundary layer. In a similar fashion, a thermal boundary layer is also developed when a fluid with a specified temperature flows over a surface which is at a different temperature. Figure 1 shows a schematic representation of what happens in the boundary layer for the unique case of Pr=1.

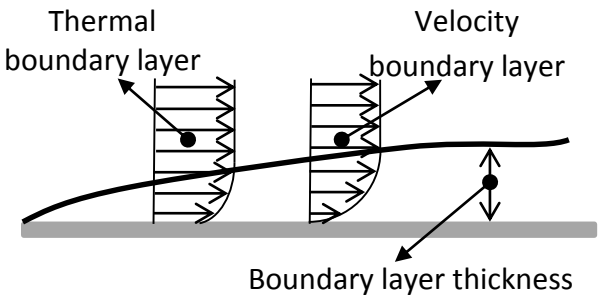


**Figure 1 – Schematic representation of the boundary layers**

The velocity of the boundary layer forces the fluid particles adjacent to the surface to a halt (non-slip boundary condition) with the result that those particles reach thermal equilibrium with the adjacent surface. These particles which have assumed the surface temperature then exchange energy with the particles adjacent to them, and so on. This illustrates that the heat transfer of the boundary layer is driven more by the fluid's ability to conduct heat than by convection.

The relative thickness of the boundary layer is best described by the Prandtl number ($Pr$) and is defined as follows [1]:

$$Pr = \frac{\text{Molecular diffusivity of Momentum}}{\text{Molecular diffusivity of heat}} = \frac{\mu C_p}{k} \qquad \textbf{Eq. 1}$$

The lower the Prandtl number, the thicker the thermal boundary layer. The Prandtl numbers for water at 20 °C and 40 °C are 7.01 and 5.43 respectively. The Prandtl number is therefore inversely related to water temperature. This means that the boundary layer becomes thicker as the water temperature increases. The Prandtl number may also be used to estimate the length of the entrance region (when the flow hydrodynamically and thermally developed) for a specific geometry.

## 2.3. Boundary layer and heat transfer coefficient

The growth of the boundary layer changes the velocity as well as the temperature distribution in the flow inside a pipe. Shown below is the variation the growth of the boundary layer introduces on the local heat transfer coefficient as well as the friction factor.

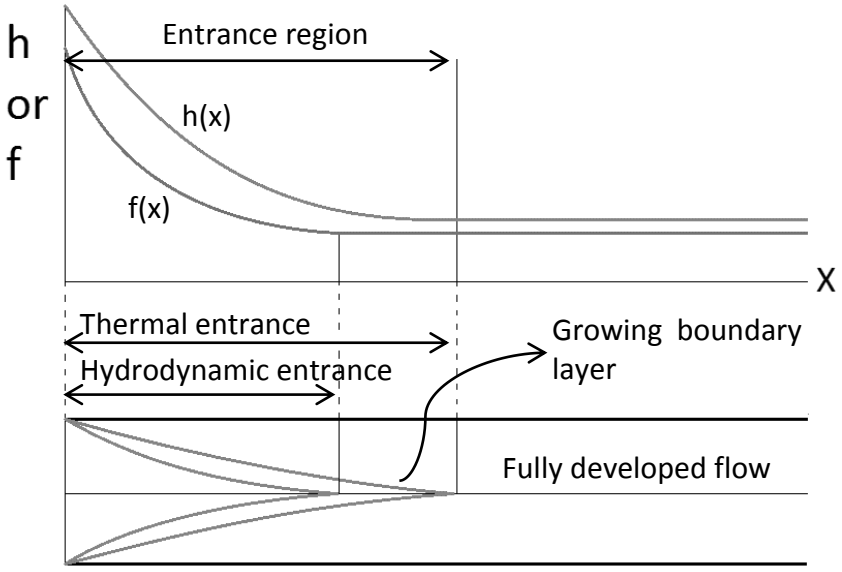


**Figure 2 - Variation of the friction factor and the convection heat transfer coefficient in the flow direction**

Figure 2 shows the difference between the hydrodynamically and the thermally developing flow phenomena. It also shows that after the entrance region the friction factor as well as the heat transfer coefficient stays constant. This is due to the boundary layer being fully developed and also staying constant. While the boundary layer is still relatively thin the heat transfer coefficient is large – becoming less as the boundary layer grows in thickness.

## 2.4. Previous work

Concentric tube heat exchangers have been studied for about a century. One well-known correlation was developed in 1930 by Dittus and Boelter and is still used today. Contained in this section is a brief review of past studies relating to this present study. This includes

studies on tube-in-tube heat exchangers as well as the use of LCT in water-based heat transfer studies. The basic layout of a tube-in-tube heat exchanger is shown in Figure 2:

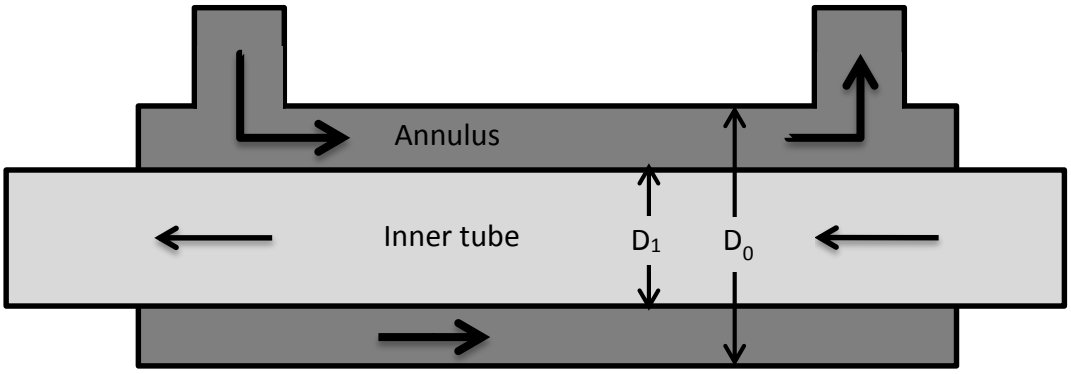


**Figure 3 – Basic layout of a tube-in-tube heat exchanger**

### 2.4.1. Tube-in-tube heat exchangers

There are many correlations for heat transfer coefficients in the literature. They are for different annular diameter ratios ($a = D_1/D_0$, inner wall diameter to outer wall diameter ratio), different flow rates, different working fluids, different thermal boundary conditions, etc. A selection of these is shown in Table 1. Because of the two walls present in the annulus, the diameter used in most correlations is stated as the hydraulic diameter, which is defined as: $D_h = D_0 - D_1$. All of these correlations contribute to the pool of data on heat exchangers, although not all of them correlate well with one another [1].

**Table 1 – Existing correlations for determining Nusselt numbers in annular passages**

| Author | Correlation | $a = D_1/D_0$ | $Re = \rho V D_h/\mu$ | Medium |
|---|---|---|---|---|
| Dirker and Meyer [4] | $Nu_{Dh} = C_o Re_{Dh}^{P} Pr^{1/3} \left(\frac{\mu}{\mu_w}\right)^{0.14}$<br>$P = 1.013e^{-0.0067/a}$<br>$C_o = (0.003a^{-1.86})/(0.063a^{-3} - 0.0674a^{-2} + 2.225/a - 1.157)$ | 0.3125-0.588 | 4 000-30 000 | Water |
| McAdams [5] | $Nu_{Dh} = 0.03105a^{-0.15}\,(1/a-1)^{0.2} Re_{Dh}^{0.8} Pr^{1/3} \left(\frac{\mu}{\mu_w}\right)_o^{0.14}$ | 0.00014-0.84 | Not specified | All |
| Dittus and Boelter [6] | $Nu_{Dh} = 0.023 Re_{Dh}^{0.8} Pr^{n}$, $n = 0.4$ for heating<br>$n = 0.3$ for cooling | Not specified | Not specified | Not specified |
| Gnielinski [7] | $Nu_{Dh} = \frac{\left(\frac{f}{8}\right)Re_{Dh}Pr_a}{\varphi + 12.7\sqrt{\frac{f}{8}}\left(Pr_a^{\frac{2}{3}}-1\right)}\left(1+\left(\frac{D_h}{L}\right)^{\frac{2}{3}}\right)F_{ann}K$<br>$\varphi = 1.07 + \frac{900}{Re_{Dh}} - \frac{0.63}{1+10Pr_a}$<br>$K = \left(\frac{Pr_a}{Pr_{iw}}\right)^{0.11}$ for liquids<br>$K = \left(\frac{T_b}{T_{iw}}\right)^{n}$ for gases and $n = 0$ for cooling<br>$n = 0.45$ with $0.5 < \frac{T_b}{T_{iw}} < 1.0$<br>$F_{ann} = 0.75a^{-0.17}$<br>$f = (1.8\,log_{10}\,Re^{*} - 1.5)^{-2}$<br>$Re^{*} = Re_{Dh}\frac{(1+a^2)\ln a + (1-a^2)}{(1-a)^2 \ln a}$ | Not specified | Not specified | All |

Dirker and Meyer [4] investigated several existing correlations published in the literature and found differences of up to 20% in the correlations available. Their data ranged over a Reynolds number (defined as $Re = \rho V D_h/\mu$ ) range of between 4 000 and 30 000. They also showed that the annular diameter ratio of the annulus affects the Nusselt number. They reported on the average Nusselt number for the whole length of the heat exchanger with all of their tested heat exchangers having lengths of between 6.1 m and 6.3 m. They presented a correlation from their own experimental data, based on the modified Wilson plot method (the correlation is shown above in Table 1). Dirker and Meyer stated that the correlations put forward by McAdams [5] and the Dittus-Boelter [6] correlation matched their own data the best.

Gnielinski [7] presented a correlation to fit the existing data available in the literature, taking into account the data from several different authors (ranging from the early 1900s to 2005) including that of Dirker and Meyer [4]. The correlation presented by Gnielinski took the geometry of the heat exchanger into account, including the annular diameter ratio as well as the total heat exchanger length. His correlation (shown in Table 1) also gives an average Nusselt number for the whole length of the heat exchanger. Gnielinski [7], as well

as Dittus and Boelter [6], showed that the direction of heat flux influences the Nusselt number value. What may be observed is that Gnielinski's equation has a term where the length of the heat exchanger is the denominator. This means that if the length of the heat exchanger becomes shorter, the resulting Nusselt number will become larger. This might be due to the entrance effect having a greater influence on the total heat transfer.

There is little or no literature available that directly discuss the entrance effects of tube-in-tube heat exchangers. Cengel [1] shows in his book that the heat transfer rate increases as one moves closer to the entrance port of a heat exchanger (where the flow is not yet fully developed). This is a known phenomenon. Maranzana *et al.* [8] investigated heat transfer coefficients in mini and micro channels and the influence of axial conduction in the walls. They implemented a two-dimensional heat conduction representation in the walls of the mini and micro channels. Their results show that the most of the heat is transferred at the entrance region of their heat exchanger element, especially at lower Re numbers. This shows that entrance regions might have a strong effect on total heat transfer.

Van Zyl *et al.* [9] investigated annular heat transfer coefficients in tube-in-tube heat exchangers. In addition to obtaining average heat transfer coefficients, they divided the length of the heat exchanger into smaller control volumes (CV) and calculated local convective heat transfer coefficients. They found that the annular convective heat transfer coefficients were larger by as much as 14% at regions closer to the annulus inlet. The average Nusselt number found by van Zyl *et al.* was comparable (within 3% for a cooled annulus and within 20% for a heated annulus) with that found by Dirker and Meyer [4], McAdams and Dittus-Boelter [4-6]. He also notes that the direction of the heat transfer influences the Nusselt number.

### 2.4.2. Entrance region heat transfer

The entrance region is defined as the length it takes for the flow to become fully developed. The flow is thermally fully developed when the profile of the bulk fluid temperature does not change its shape along the length in the direction of the flow (temperature values will, however, change as heat is transferred, but the relative temperature profile does stabilise). The growth of the thermal boundary layer affects the heat transfer capability. Where the thermal entrance length may be approximated for the laminar flow region and the turbulent flow region by [1]:

$$L_{thermal,laminar} = 0.05RePrD_h$$

$$L_{thermal,trubulent} = 10D_h$$

It has been noted that the heat transfer coefficient is greater at the entrance region for most heat exchanger geometries. This also holds true for tube-in-tube heat exchangers operating in the laminar flow regime as shown theoretically by Singh in 1957 [10]; and more recently by means of experimental data obtained by van Zyl *et al.* [9] in the turbulent flow regime; and Cengel [1] also describes this phenomenon as being true. This same

phenomenon was also shown to be present in mini and micro channels as presented by Marazana *et al.* and Sasmito *et al.* [8, 11]. The reason for this is the relatively small boundary layer at the entrance of the heat exchanger, allowing for more mixing of the fluid which leads to higher convective heat transfer than at locations where the boundary layer is thicker and heat transfer depends more on the thermal conductivity of the fluid. It is extremely difficult to measure the thickness of the boundary layer directly, but its effect is contained in the heat transfer coefficient.

Singh [10] used differential equations derived from the energy balance for a specific incremental area of the tube under investigation. The study considered a constant-property viscous, incompressible and heat-conducting fluid flowing inside a smooth tube with a constant surface temperature. The eigenvalues with their associated eigenfunctions of the differential equation were calculated in order to solve for the heat transfer capability along the length of his heat exchanger. It was found that with a constant wall temperature for laminar flow inside a smooth tube, the local Nusselt number at the inlet tends to infinity, but falls exponentially to 3.66 for regions where the flow is developed. Most of the literature on thermally developing flow is for the laminar flow regime and includes different heat exchanger types [12-16].

## 2.5. Thermochromic Liquid Crystals (TLCs)

Research employing thermochromic liquid crystals is continually growing. It is an invaluable tool used in flow visualisation, complex surface temperature measurements and also in heat transfer studies. TLCs may be suspended in the working fluid as tracer particles (which double as elements for fluid temperature measurement) or painted onto a surface of which the temperature is to be determined. Common examples of cases where TLCs are used in commercial products are in fish tank thermometers and colour-sensitive coffee cups.

Thermochromic liquid crystals are materials which change their reflected colour in the presence of white light as a function of their own temperature [3]. TLCs are organic compounds derived from cholesterol esters. They have two distinct melting points, the first of which turns the solid into a cloudy liquid and the second one turns the liquid clear.

The cloudy phase is called the liquid crystal phase (or the mesomorphic phase) and is a condition where the substance exists intermediately between a solid crystal and an isotropic liquid. This occurs because the molecules are movable but still organised in a helical pattern. When in this phase, the substance acts mechanically like a fluid but has crystalline optical properties [3].

The theory behind the optical properties of the substance lies in the behaviour of the molecular structure. The helical structures of the liquid crystals have a pitch length. These lengths are in the visible light wavelength spectrum. This pitch length may be altered by means of an external stimulus, either temperature or shear stress [17]. By changing the pitch lengths, the reflected wavelength is also changed, therefore presenting as a different

colour. The fundamental structure of the liquid crystal structure is not affected by the external stimulus (temperature or shear stress) with the result that the change is repeatable under the same circumstances.

There are three main classes of liquid crystals: chiral-nematic, cholesteric and smectic. Chiral-nematic and cholesteric liquid crystals are insensitive to normal as well as shear stresses [18]. The two distinct melting points are useful for temperature measurement. At a lower melting temperature or activation temperature, the crystals reflect red light. As the crystals are heated up from their lower melting point to their upper melting point, the colour of the reflected light changes and all the colours in the visible light spectrum are covered. The crystals become transparent at the upper melting temperature. This temperature range is called the event temperature range. This phenomenon is repeatable and can be calibrated so that a certain colour correlates to a specific temperature. Another appealing feature of the chiral-nematic and cholesteric liquid crystals is that the response time to temperature changes is only a few milliseconds [19], making it a useful tool for transient studies.

The properties of cholesteric and chiral-nematic liquid crystals make them a very attractive choice for surface temperature measurement in heat transfer studies.

### 2.5.1. TLC configurations

According to LCR Hallcrest's handbook on liquid crystal technology [18], there are three configurations in which TLCs are mainly used:

- Unsealed TLC mixtures
- Microencapsulated TLC slurries
- TLC-coated polyester sheets

Each of these configurations has its own unique properties, which make them better suited to their respective applications.

The unsealed TLC mixtures have the brightest colour response of all the configurations, but are highly susceptible to environmental factors – for example fats, organic solvents and oxygen, making this raw product unsuitable for a wide range of applications.

Microencapsulated TLC slurries have been proven to be the most versatile temperature-indicative liquid crystals. The crystals are encased in a small protective layer, shielding them from the environmental factors that affect the unsealed TLC mixtures.

Coated polyester sheets are a pre-manufactured product where the crystals are sandwiched between a black substrate (for contrast) and a clear coating. This protects the TLCs and is manufactured as a ready-to-use product.

Both the unsealed and the microencapsulated TLC mixtures are also manufactured as sprayable coatings. This allows the user to spray an adhesive compound containing TLCs

onto any geometry. This requires a layer of black paint as a base onto which the TLC coating is sprayed. The black paint absorbs the incident light, so that the resultant reflected light is only that which is reflected from the TLC mixture.

### 2.5.2. Liquid crystal thermography (LCT)

Thermography may be loosely translated to temperature imaging. Instead of creating a picture based on the visible light spectrum, visuals are constructed on the basis of their surface temperature. Another example of thermography is using infrared imaging equipment as thermographic cameras. Thermographic cameras read surface temperatures based on the amount of infrared radiation they emit, according to the black body radiation law, and estimates the surface temperature. These temperatures (either measured by infrared radiation or extracted from the TLC colour response) are then used to construct a temperature field. Each pixel of a photo then represents the temperature instead its visible colour. Liquid crystal thermography works on the same principle. One is able to visualise temperature maps physically as the crystals change colour according to their temperature [17-21].

Not all liquid crystals have the same temperature response. The crystals are manufactured according to their required application. The two quantities which have to be specified are the onset or activation temperature and the bandwidth. The onset temperature is the temperature at which the crystals will start showing a visible red colour. The bandwidth of the crystals is specified as the difference in temperature from the red onset temperature to when the blue is visible. The usable bandwidth of the crystals is usually slightly more than the specified bandwidth [18].

### 2.5.3. Use of LCT in water tunnels

An example of LCT used as tracer particles was presented by Li *et al.* [22]. They used the microencapsulated slurry as temperature indicators suspended in the water. Their application was a bottom-heated, top-cooled cubic cavity with a baffle at the median height. These results included a temperature field of the water contained in the test setup as well as the velocity flow field.

Ogden and Hendricks [23] used liquid crystal thermography successfully on water tunnel models measuring surface temperatures. They covered a heated ellipsoid shape in TLCs. They protected the temperature-sensitive paint from damaging compounds by means of a thin (and also sprayable) acrylic polymer. A final polyurethane layer was applied over the acrylic polymer, which gave a tough workable finish.

The images were recorded, containing the colour field on the surface of the model and interpreted in temperature values. The interpretation of these reflected colours is called thermography, the method for which is the next topic of discussion.

### 2.5.4. Heat transfer investigation using LCT

Thermochromic liquid crystals have been used in heat transfer research and widely in turbulent heat transfer research in gas turbine/jet engine hot components. Stasiek *et al.* [24] used LCT to obtain heat transfer coefficients in fin-tube heat exchanger geometries with vortex generators. They also conducted a numerical simulation of the same problem and geometry. They found that the two methods were in satisfactory agreement with each other.

Stasiek and Kowalewski [21] employed TLCs to measure temperatures in selected experiments in their laboratory in order to calculate heat transfer coefficients and Nusselt numbers. Their applications included steady-state, as well as transient-state analyses. They used LCT in a wind tunnel on a cooled plate with complex geometries being heated by hot air flowing through the wind tunnel. Natural convection was also investigated by using the TLCs as tracer particles, showing an instantaneous temperature point through the fluid.

Tam *et al.* [25] used LCT to measure heat transfer coefficients in the case of micro channels. Tam placed the test section inside a vacuum box in order to minimise heat loss to the environment while maintaining visual access to the liquid crystals for measurements. They could estimate the heat transfer coefficients in their experiments within a 22% accuracy.

Similar experiments have also been conducted by numerous other authors, some of which include the following:

- Estimation of temperature-dependant heat transfer coefficients for a vertical rectangular fin by Konda Reddy and Balaji [26].
- In a mini-channel array for simultaneously developing flow under conjugated conditions, comparing LCT data to computational simulations by Rao and Khandekar [27].
- For local heat transfer measurement and a comparison between steady-state and transient methods by Critoph *et al.* [28].
- In a transient study by Chyu *et al.* [29] of an air turbine blade cooling channel, featuring delta-wing shaped vortex generators.

There is no known literature available, in which tube-in-tube heat exchanger analysis was done with LCT.

## 2.6. Literature review summary

The literature survey lists examples of similar research to that of the current study. It discusses possible shortcomings of the correlations present in the literature in that it does not explicitly account for inlet geometry or underdeveloped flow regions. The use of TLC in the literature is also discussed and examples are given where it was utilised in water channels, with some limitations. TLCs have to be isolated from the flow medium by means

of a protective layer when taking surface measurements. Examples are also given where LCT was employed for heat transfer studies.

# Chapter 3: Experimental setup and methodology

This section contains details of the experimental setup used in this study. This covers the experimental facility available in the laboratory, the instrumentation that was used, the heat exchanger design as well as any additional hardware that was required to complete this study. The relevant test cases are also discussed with respect to inlet temperatures and flow rates. The first topic of discussion is the experimental facility.

## 3.1. Experimental facility

The experimental facility used for this study, consisted of two water loops: one for cold water and the other for hot water. Figure 4 shows a schematic layout of the experimental facility and Table 2 supplies more information about the components in each loop.

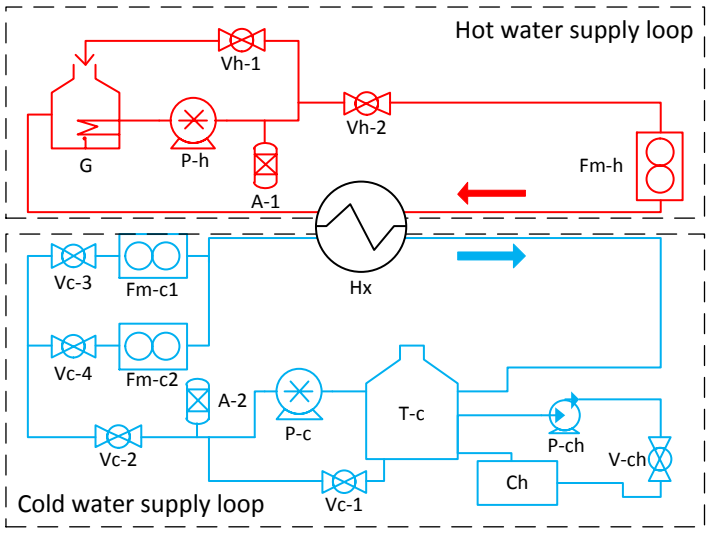


**Figure 4 – Experimental facility (nomenclature is defined in Table 2)**

**Table 2 – List of experimental equipment used (reference to Figure 4)**

| **Hot water supply loop** | | **Cold water supply loop** | |
|---|---|---|---|
| G | Hot water storage tank with 12-kW heating element (600 litres capacity) | T-c | Cold water storage tank 1 000 litres capacity |
| Vh | Ball valves | P-ch | Chiller pump |
| P-h | Positive displacement pump | V-ch | Chiller valve |
| A-1 | 4-litre accumulator | Ch | Chiller, 16 kW |
| Fm-h | Coriolis flow meter, 54.5 – 1 090 l/h | P-c | Positive displacement pump |
| | | A-2 | 4-litre accumulator |
| | | Vc | Ball valves |
| | | Fm-c1 | Coriolis flow meter, 54.5 – 1 090 l/h |
| | | Fm-c2 | Coriolis flow meter, 4.1 – 82 l/h |

The hot water loop featured a hot water storage tank with an electrical resistance heater, which heated the water to 45 °C. The water temperature was held constant by means of manually switching the thermostat. The hot water storage tank was followed by a positive displacement supply pump (P-H) and an accumulator (A-1) to limit flow oscillation. Valves (Vh-1 and Vh-2) were used to control the flow through the bypass line and the test line. The

mass flow rate in the test line was obtained via a Coriolis flow meter (Fm-h) placed before the heat exchanger test section (Hx).

The cold water loop was similar to that of the hot water loop. However, instead of having a heating element, it had a cold water reservoir (T-c), serviced by a chiller (Ct) (at 18 °C) equipped with a recirculation pump (P-ct) and a hand-operated valve (V-ct). The cold water temperature was maintained at around 20 °C by means of constant circulation to the chiller. Another difference between the two loops was that the cold water loop had two parallel-connected Coriolis mass flow meters (Fm-c1 and Fm-c2) before the test section heat exchanger (Hx). These two flow meters were of different capacity and a selection between the two was made by means of valves (Vc-3 and Vc-4), depending on the specific flow rate conditions.

The tube-in-tube counter-flow heat exchanger which was used as the test section had two inlet ports, one for the hot and another for the cold water, and two outlet ports. The corresponding inlet and outlet ports were connected to the relevant flow loops to facilitate heat transfer from the hot water to the cold water. The experimental facility also facilitated the investigation of a cooled as well as a heated annulus. This was done by switching the ports around so that either the hot or the cold water was fed through the annulus and vice-versa for the inner tube. More information about the test section heat exchanger is provided in section 3.2.

The inlet and outlet temperatures at all four inlet and outlet ports as well as the local inner tube fluid temperature needed to be measured (which will be elaborated on later in section 3.2). All these temperatures were measured by using T-type thermocouples with a bead diameter of 0.8 mm. All the thermocouple leads were connected to a National Instruments thermocouple amplifier board which was in turn connected to a personal computer. This gave the ability to accurately (with a measurement uncertainty of 0.11°C) log the temperatures which were measured by the thermocouples throughout the heat exchanger. The remaining surface temperature measurements were taken by imaging the surface of tube 2 which was covered in TLC.

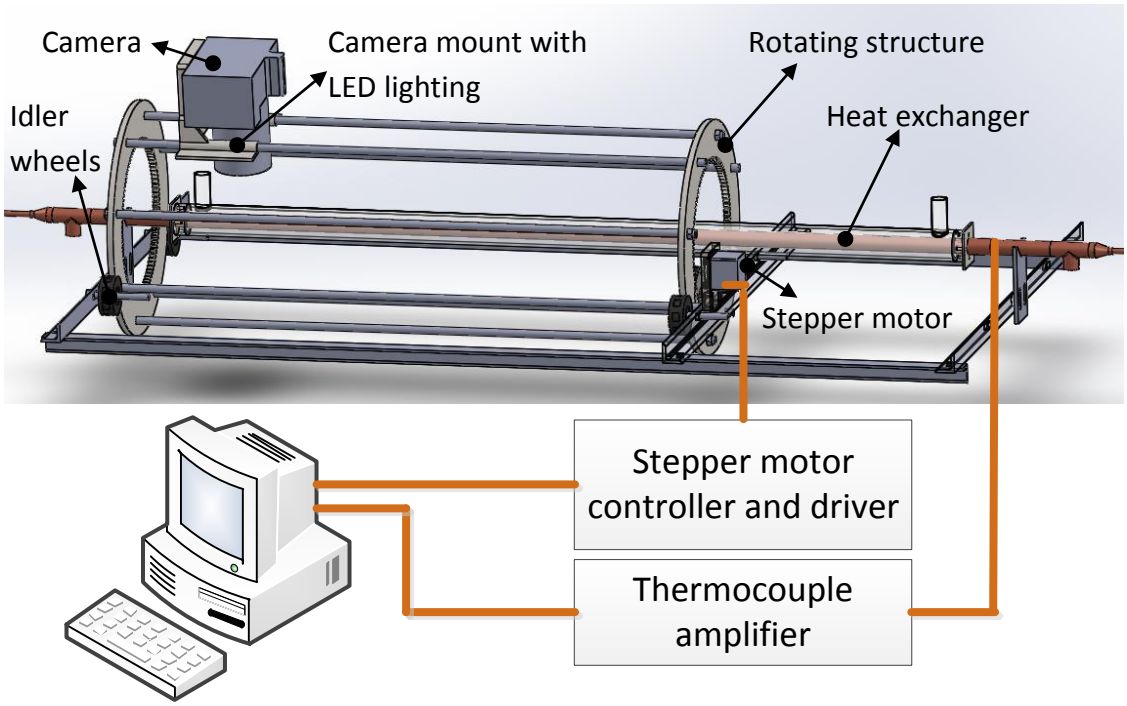


**Figure 5 – Electrical connection diagram of stepper motor control and thermocouples**

In order to accurately and reliably determine where a certain photo was taken of the surface of tube 2, a mechanism was built to position the camera around and along the heat exchanger (see Figure 5). This mechanism consisted of two large diameter wheels with internal gears. Threaded rods between the two wheels formed a round "squirrel" cage. This cage was placed on four rollers, two on each side, and was driven by a stepper motor. A camera mount was placed on two of the threaded rods and was allowed to slide along the length of the heat exchanger. It was possible to know how far the camera was tilted within an accuracy of 2° by controlling the stepper motor motion. The camera was moved along the length by hand and its position was pre-determined and measured by means of a measuring tape within 0.5 mm.

The camera mount in Figure 5 featured LED lighting. The LED lights used were manufactured by LUXEON (model ES – CW200) and were specified to emit light at a colour temperature of 5500K at a light intensity of 200 lumen each. There were 6 LED's, symmetrically positioned 3 on either side of the camera lens and were thus the same distance from the setup as the camera itself. The LED's were powered using a DC power supply ensuring that the proper 700mA forward current was applied and regulated at all times.

The LED lighting was powered through a cable with suitable slack for one full rotation. The lighting strip was fixed onto the bottom part of the camera mount, close to the camera. This setup facilitated the capturing of photographs with the digital camera. The procedure followed for capturing images of the surface of tube 2 involved moving the camera to a specific axial location and taking all the images around the circumference at that specific point, before moving to a new axial location. This resulted in taking the images in distinct rings at a time.

A 7-megapixel digital camera (Panasonic DMC Tz-3 which implements a 1/2.35 inch CCD) was mounted to the mechanism used to capture still photographs of the surface of tube 2, with its surface having been coated in TLCs. These images were later used to extract the wall temperatures. In order to achieve colour accuracy between all the photographs taken, all automatic features of the camera were switched off. Most aspects of the camera were manually controlled including the zoom, focal distance, film sensitivity (ISO), colour correction (set to none), shutter speed, aperture, white balance, image quality (set to fine) and image stabilization (switched off). This ensured that the camera itself would have little to no influence on the interpereted colour.

## 3.2. Heat exchanger overview

The tube-in-tube heat exchanger in this study featured three concentric tubes, two of which formed the heat exchanger and the third, the innermost one, used as a fluid temperature measurement rod. Figure 6 show the layout of the concentric tubes and the inner rod as well as their respective diameter designations and some temperature definitions that are used throughout this dissertation.

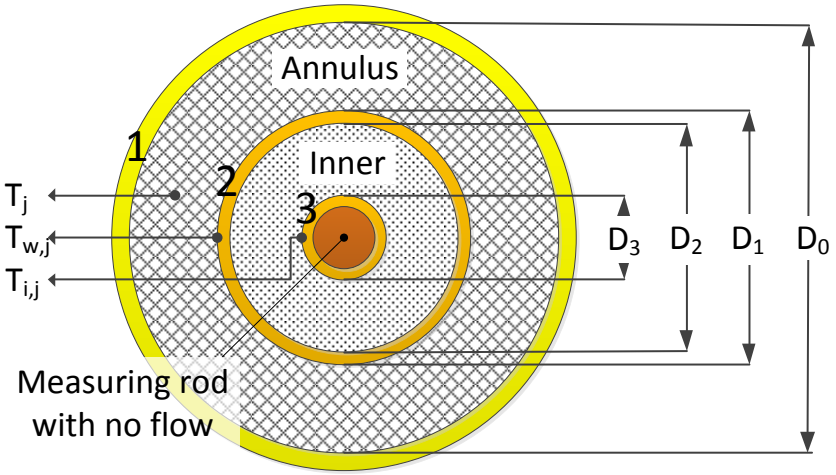


**Figure 6 – Concentric tube layout and designations**

Tube 1, constructed from Perspex, had an inner diameter of $D_0$ = 36.00 mm (± 0.1 mm) and acted as the outer wall of the annulus. The see-through Perspex facilitated capturing images of the inner tube's outer wall (Tube 2) which were treated with TLCs in the region close to the annular inlet port (stretching from the annular inlet port to 280 mm downstream) to obtain the profiles of the inner wall temperatures. Tube 2, constructed of copper, had an outer diameter of $D_1$ = 19.47 mm and a wall thickness of 0.8 mm which included all the LCT surface paint layers (these are discussed in section 3.3). This resulted in an annular diameter ratio of $a = D_1/D_0$ = 0.54. There were no physical obstructions present in the annular cavity (between tubes 1 and 2) of any kind.

Tube 2 was concentrically located inside Tube 1 by means of flanged connections on either side of the heat exchanger. These connections were machined from a solid 40 mm billet of Perspex and its inner diameter matched that of the outer diameter of tube 2. Tube 3, the

innermost tube and also called the measurement rod, had an outer diameter of $D_3$ = 6.5 mm and was used to measure the change in the bulk fluid temperature of the water passing through tube 2 (referred to in this dissertation as the inner fluid).

Measuring rod 3 was fully immersed in the centre of Tube 2 and was surrounded by the inner fluid. It was kept concentric inside tube 2 (the inner tube) by means of radial spacers with spokes no thicker than 1mm. The rod contained 11 measuring stations along its length with the thermocouple leads passing through inside it. Each measuring station was constructed from short (15 mm long) sections of copper tube onto which two T-type thermocouples were soldered internally. The measuring stations were separated from one another by 95-mm long acrylic tube sections with the same outer diameter as the copper sections. The acrylic sections minimised the axial thermal conduction along the length of the measuring rod, ensuring that the temperature measured at each measuring station was that of the fluid in the centre of tube 2, at that location.

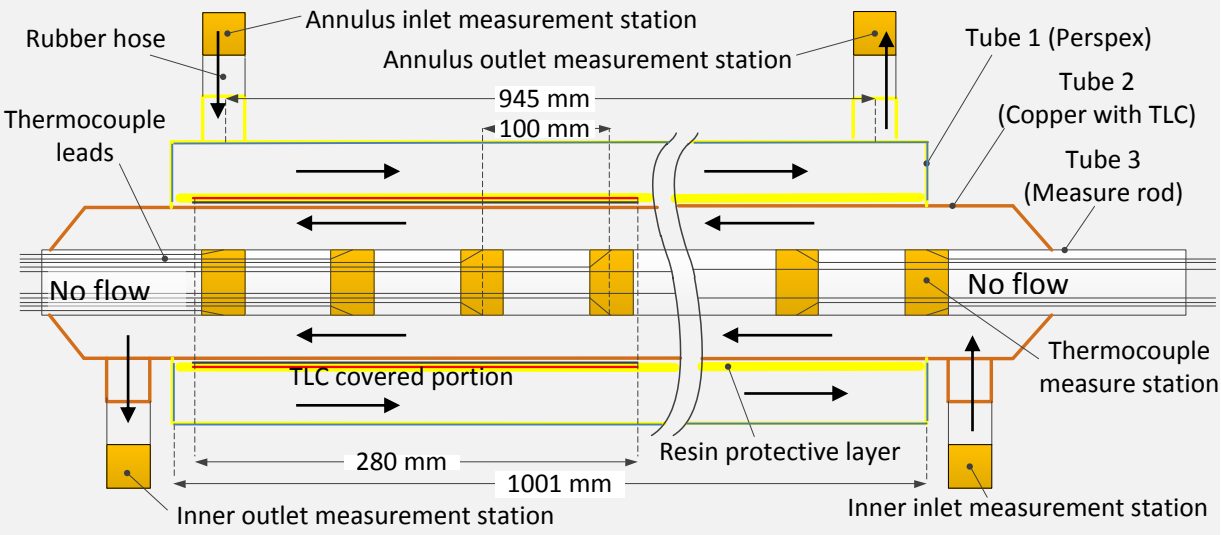


**Figure 7 - Schematic overview of test section**

Figure 7 shows the coupling layout of the heat exchanger. It shows the four measuring stations at the inlet and outlet ports. These stations were constructed from a short length of copper tubing with 4 thermocouples soldered to the outer surface. These measuring stations were isolated from the heat exchanger by means of a rubber hose, to restrict axial conduction from the heat exchanger to the measuring stations.

## 3.3. Heat exchanger construction

Tube 1 was constructed from Perspex which allowed the digital camera equipment to capture images of the surface of the TLC-coated tube (tube 2). Two 20 mm holes were machined into the Perspex tube in order to fix the inlet and outlet ports of the annular passage. The inner diameters of these ports were 16.00 mm (± 0.1 mm).

Tube 2 was constructed from three-quarter inch copper tubing. This tube was covered with a black base coat, TLCs and a resin layer. This was applied to the surface of tube 2, starting

at the inlet of the heat exchanger and continuing for 280 mm. The TLCs used in this study were manufactured by LCR Hallcrest and were of the cholesteric kind. The sprayable mixture of paint was water-based, making it soluble in water. For this reason, extra care had to be taken by adding the resin layer to prevent premature break-down of the paint layer. The resin layer was continued along the entire length of the heat exchanger in order to have a constant tube diameter. The thickness of all the paint layers and the resin layer was measured at 0.22 mm (with variances of ± 0.05 mm), which changed the outer diameter of the inner tube to 19.47 mm ($D_1$).

In order to maintain a constant paint thickness, a custom spray rig was constructed, based on a 3D printer (shown in Figure 8). This allowed for controlled motion during painting. The copper tube was rotated while an air brush was moved along its length at a constant axial speed, as the air brush followed a locus on the outer surface of the tube. This rig was used to paint the black back coat as well as the TLC coat. The resin coat was applied by spreading it over the outer surface of the tube by hand while the tube was rotating. Rotating the tube while the resin cured made for an even coat. The resin layer was sanded down using sanding paper on a wooden block while the tube was rotated in a lathe. After tube 2 had been constructed, the outer diameter was measured using a Vernier calliper at multiple locations to ensure that the coat had an even thickness and the outer surface was circular.

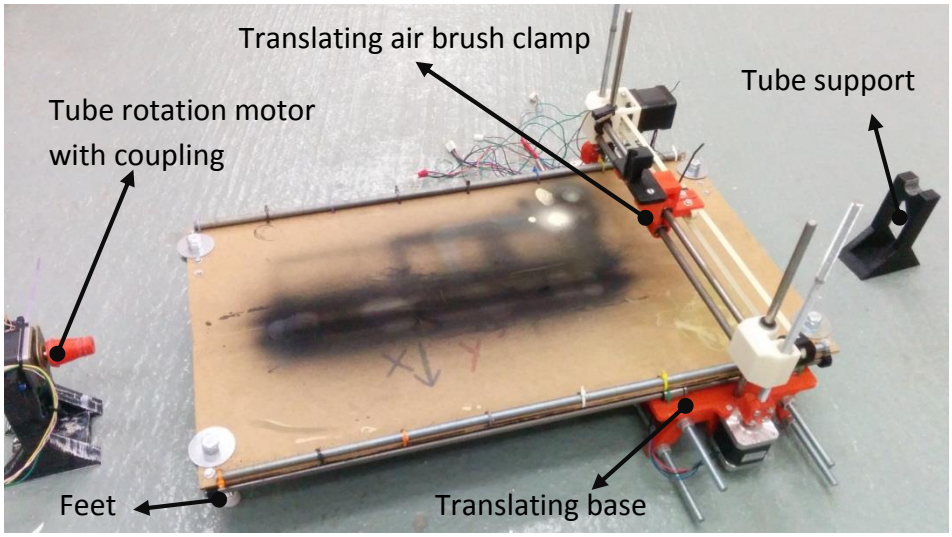


**Figure 8 – Customised painting mechanism used to apply TLCs**

This painting mechanism allows the air brush clamp to have three degrees of freedom. The motor with the tapered coupling, on the left in Figure 8, spun the copper tube while the air brush (mounted on the moving structure) was moved from right to left, effectively painting a spiral on the copper tube. This process was pre-programmed and the commands were sent to the stepper motors. An even coat was ensured by applying multiple coats, with subsequent coats shifting the pitch of the spiral by half a pitch and reversing the rotation direction.

As mentioned above, the inner most measuring rod was constructed from copper pieces and Perspex tube sections of the same diameter (using machining). Each copper section was 15 mm in length. The spacing was such that the measuring stations were positioned 100 mm apart. Each of the copper pieces contained two T-type thermocouples soldered to the inside of the copper piece. The basic construction of a thermocouple measuring station is shown in Figure 9 and the spacers are shown in Figure 10.

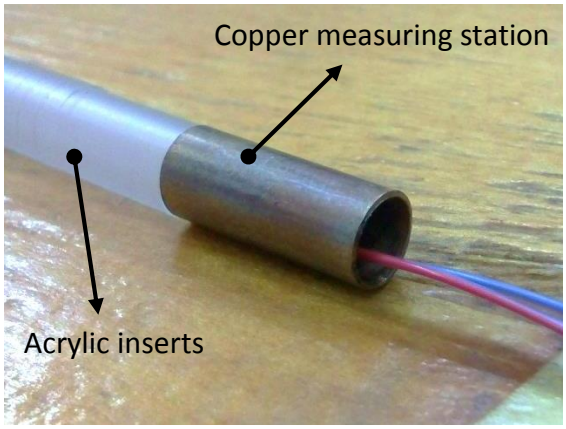


**Figure 9 – Photo of thermocouple measure station**

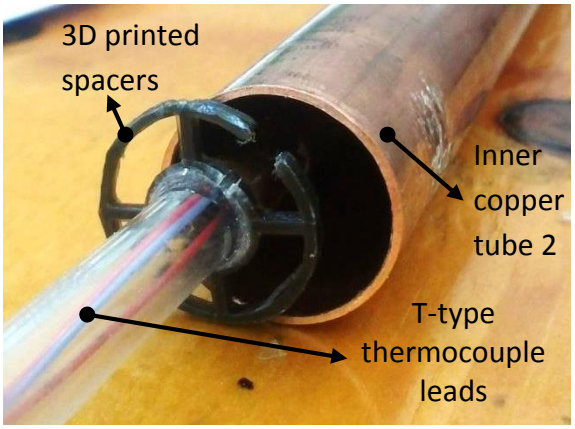


**Figure 10 – Photo of tube 3 spacers**

Another aspect to be considered was the entrance length for the inner tube of the heat exchanger. If the flow in a tube is fully developed (both hydrodynamically and thermodynamically), the heat transfer coefficient remains constant along its length. For this reason, the inner tube inlet was constructed so that it would have an adequate development length before entering the heat exchanger. The hydraulic diameter of the inner cavity is equal to $D_{h,ii} = D_2 - D_3 = 17.9 - 6.5 = 11.4$ mm. The distance from the inlet of the inner tube to the point where it enters the heat exchanger area was 280 mm. This gave the inner tube a length of 24.4 diameters (according to Cengel [1], turbulent flow will develop within 10 diameters) to develop fully. It is reasonable to assume that for turbulent flow, the flow would be hydrodynamically as well as thermodynamically developed by that point.

## 3.4. Thermal insulation

In order to minimise the amount of heat lost to the environment, the whole heat exchanger was covered with thermal insulation. The insulation used had a thermal conductivity of 0.036 W/mK as per the manufacturer's specification. The insulation was applied in such a manner that at no point was the insulation thinner than 25 mm, except for the part being imaged which was temporarily exposed. The exposed imaging portion was 6 cm long.

## 3.5. Test cases

Described here are all the different test cases that were run for this study, covering the flow rates and the inlet and outlet temperatures for both the cooled and heated annulus cases. There were five cooled annulus cases (CA 1 to CA 5), and four heated annulus cases (HA 1 to HA 4) as well as the different cases run for the calibration procedure. Table 3 contains the

test parameters for the separate testing conditions. They show the inlet temperatures, $T_{a,in}$, of the annulus and the inner tube, and the pre-decided Reynolds numbers.

**Table 3 – Summary of test cases for the cooled annulus configuration**

| | Cooled annular cases | | | | | Heated annular cases | | | |
|---|---|---|---|---|---|---|---|---|---|
| | CA 1 | CA 2 | CA 3 | CA 4 | CA 5 | HA 1 | HA 2 | HA 3 | HA 4 |
| $Re_a$ (-) | 1000 | 2500 | 5000 | 10 000 | 13 800 | 1000 | 2500 | 5000 | 8000 |
| $T_{a,in}$ (°C) | 41.8±0.1 | 42.9±0.3 | 43.5±0.1 | 42.7±0.3 | 43.4±0.7 | 20.8±0.1 | 20.5±0.1 | 20.5±0.2 | 20.2±0.2 |
| $Re_i$ (-) | 3600 | 3600 | 3600 | 3600 | 3600 | 3700 | 3700 | 3700 | 3700 |
| $T_{i,in}$ (°C) | 21.2±0.1 | 21±0.1 | 20.7±0.1 | 20.6±0.2 | 20.3±0.1 | 40.9±0.1 | 40.4±0.1 | 41.8±0.1 | 41.8±0.1 |

For the calibration, adiabatic tests cases were run to ensure the heat exchanger was at a known constant temperature throughout. The flow rate was kept constant at ± 900 litres per hour. This flow rate ensured turbulent flow in both the annular and inner flow passages. The inlet temperatures ranged between 14.4 °C ($Re_a = 5\,000$ & $Re_{ii} = 11\,000$) and 50.1 °C ($Re_a = 10\,400$ & $Re_{ii} = 23\,630$) with 50 temperature steps in between. The calibration tests were adiabatic tests during which the outlet of the annular flow passage was connected directly to the inlet of the inner passage.

## 3.6. Measurement procedure

All testing was conducted at night. This gave the most constant lighting conditions, as the sun shifts during the day and incidental light is also affected by weather conditions (such as clouds). The other advantage of testing at night was that the amount of ultraviolet (UV) light exposure to the TLC was minimised as they were never uncovered during the day. This ensured the longevity of the crystal surface, because UV breaks down TLCs [18]. When testing at night, the only light source present was that of the LED lighting used as the laboratory lights were also switched off during test.

All the measurements were taken at steady state. Steady state was deemed to have been reached for each ring if the temperature difference over the inlet and outlet ports (for both the annular and inner fluid passage) remained within a 0.2 °C range for two minutes. About 13 minutes were needed to capture all the needed images (about 140) of the inner wall of the annulus. Practically, it was difficult to maintain a constant inlet flow and thermal conditions for such a length of time, owing to the automated routine thermal adjustments in the chiller and in the geyser of the test facility. It was therefore decided that each “ring” would be treated separately when analysing the data, which eliminated the need for 13 minutes of steady operating conditions and reduced that time to about two minutes.

Even though there were systematic and routine adjustments in the test facility, approximately the same conditions were kept for the duration of the 13-minute tests in any case (within 0.4 °C for the inlet temperatures). This was strictly monitored; if it so happened that the temperature ranges varied by more than 0.4 °C over the 13-minute period, that test was repeated. Small temperature variations were, however, still addressed during the data-analysis procedures for all test cases, as discussed below.

The thermocouple temperature data was logged at a rate of 10 Hz for the full duration of image capturing. This was to ensure that no unexpected spikes in inlet temperatures were present when recording a data point. It also aided in analysing each ring's data individually.

The procedure of testing involved taking thermocouple readings, flow meter readings, setting the pumps to the correct speed to achieve a certain mass flow rate and taking photographs using the mechanised imaging mount. The sequence of operations is given in Figure 11.

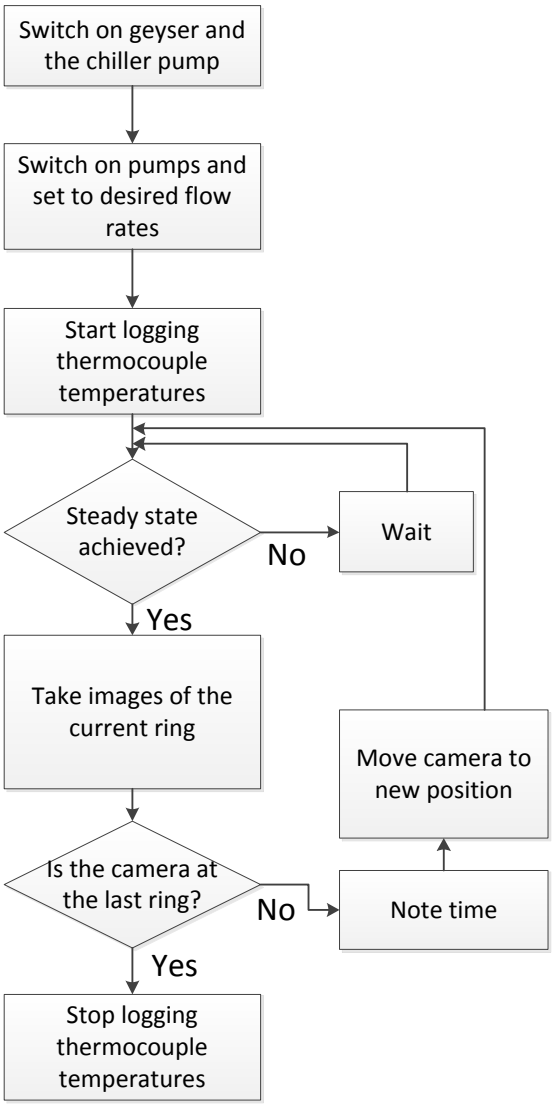


**Figure 11 – Data-capturing flow chart**

The test procedure involved switching on the heating element and the pump to the chiller unit. This ensured that the desired inlet temperatures were achieved. After the separate tanks had reached their respective temperatures, the pumps driving the hot and cold water loops were switched on and set to the desired speed. Directly after the pumps had been set, thermocouple data logging was initiated. It took about 10 minutes from the time the pumps were switched on for a steady state to be reached, after which the image of a ring was taken. When the current ring's imaging was finished, the camera mount was moved to the

next position and the next ring's images were taken until all the subsequent rings had been imaged. The time was noted after each of the separate rings had been imaged to distinguish what thermocouple data should be used in which ring. After all the images had been captured that were needed for a specific test case, the temperature logging was stopped.

The procedure set out in Figure 11 was repeated for each of the different test cases.

## 3.7. Summary of experimental setup and methodology

The current chapter described the experimental facility used in this study which featured two separate water loops, one hot water loop and another with colder water. The two water loops fed into two different ports of the counter-flow heat exchanger and reticulated back into their respective reservoirs. The experimental heat exchanger was housed inside a mechanical device which had a rotating cage on which the digital camera was mounted and positioned by the mechanical setup. The mechanical setup provided the needed placement accuracy in order to image tube 2 in a repeatable and reliable fashion.

Also discussed were the different test cases that were investigated with their associated flow rates and inlet temperature. The data capturing methodology was also discussed.

# Chapter 4: Data analysis

In order to obtain the heat transfer data, the data had to be reduced, most of which was done from the different temperature data obtained (thermocouple readings as well as wall temperature distributions). The first aspect discussed next is the total heat transfer rate.

## 4.1. Liquid crystal thermography

This subsection contains details of the implementation of LCT.

### 4.1.1. Interpretation of TLCs

A robust description of colour is needed so that the colour changes occurring can be interpreted accurately. Normal pictures (as digital photographs) are represented by pixels, each containing an intensity value of each of the primary colours: red, green and blue (referred to as RGB). This is, however, not an intuitive way to interpret colours as all the values are influenced by the brightness of the pixel with no change in the actual colour of the pixel. A more intuitive way of interpreting colour consists of the hue, the saturation and the brightness value (HSV). Hue is a pure representation of the colour, which is not influenced by the brightness of the object or pixel (see Figure 12 for a colour representation schematic under the HSV colour system). Saturation is a measure of the intensity of the colour and the 'value' represents the brightness of the pixel. This colour system separates the colour of the pixel from its saturation and brightness.

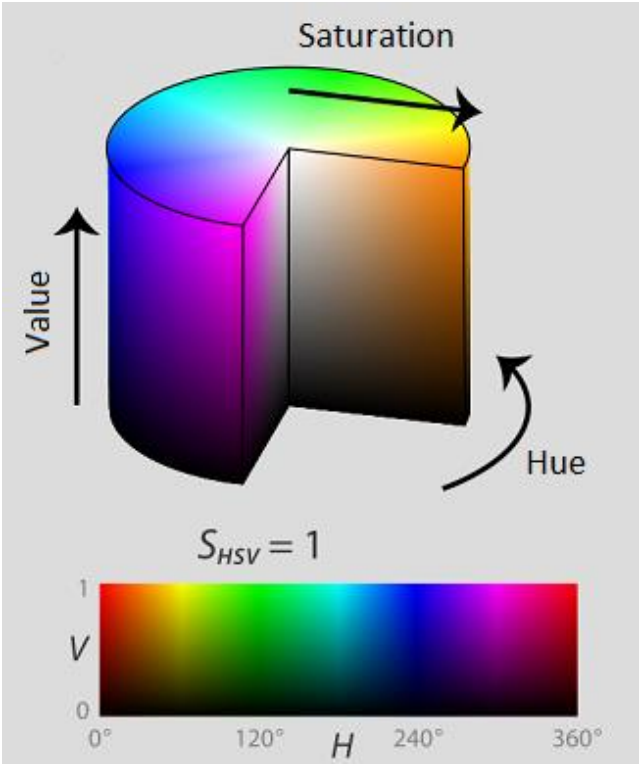


**Figure 12 – HSV colour representation (adapted from [30])**

Digital images may be converted from the RGB colour system to the HSV colour system. The method for doing this is described by Moeslund [31]. This may be done for each of the pixels

inside the data region, which needs temperature interpretation. The algorithm for switching from RGB to HSV is described below:

RGB images are usually represented in a 24-bit format, meaning that each of the colours, red, green and blue, has 8 bits per pixel to represent the intensity of its own colour. This means that each colour can have a numerical value between 0 and 255, which should be normalised to have a value between 0 and 1:

$$\begin{aligned} R' &= R/255 \\ G' &= G/255 \\ B' &= G/255 \end{aligned} \qquad \textbf{Eq. 2}$$

Next the most and least dominant of the three colours has to be determined:

$$C_{max} = \max(R', G', B') \qquad \textbf{Eq. 3}$$

$$C_{min} = \min(R', B', G') \qquad \textbf{Eq. 4}$$

$$\nabla = C_{max} - C_{min} \qquad \textbf{Eq. 5}$$

The hue angle is then calculated, based on which of the primary colours is dominant:

$$H = \begin{cases} 60° \times \left(\dfrac{G' - B'}{\nabla}\right) & if\ C_{max} = R' \\ 60° \times \left(\dfrac{B' - R'}{\nabla} + 2\right) & if\ C_{max} = G' \\ 60° \times \left(\dfrac{R' - G'}{\nabla} + 4\right) & if\ C_{max} = B' \end{cases} \qquad \textbf{Eq. 6}$$

The saturation value is then calculated based on whether the ∇ value is zero or positive:

$$S = \begin{cases} 0 & ,\nabla = 0 \\ \dfrac{\nabla}{C_{max}} & ,\nabla > 0 \end{cases} \qquad \textbf{Eq. 7}$$

The illumination value is defined to be:

$$Val = C_{max} \qquad \textbf{Eq. 8}$$

The resulting values are then:

- $Hue \in [0°, 360°]$
- $Saturation \in [0\%, 100\%]$
- $Value \in [0\%, 100\%]$

The hue angle was further normalised for use in this study. This made the hue value a factor between 0 and 1, instead of the arbitrary 0° to 360°.

$$H = \frac{Hue}{360°} \qquad \text{Eq. 9}$$

By using the converted hue angle value instead of trying to interpret the RGB values, the colour observed is no longer a function of the brightness of the lighting and also depends less on the equipment's interpretation (saturation) of the colour. This ensures that the colour being observed changes as little as possible owing to environmental factors. It is, however, still recommended that the exact same setup and equipment should be used to calibrate the crystals and to interpret them. There are physical factors which may influence the observed colour. This is discussed next.

### 4.1.2. Viewing and lighting angles

The viewing angle and lighting angle for observing the reflected colour of a liquid crystal is important since these may affect the observed hue value. This is especially so when the liquid crystals do not have backlighting (as in the case of an LCD display). The influence of the viewing and lighting angle on the observed reflected colour is discussed by Kodzwa and Eaton [32].

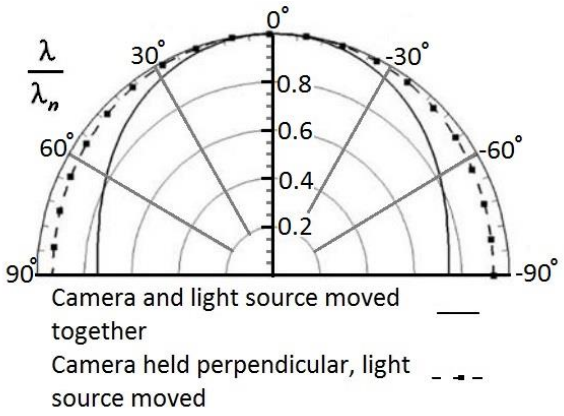


**Figure 13 – Influence of light source and viewing angles (adapted from [32])**

Figure 13 shows the influence of the incidence lighting angle as well as the angle at which the crystals are viewed from on the observed hue angle. Figure 13 indicates the wavelength ($\lambda$) observed at an angle relative to the wavelength when viewed perpendicular to the surface. If the hue angle is changed by any factor other than temperature (for example the viewing angle), that change will be interpreted as a change in temperature. It is therefore advisable to put the light source as well as the imaging equipment at the same point, perpendicular to the imaged surface.

The positioning of the light source and the imaging equipment is, however, not the only factors that may induce acute viewing angles. Refraction angles due to air-solid or air-liquid interfaces may also introduce acute viewing angles. Li *et al.* [22] had to make a correction to fix the perspective of their perceived images because of the light refraction through their water channel. A graphical investigation was also conducted to determine the viewing angle the camera "sees" due to the position of the camera taking into account the refraction

angles of the different materials the light would pass through and was found to be within 2° of perpendicular to the TLC surface.

All these factors could be taken into consideration when the setup of the experiment is designed as well as when careful calibration is applied. The best method to account for this is to keep the layout of the experimental measurement setup constant for calibration and data collection. Also, the incident angles were kept as small as possible by placing the LED lighting close to the lens of the camera.

### 4.1.3. Calibration of TLC mixtures

Thermochromic liquid crystals are calibrated by means of correlating a specified hue angle value to a known temperature. By repeating this for several temperatures, a calibration curve may be constructed [19]. This process should, however, be done for each application since no two batches of liquid crystals behave exactly the same, no two different types of cameras will record exactly the same colour and no two light sources will result in exactly the same light conditions. Although all these factors were manageable, the best way to account for these varying conditions was to keep them constant in the specified calibration and experimental setup.

The calibration curve used in this study was achieved by circulating constant temperature water through the annulus. The outlet of the annulus was then connected to the inlet of the inner tube, so that the same water circulated through the whole heat exchanger. This was done to ensure that the whole heat exchanger was isothermal. The inlet and outlet temperatures were monitored by using PT100 temperature probes which have a manufacturer uncertainty of 0.01 °C, so that the annular inlet and the outlet of the inner tube temperature would remain within 0.05 °C of each other. Figure 14 shows the calibration curve obtained:

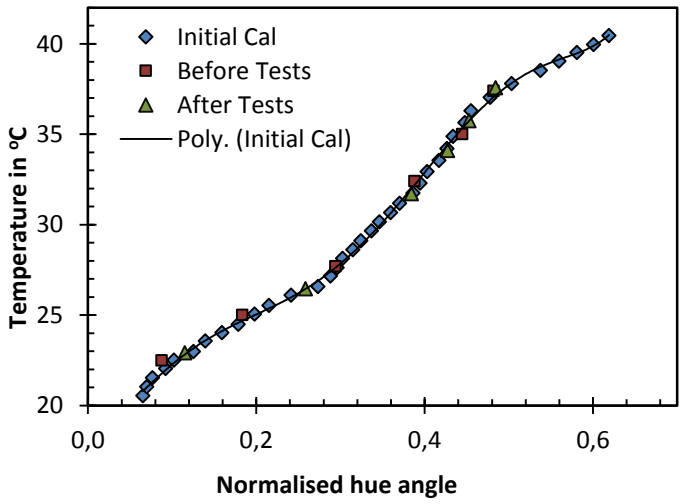


**Figure 14 – TLC calibration results**

The equation for the 6th order polynomial trend line shown in Figure 14 is represented below as Eq. 10:

$$T_{TLC} = 13781H^6 - 25198H^5 + 16594H^4 - 4676.1H^3 + 512.03H^2 + 21.936H + 18.215 \quad \textbf{Eq. 10}$$

Calibration may be done for all liquid crystal mixtures using the same technique, regardless of the bandwidth of the liquid crystals supplied.

Figure 14 shows the averaged hue of all the captured calibrations vs. the temperature values for the three calibration tests performed at different times during this study (an initial or TLC batch calibration, a calibration done before the test data was collected and a final calibration after all the data had been collected). The different calibration sets were required in order to confirm that the crystals still performed as they should and had not started to degrade. For this study, normalised hue was used, which is displayed on the x-axis.

Isothermal conditions were repeated for an initial calibration of 52 different temperatures, to ensure that the start and end values were accurately obtained. From these 52 temperatures, 37 of these points fell in the bandwidth of the liquid crystals. For each of these temperatures, the hue angle was extracted from the still images at five random physical locations on the heat exchanger. These five different photographs at each of the different temperatures, but at different spots on the heat exchanger, were analysed to ensure that they did not vary from one another by more than the manufacturer-specified uncertainty of ± 1% of the bandwidth (this equates to ± 0.2 °C). As the average hue angle between the five separate images showed an adequately low scatter, it was assumed that five points were sufficient.

Eq. 10 shows the 6th order polynomial fit. The polynomial was obtained by using a numerical solver. This polynomial equation was used in this study as the calibration formula for converting the estimated hue angle value to temperature. The standard deviation between the calculated values from the polynomial fit and the calibration measured values was found to be 0.13 °C and the largest difference between the equation and a single temperature point was ± 0.53 °C. Based on this, a decision was made to use ± 0.53 °C (this is close to the recommended value of between ± 0.4 °C – ± 0.5 °C by Rao and Zang [33] and Rao and Xu [34]) as the uncertainty per extracted pixel from the TLCs. This could be lowered by introducing an interpolation scheme between each of the data points. This was not used, however, due to its complexity when the statistical accuracy of a pixel cluster (defined by $0.53/\sqrt{16}$ for 16 pixels in a cluster) is equal in value to that of the standard deviation.

### 4.1.4. Interpretation of extracted hue values

Temperatures were extracted from the still images by means of calculating the hue values of the relevant pixels. This process was repeated for all the pixels contained in the desired sampling area, effectively replacing the colour of the images with representative temperatures at the specific point where the colour was interpreted.

A very grainy temperature distribution (as is typical with photographs) was obtained by considering the hue value from one adjacent pixel to the next when observing a zoomed version of the image. Grainy photos may be caused by a high ISO film speed (the camera used in this study was set at an ISO speed of 100, which is considered rather slow, reducing grain), some impurities on the tube surface or even the quality of the imaging sensor in the camera. A completely grain-free photograph could only be closely achieved with very expensive imaging equipment.

Since it would not have been physically possible for a large temperature difference to exist over such a short distance, it was necessary to base the temperature conversion on the average of 16 pixels in a 4 by 4 pixel area. This effectively lowered the image resolution but it resulted in a more physically correct smoothed temperature distribution field. Alternative approaches could have been taken, such as a surrounding-temperature filter which would have made each pixel a function of its surrounding pixels by means of a weighting factor. This approach would have been far more computationally intense and, knowing that the resolution of the aforementioned technique still gave a spatial resolution of 0.5 mm by 0.5 mm, it was deemed sufficiently small. Neither one of the techniques would have had an effect on the average wall temperature per ring, as both techniques would have taken the average of all the pixels available, regardless of the filtering technique.

### 4.1.5. Sampling area of TLC photographs

Before extracting temperature values from the photographs, it was necessary to select the sampling area that should be interpreted. Initially an area of 40 mm long by 1.5 mm wide on the tube surface was extracted per image. This posed a problem, however, when it came to the viewing angle of the crystal-coated surface. Because the Perspex and water refracted the light incident on the wall of tube 2, a temperature gradient of about 1 °C was observed over the 40 mm extracted section, when running at isothermal conditions. A 1 °C uncertainty in temperature due to the interpretation of the TLC is too large an error when considering the theoretical error of 0.2 °C. To better illustrate this, Figure 15 shows the wall temperature field on tube 2 for an arbitrary flow scenario. The figure shows that there were discontinuous temperature fields on the tube exactly where the next ring of images began. These discontinuities could only be caused by the acute viewing angles obtained when viewing a wide image.

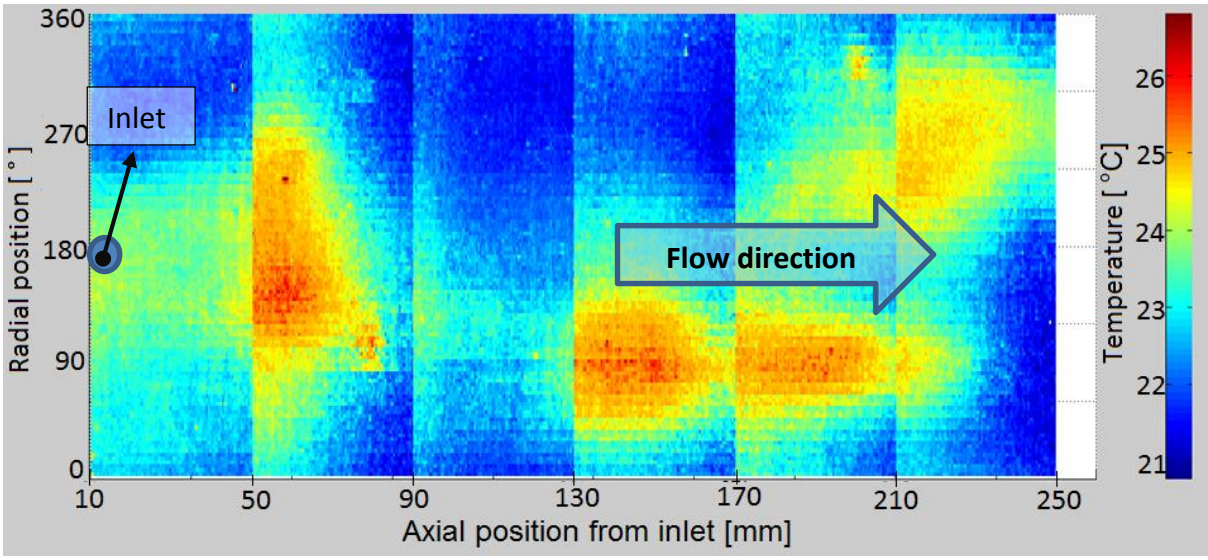


**Figure 15 – Composite temperature field showing discontinuous rings**

Due to the temperature gradient introduced by the large viewing area, the extracted area was limited to images of 10 mm in length. The possibility of reducing the number of images needed in order to obtain an accurate average wall temperature measurement per ring was also investigated. A sample case was investigated, where 40 images around the circumference were taken. The average wall temperature per ring calculated from 40 images was compared with only taking the averages from 20 and 10 photographs per ring respectively. This was done to minimise the time needed to measure the average wall temperature. Figure 16 shows that the change in the reading obtained for average surface temperature does not vary by more than 0.1 °C when reducing the sampling area.

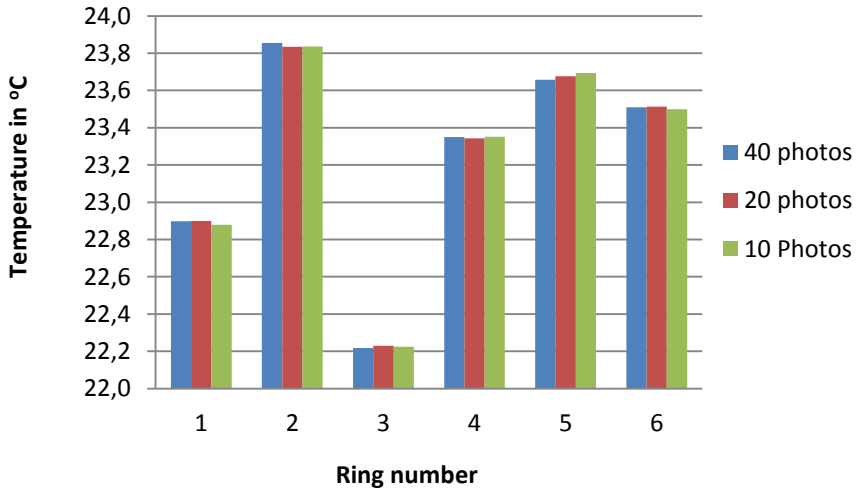


**Figure 16 – Study on average surface temperature vs. sampling area**

Figure 17 shows the total viewable area per ring achievable with 40 images captured around the circumference, each with a length of 40 mm. It also shows the extracted sampling area used in the calculations, consisting of 10 images with a length of 10 mm each.

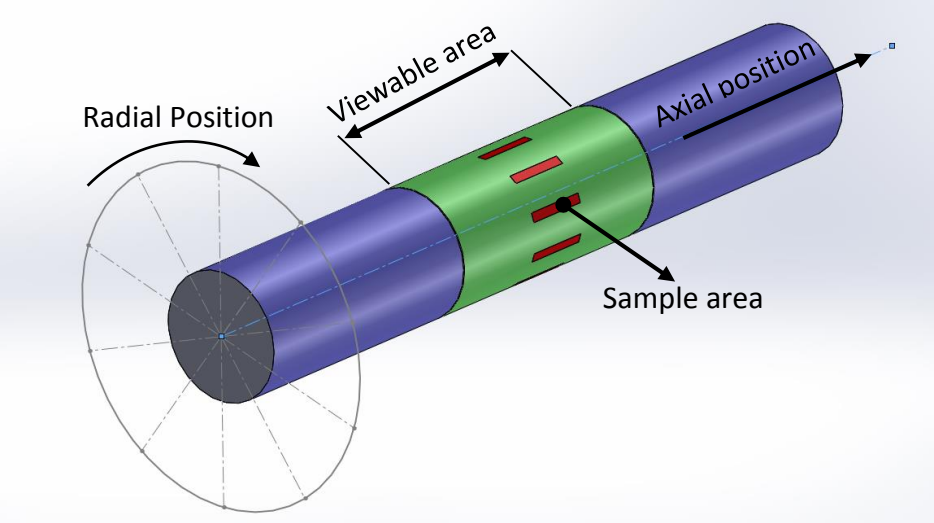


**Figure 17 – Viewing and sampling area**

It was therefore safe to assume that the smaller sample area did not affect the average surface area reading dramatically at any of the rings imaged. This reduction had two advantages. The first was that dramatically less time was needed to capture a full data point from about 35 minutes to 13 minutes. The second advantage was that less data reduction and therefore less computational time were required.

### 4.3.6. Temperature extraction from TLC photographs

Described below is the process followed to extract temperature data from the captured images, using a computerised script.

Before starting the data-processing, the images were grouped in a digital folder relating to the flow scenario considered and the axial position along the length of the heat exchanger. The script loaded one image at a time, performed all the computations on the selected image and then moved on to the next image contained in the folder. This process continued until all the images in the specified folder had been evaluated. Figure 18 shows an original image as taken by the digital camera. The 6 bright reflected spots visible in Figure 18 on the outer tube is due to the LED lighting fixed to the camera mounting. It should be noted that all external light sources were removed (testing was conducted during the evening and laboratory lights were switched off) during data capturing.

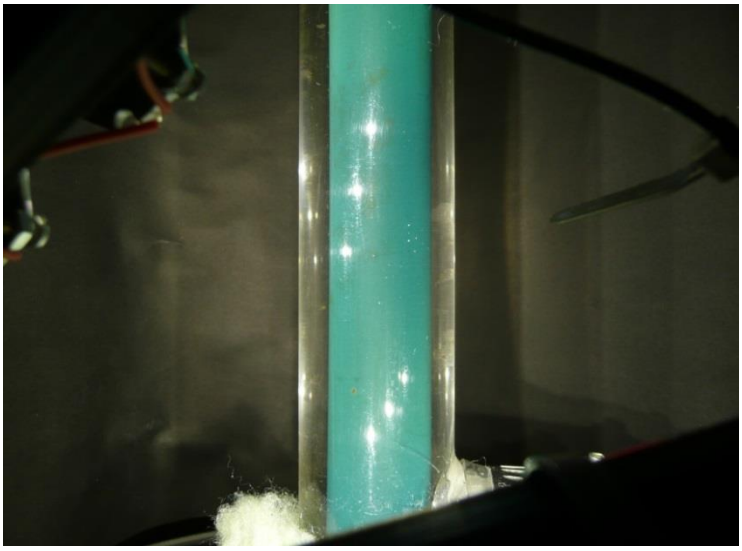

**Figure 18 – Photographs as taken by digital camera**

After the photo had been loaded, it was cropped and displayed as shown in Figure 19. The script automatically detected the outer edges of the Perspex tube (shown as the red squares in Figure 19). This distance was used as reference for a distance of 40 mm (outer diameter of the Perspex tube). Based on this, the size of the area in pixels extracted was calculated. The script automatically drew a 10 mm high box (white lines) where after the computer waited for the user to identify the four intersections between the white box and the TLC-coated tube (these four points are shown as yellow circles in Figure 19).

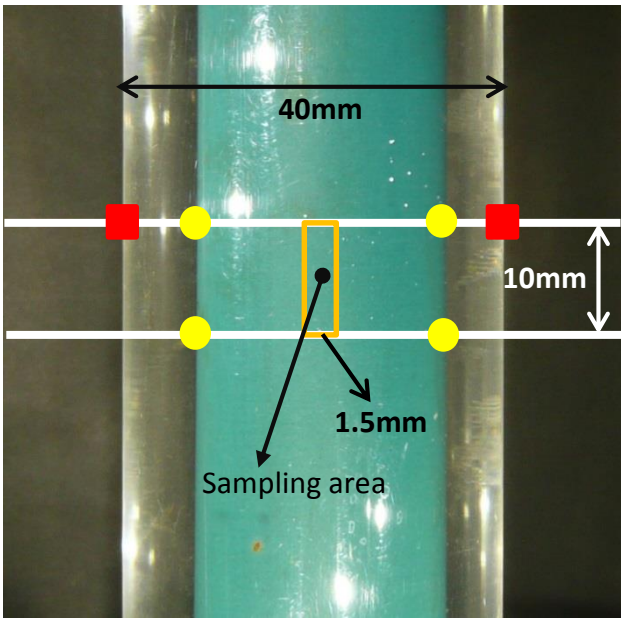


**Figure 19 – TLC image cropped**

The four points were used to centre the extraction area precisely in the middle of the copper tube. The box in the middle of the figure was the sample area. This was 1.5 mm wide and 10 mm high (note that Figure 20 is not drawn to scale). On average 250 pixels were contained in this area.

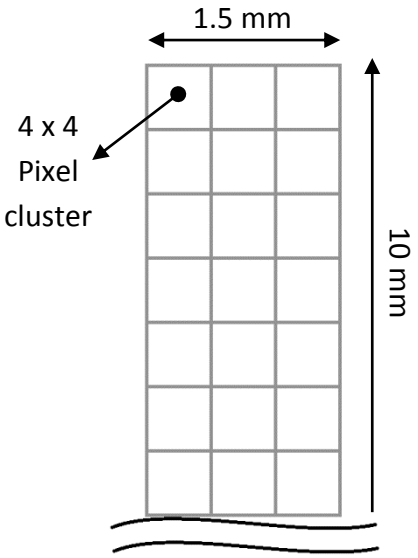


**Figure 20 – Schematic of propagation of pixel clusters**

Figure 20 shows how the pixel clusters were propagated after being extracted from the images. Each of the clusters was replaced in the same position on the new composite image as that from where it had been taken in the original image.

$$T_{TLC} = 13781H^6 - 25198H^5 + 16594H^4 - 4676.1H^3 + 512.03H^2 + 21.936H + 18.215 \quad \text{Eq. 10}$$

Each cluster now had an average hue angle value. This value was substituted into the 6$^{th}$ order polynomial fit (Eq. 10) created from the TLC calibration procedure. From this a temperature was obtained for each cluster. These cluster values were then arranged back in the way they were extracted to form a temperature map. The extracted temperatures of several images may be combined to form a composite image similar to the one shown in Figure 21.

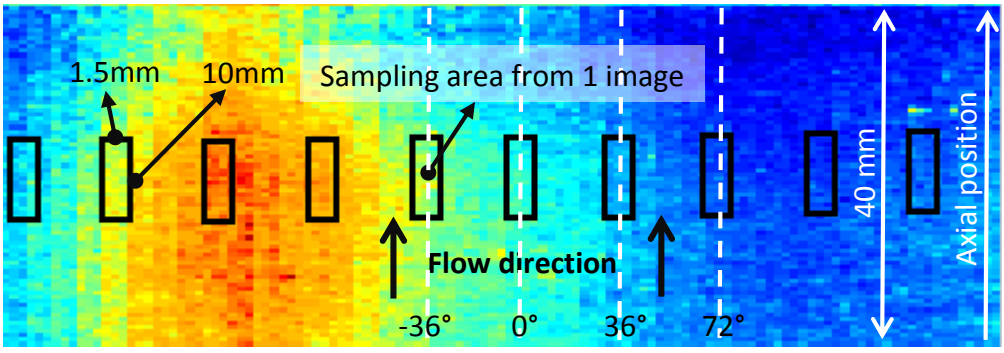


**Figure 21 – Composite temperature image of one ring, folded open**

Figure 21 shows the capabilities of liquid crystal thermography. This image was created by using a 40 mm long sample region where 40 images were captured around the circumference of tube 2. The whole image represents the previously mentioned “viewable area” whereas the area contained inside the black squares represents the sample area for

determining the average surface temperature. Therefore, each of the black squares represents one of the pixel cluster propagation images as shown in Figure 20.

The temperature distribution obtained from the LCT is shown in Figure 22 as was used later in the study for calculating the heat transfer. Each of the cells in Figure 22 represents the average temperature of a black square in Figure 21. Note that the first two rings were not complete because the inlet port obstructed the imaging of the entire ring. The image represents the temperature distribution if one were to fold the inner tube flat. The axial position shown is in the centre of the ring and was measured from the middle of the inlet. Ring 1 therefore represents the length of the tube from 0 mm up to 40 mm.

| | Axial position in mm | | | | | | |
|---|---|---|---|---|---|---|---|
| degrees | 20 | 60 | 100 | 140 | 180 | 220 | 260 |
| -144 | 27.6 | 28.0 | 26.5 | 31.8 | 30.2 | 31.1 | 32.2 |
| -108 | 27.7 | 26.1 | 24.9 | 31.3 | 27.8 | 27.9 | 27.8 |
| -72 | 27.7 | 26.0 | 25.9 | 30.8 | 29.8 | 28.9 | 28.2 |
| -36 | Blocked by inlet | | 27.3 | 32.7 | 30.5 | 31.7 | 28.9 |
| 0 | | | 25.6 | 34.1 | 32.2 | 32.6 | 31.3 |
| 36 | | | 26.0 | 32.1 | 30.4 | 30.9 | 29.5 |
| 72 | 27.7 | 25.2 | 26.1 | 29.6 | 27.5 | 27.7 | 27.2 |
| 108 | 27.8 | 25.8 | 25.6 | 27.6 | 26.7 | 26.2 | 25.9 |
| 144 | 28.1 | 27.8 | 25.3 | 27.5 | 26.3 | 25.6 | 25.8 |
| 180 | 28.2 | 26.1 | 25.2 | 27.5 | 26.3 | 25.3 | 25.8 |
| Ring | 1 | 2 | 3 | 4 | 5 | 6 | 7 |

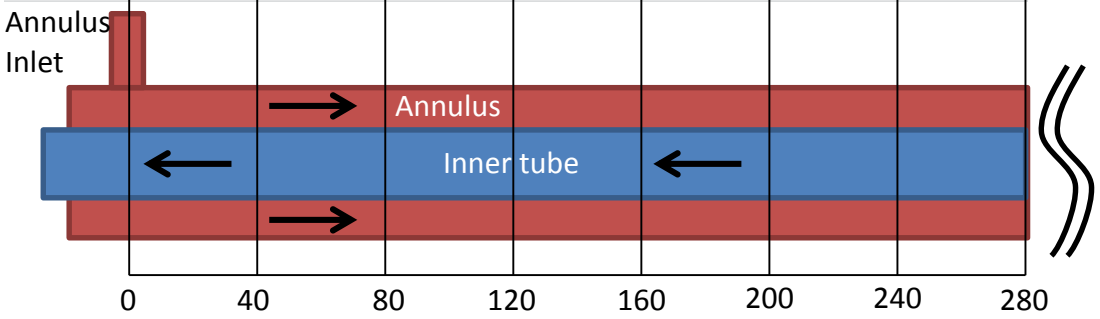


**Figure 22 – Temperature distribution at inlet for cooled annulus (Re ≈ 13 800)**

Note that the orientation in Figure 22 has changed from the previous images. The heat exchanger is now horizontal, not vertical as in Figure 18 - Figure 21. Figure 22 also shows a projected view of a schematic heat exchanger, indicating the points to which the separate rings are related.

The average wall temperature per ring is then taken as the mean of each of the columns and this value is used as $T_{w,j}$.

## 4.2. Thermocouple calibration

The thermocouples used (T-type) were calibrated in a similar fashion to that of the calibration of the TLCs. The whole heat exchanger was also assembled and measurements

were taken while running water of a constant (and known) temperature through the setup. The methodology differed slightly from the TLC calibration. Raw temperature readings were taken at temperatures ranging between 17 °C and 55 °C. The water was first cooled to 17 °C and the first calibration data point was taken. The water was then heated to 55 °C in increments of 2.5 °C, taking measurements at each increment. When the water reached 55 °C, it was cooled down to 17 °C in 5 °C increments. This resulted in a total of 24 isothermal points. At each of the pre-set temperatures, 200 thermocouple readings were taken one after another over a period of 20 seconds for each of the thermocouples. The inlet and outlet temperatures of the heat exchangers were again monitored using PT100 temperature probes.

All these temperature measurements were fed into a Matlab script, averaging the 200 samples for each thermocouple channel and creating a 3$^{rd}$ order polynomial fit to all the data points. Most of the thermocouple channels displayed a good quality calibration curve with a standard deviation of less than 0.05 °C. This means that a thermocouple reading error of at most ± 0.1 °C may be expected from the thermocouple readings, as accepted in the literature [35].

Some of the channels did however display large standard deviations during calibration, namely the two thermocouples at measuring rod station 5 and one from station 6. It was decided that these channels would be removed from the data analysis.

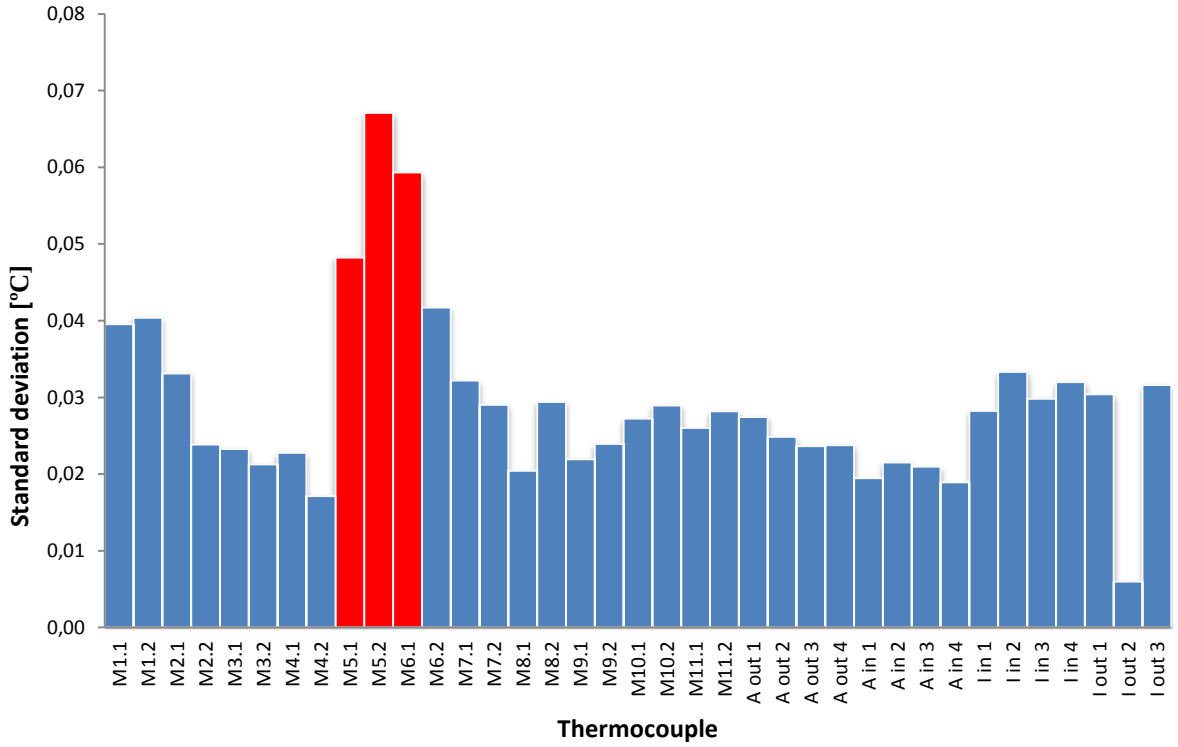


**Figure 23 – Standard deviations of thermocouple channels after calibration**

## 4.3. Heat transfer rate

The amount of heat transferred from the annular or the inner passage may be described as:

$$\dot{Q} = \dot{m} C_p \Delta T \qquad \text{Eq. 11}$$

This quantity may be calculated for both the annular fluid passage as well as the inner fluid passage. Both the inlet and outlet temperatures for both streams were directly measured and the flow rates were also known. The $C_p$ value was calculated by the equations put forward by Popiel and Wojtkowiak [36] and calculated at the mean temperature between the inlet and outlet.

## 4.4. Energy balance

By calculating the energy balance error, an idea can be obtained of how well the setup performed in terms of measurement accuracy and the effectiveness of the insulation. The energy balance error was obtained by comparing the heat transferred in the annular passage with that transferred in the inner tube. The energy balance error was calculated as follows:

$$eb = \left| \frac{\dot{Q}_{ii} - (\dot{Q}_a + \dot{Q}_{ii})/2}{(\dot{Q}_a + \dot{Q}_{ii})/2} \right| \times 100\% \qquad \text{Eq. 12}$$

Theoretically, the annular fluid should gain or lose exactly as much heat as the heat lost or received by the inner fluid. This would give an energy balance of 0%, indicating no heat was unexplained or lost to the surroundings.

Another quantity of interest is the amount of heat that was lost from the annular fluid to the surroundings. This was calculated theoretically by taking an approximation approach to a first-order steady-state heat transfer. There were four thermal resistances to account for:

- The convective thermal resistance to the surface of outer wall of the annulus, $R_{inner}$
- The conductive thermal resistance through the outer wall of the annulus, $R_{tube}$
- The conductive thermal resistance through the insulation, $R_{ins}$
- The convective and radiative thermal resistance to the surrounding, $R_{outer}$

These are shown schematically in Figure 24.

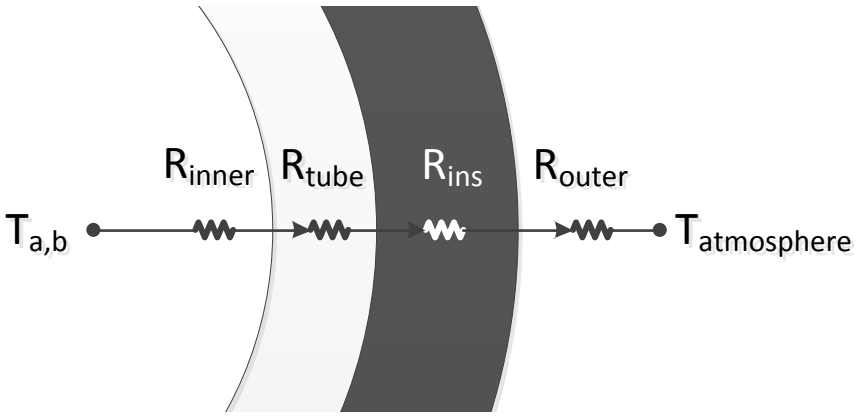


**Figure 24 – Heat loss to surroundings**

The thermal resistance between the bulk fluid temperature of the annulus and the acrylic tube ($R_{inner}$) was calculated as being negligible (smaller by a factor of a 100) relative to the resistance of the acrylic tube itself ($R_{tube}$) and the insulation ($R_{ins}$). The same held true for the resistance to the surroundings. It was therefore assumed that the temperature of the inner wall of the acrylic tube ($D_0$) was equal to the temperature of the bulk fluid and that the outer wall of the insulation was equal to the atmospheric temperature.

The thermal resistance for a generic cylinder (such as the acrylic tube and the insulation) may be calculated as:

$$R_{cylinder} = \frac{\ln(r_2/r_1)}{2\pi L k_{solid}} \qquad \textbf{Eq. 13}$$

The thermal conductivity of the acrylic tube and the insulation was 0.2 W/mK and 0.036 W/mK [37] respectively. The total resistance may then be determined by adding all the separate resistance entities to one another (units: K/W):

$$R_{total} = R_{tube} + R_{ins} \qquad \textbf{Eq. 14}$$

From this value the heat loss rate may be calculated using:

$$\dot{Q}_{loss} = \frac{\Delta T}{R_{total}} \qquad \textbf{Eq. 15}$$

For the worst case scenarios of the highest temperature for a cooled annulus and the lowest temperature for a heated annulus, the respective heat loss to the environment was calculated to be 4.6 W and -2.7 W (meaning gained from the surroundings). This equated to a heat loss or gain of 1.3% and 1% for a cooled annulus and a heated annulus respectively, relative to the total heat transfer between the fluids inside the heat exchanger.

## 4.5. Inner fluid bulk temperature and heat transfer rate

Contained inside the inner rod were 11 thermocouple measuring stations consisting of two T-type thermocouples each whose readings were averaged. Figure 25 shows how these thermocouple measuring stations were laid out inside the heat exchanger. The placement of these thermocouple stations also divided the heat exchanger into convenient CVs (CV) which were later used as calculation points. CV 1, 2 and 3 are further subdivided into seven smaller CVs (the size being dictated by the imaging rings) used for the inlet heat-transfer calculations.

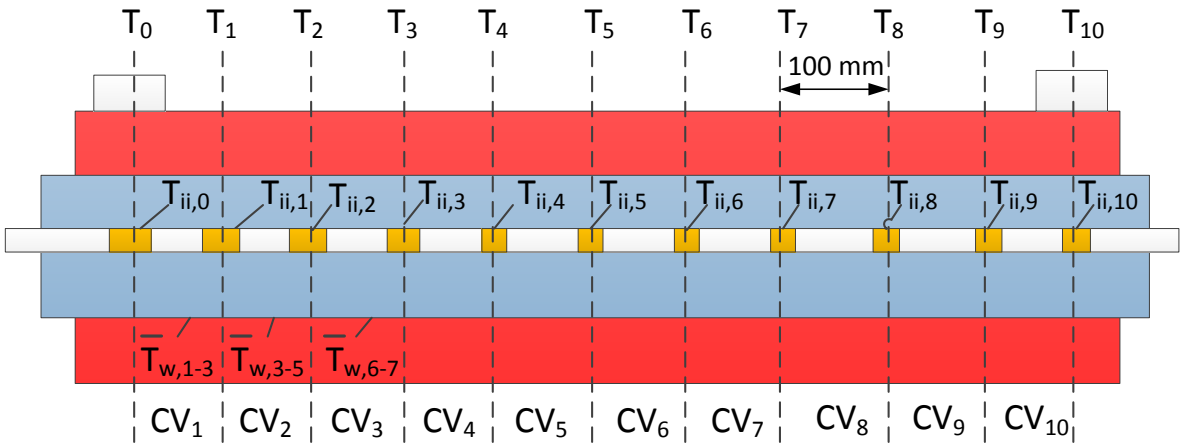


**Figure 25 – Schematic section view of experimental heat exchanger**

These stations were used to measure the temperature change along the inner fluid flow path. The inner fluid flow velocity chosen was sufficiently high for the adequate mixing of the inner fluid. This ensured that there were little or no temperature gradients locally over the measuring stations. As the mass flow rate of the inner fluid was known, the heat transferred between two subsequent measuring sections was calculated using:

$$\dot{Q} = \dot{m} C_p \Delta T \qquad \textbf{Eq. 16}$$

This expands to:

$$\dot{Q}_j = \dot{m} C_p (T_{i,j} - T_{i,j-1}) \qquad \textbf{Eq. 17}$$

The $C_p$ value was based on the average bulk fluid temperature between the two relevant measuring stations. This was facilitated by using the equations proposed by Popiel and Wojtkowiak [36] for determining the thermophysical properties of liquid water.

It was possible to obtain a temperature trend line for each test run by measuring at different points along the heat exchanger. Second-order polynomial fit trend lines were used to calculate the heat transfer in any given length of the heat exchanger. Second-order fits followed the profile of the temperature change along the heat exchanger the best. Figure 26 shows an example of such a temperature trend line for a cooled annulus with an annular Reynolds number of 13 800. Appendix C contains a complete list of these figures.

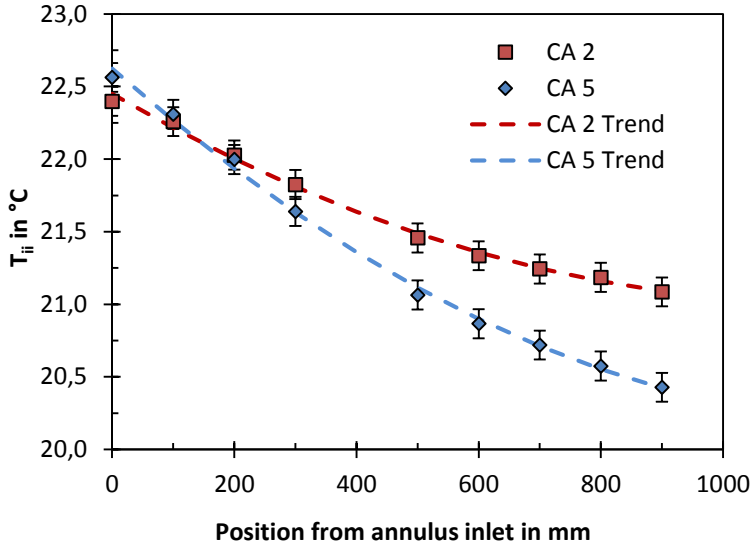


**Figure 26 – Measuring rod temperatures**

It was assumed that the amount of heat conduction along the length of tube 2 (inner wall of the annulus) was negligible in relation to the amount of heat transferred over the tube wall. To check if this assumption was valid, the surface temperatures were used to calculate the theoretical heat conduction rate:

$$\dot{Q}_{cond,tube2} = -kA_{tube2}\left(\frac{\Delta T_w}{\Delta x_w}\right) \qquad \text{Eq. 18}$$

These temperatures were analogous to those of the copper tube. The largest averaged temperature gradient was found to be 100 °C/m (for the case of a cooled annulus with an annular Reynolds number of 13 800). The thermal conductivity of copper was 398 W/mK [38], the cross-sectional area of tube was 33.37 mm$^2$. Therefore the calculated conduction is 1.3 watt.

Comparing this with the average over the first 300 mm of the heat exchanger (where this gradient was present) of 95 W, gives 1.4% for the worst case scenario. For most other cases, the heat conduction was about a quarter of this. In spite of the high thermal conductivity of the copper tube, the low relative level of conduction heat transfer was due to the small tube cross-sectional area. This low percentage of heat conducted is therefore negligible for the rest of the calculations.

## 4.6. Annular fluid heat transfer and bulk temperature

The bulk fluid temperature in the annulus, $T_a$, was not directly measured over the length of the heat exchanger as this would have interfered with the imaging. It was calculated by taking the energy balance for each of the CVs. It was therefore assumed that the amount of heat transferred inside the inner tube (as measured by the measuring rod) would be the same as that in the annular passage.

$$\dot{m}_{ii} C_{p,ii} \Delta T_{ii} = \dot{m}_a C_{p,a} \Delta T_a \qquad \text{Eq. 19}$$

It was possible by using the amount of heat transferred, to calculate the bulk temperature change of the annular fluid from the inlet of a CV to the outlet of that CV by using Eq. 20. Since the heat transferred to or from the inner tube must be equal to the amount of heat transferred to or from the annulus in each of the CVs:

$$T_{a,2} = T_{a,1} + \frac{\dot{m}_{ii} C_{p,ii} \Delta T_{ii}}{\dot{m}_a C_{p,a}} \qquad \text{Eq. 20}$$

In this way, the local bulk fluid temperature of the annular fluid could be obtained which was necessary, in conjunction with the local wall temperatures, to determine the local heat transfer coefficient.

## 4.7. Annular convective heat transfer coefficients

One of the aims of this study was to determine the heat transfer coefficients at the inlet region of the heat exchanger. This section contains the equations that were used to do this. Eq. 21 gives all of the quantities required to calculate the heat transfer coefficients.

$$h_{conv,j} = \frac{\dot{Q}_j}{A_{w,j}(T_{w,j} - T_{b,j})} \qquad \text{Eq. 21}$$

The heat transfer rate current, $\dot{Q}_j$, and the local annular bulk fluid temperature, $T_{a,j}$, were both obtained by using the thermocouple measuring stations contained in the measuring rod. The local inner wall temperature of the annulus, $T_{w,j}$, was obtained by using the measured hue values of the TLC coating. However, since a resin layer had been applied over the TLC layer and was situated between the TLC and the annular fluid, the temperature difference over the resin layer (which had a relatively low thermal conductivity), also had to be taken into consideration:

$$\Delta T_{resin} = \frac{\dot{Q} \tau_{resin}}{k_{resin} A_w} \qquad \text{Eq. 22}$$

where $\tau_{resin}$ is the thickness of the resin layer coating. The thermal conductivity of the resin ($k_{resin}$) used in this study was evaluated for its thermal conductivity and was found to be 0.219 W/mK (more details of how this value was obtained appear in Appendix A). The equation therefore becomes:

$$h_{a,conv,j} = \frac{\dot{Q}_j}{A_{a,w,j}\left(T_{w,j} + \frac{\dot{Q}_j \, \tau_{resin}}{k_{resin} A_{a,w,j}} - T_{a,b,j}\right)} \qquad \text{Eq. 23}$$

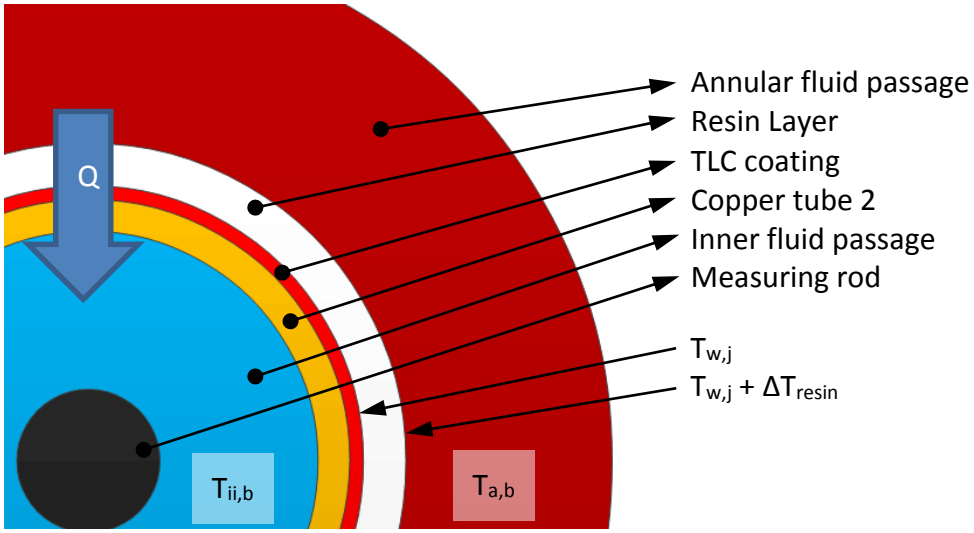


**Figure 27 – Schematic placement of temperatures**

This is to accommodate the temperature gradient present over the resin layer. From the methodology described above, it is possible to obtain localised heat transfer coefficients for each of the seven CVs designated close to the inlet of the heat exchanger.

## 4.8. Calculating the Nusselt number

The Nusselt number was calculated as:

$$Nu_{a,j} = \frac{h_{conv,j} D_{h,a,j}}{k_{a,j}} \qquad \textbf{Eq. 24}$$

The thermal conductivity used in this equation (Eq. 24) is based on the bulk fluid temperature of the water contained in the annulus for the current CV, as it is not constant over the temperature range considered. The evaluation of the thermal conductivity of the water for each CV is facilitated by the equations for physical water properties by Popiel and Wojtkowiak [36].

By calculating the heat transfer coefficient and the Nusselt number at the inlet of the heat exchanger, one is able to gauge the heat transfer capability at the inlet. In order to get a picture of what happens in the rest of the heat exchanger, the overall heat transfer coefficient is also calculated.

## 4.9. Calculating overall heat transfer coefficients

The CVs defined according to the positions of the measuring rod stations were used as calculation markers for the calculation of the local overall heat transfer coefficients. There are 10 of these CVs. The overall heat transfer coefficients were calculated by using the following formula:

$$\dot{Q} = U A_w \Delta T_{LMTD} \qquad \textbf{Eq. 25}$$

Rearranging and expanding this equation gives:

$$U = \frac{\dot{Q}}{A_w \left( \frac{\left(T_{a,j-1} - T_{ii,j-1}\right) - \left(T_{a,j} - T_{ii,j}\right)}{\ln\left(\frac{T_{a,j-1} - T_{ii,j-1}}{T_{a,j} - T_{ii,j}}\right)} \right)} \qquad \text{Eq. 26}$$

The inner fluid bulk temperature ($T_{ii}$) and the annulus bulk fluid temperature ($T_a$) were required for these coefficients. $T_{ii}$ was measured using the thermocouple stations in the measuring rod and $T_a$ was calculated by using Eq. 20. The above equation (Eq. 26) may be applied for separate CVs as well as for the whole heat exchanger by using the measured inlet and outlet temperatures. All these calculations utilised the trend lines fitted to the measuring rod temperatures.

## 4.10. Accounting for inlet temperature drift

As mentioned above, it took 13 minutes to capture all the data needed for one of the test cases. In this time, everything possible was done to ensure constant inlet temperatures. In spite of this, inlet temperatures did drift slightly (but not by more than 0.4 °C over the 13 minutes needed). Figure 28 shows the inlet temperature variations for test case HA 3 ($Re_a = 5\,000$).

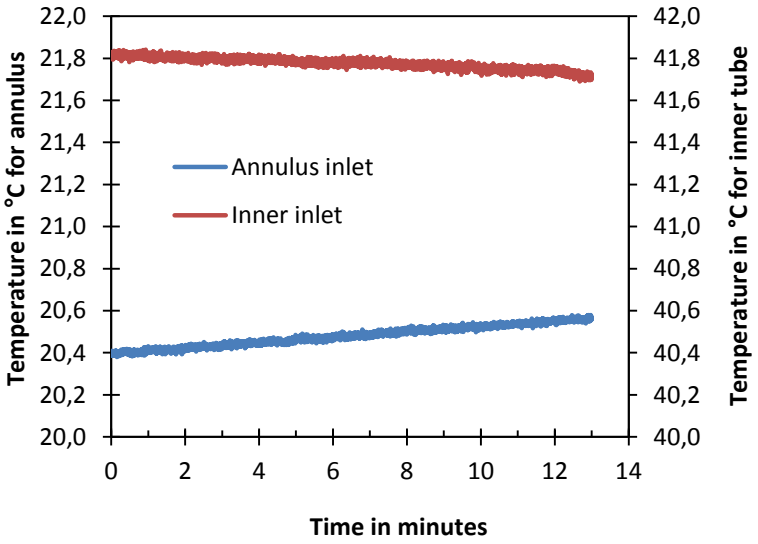


**Figure 28 – Inlet temperature vs. time**

To counteract the temperature drift, each of the different rings was treated as a separate mini test case. The inlet temperature for each of the separate rings was taken as the inlet temperature at the time when that ring was imaged. The first ring of images therefore used the average inlet temperature between minutes 0 and 2, the second ring between minutes 2 and 4, and so on.

## 4.11. Approximation of inner tube heat transfer coefficients

The inner tube heat transfer capability was estimated by using the modified second Petukov equation proposed by Gnielinski [39]:

$$Nu = \frac{(f/8)RePr}{1.07 + 12.7(f/8)^{0.5}(Pr^{2/3} - 1)} \quad \text{Eq. 27}$$

The friction factor was calculated by using the first Petukov equation for a circular tube:

$$f = (0.79 \times \log Re - 1.64)^{-2} \quad \text{Eq. 28}$$

The hydraulic diameter of the inner passage was used or all of the above equations, since the derivation was for a circular geometry without a measuring rod present. This is defined as $D_{h,ii} = D_3 - D_2 = 11.45$ mm. The heat transfer coefficient was then determined from the definition of the Nusselt number:

$$h = \frac{Nuk_{ii,b}}{D_h} \quad \text{Eq. 29}$$

## 4.12. Uncertainties

As is the case with any measurement equipment, some errors in measurement do occur. This has an effect on the calculated quantities and will therefore have an impact on the presented results. The type of errors which may be accounted for are fixed errors in which the actual value will lie within a given range from the actual value. These errors are typically given by the manufacturer of the equipment. This error type is also referred to as the accuracy of the measurement device.

There are, however, other sources of uncertainty which cannot be accounted for and these are introduced by uncontrollable factors. Some of these factors include electromagnetic interference, unknown faulty connections, system fluctuations or human error. One example of this is when a thermocouple wire acts as a heat sink from the junction of measurement.

This section gives only a brief overview of the method used to calculate the uncertainties. It also presents the results obtained from the uncertainty analysis. More information on how each of the uncertainties was calculated is given in Appendix B – Uncertainty analysis.

### 4.12.1 Uncertainty analysis method

The uncertainties ($\delta$) were calculated by using the method described by Kline and McClintock [40]. All uncertainties have the same units as the variable under investigation. These authors state that the calculated uncertainties predict a range within which the actual value will lie. The method further states that the combined uncertainty ($\delta R$) of two entities is the square root of the sum of the partial differential of each of the variables ($x_i$) squared:

$$\delta R = \left\{ \sum_{i=0}^{n} \left( \frac{\partial R}{\partial x_i} \delta x_i \right)^2 \right\}^{0.5} \quad \text{Eq. 30}$$

By using this method, it is possible to identify the weights that each of the variables' uncertainties have on the uncertainty of a particular calculated result. It is therefore possible to conduct a sensitivity analysis for a particular variable by superficially changing its accuracy and observing the resulting changes in accuracy. This was done to identify the largest source of the uncertainties in this study and is briefly discussed below.

### 4.12.2 Summary of uncertainties

Shown below are the tabulated uncertainty values for the entities of interest. First there are some common measurement and calculated quantities which show how accurately the physical entities could be determined with the setup. These are followed by the uncertainties for the calculated heat transfer values.

**Table 4 – List of uncertainties of common entities**

| Entity | Uncertainty |
|---|---|
| Polynomial approximation of TLC temperature ($T_{TLC}$) | ± 0.023 °C, depending on fit |
| Temperature difference in inner tube ($\Delta T_{ii,j}$) | ± 0.033 °C, depending on fit |
| Single LCT pixel | ± 0.53 °C |
| Average surface temperature from LCT | ± 0.03 °C |
| Single thermocouple | ± 0.1 °C |
| Inlet and outlet temperature (four thermocouples) | ± 0.05 °C |
| Annulus bulk temperature prediction | ± 0.18 °C |
| Resin thermal conductivity | ± 2% |

**Table 5 – Uncertainties of thermophysical properties of water approximations**

| Entity | Range | Uncertainty |
|---|---|---|
| $C_p$ equation | 0 °C – 150 °C | 0.06% |
| $k$ equation | 0 °C – 150 °C | 2.00% |
| $\rho$ equation | 0 °C – 150 °C | 0.04% |
| $\mu$ equation | 0 °C – 150 °C | 1.00% |

**Table 6 – Uncertainties in heat transfer**

| | CA 1 | CA 2 | CA 3 | CA 4 | CA 5 | HA 1 | HA 2 | HA 3 | HA 4 |
|---|---|---|---|---|---|---|---|---|---|
| $\delta \dot{Q}_{cv}$ [%] | 49 | 38 | 32 | 29 | 26 | 36 | 28 | 24 | 22 |
| $\delta \Delta T_{resin}$ [°C] | 3.1 | 3.1 | 3.1 | 3.1 | 3.2 | 2.2 | 2.2 | 2.2 | 2.2 |
| $\delta h_{local}$ [%] | 57 | 54 | 60 | 87 | 123 | 45 | 40 | 43 | 46 |
| $\delta Nu_{local}$ [%] | 57 | 54 | 60 | 87 | 123 | 45 | 40 | 43 | 46 |
| $\delta U$ (overall)[%] | 6 | 9 | 4 | 3 | 3 | 7 | 4 | 3 | 3 |

The uncertainty values contained in Table 6 and are based on the average uncertainty of all of the seven CVs at the inlet region. Each CV had a length of 40 mm. The uncertainty values obtained for each CV were added together and that total was divided by seven CVs to

obtain the averaged values shown above. It is therefore the average uncertainty for each of the CVs heat transfer coefficient values, and not the uncertainty for the average heat transfer coefficients over all the CVs (full length).

For example, in the case of a cooled annulus with a Reynolds number equal to 13 600, two of the seven CV uncertainties (CV 1 and 4) were comparably high (in the order of 180%) and this inflated the average uncertainty. This was due to the very small temperature difference between the bulk fluid and wall temperature at about 1 °C. The average uncertainty for the Nusselt number of the rest of the CVs (disregarding 1 and 4) is 86%.

Enlarging the CVs will greatly reduce the uncertainty percentages. To illustrate this, the average uncertainties for the heat transfer coefficient ($h_a$) over larger CVs were calculated and are shown in Table 7. The CVs were grouped together to form double and triple length CVs as well as the whole analysis region in one large CV (all seven together).

**Table 7 – Influence of control volume length on error percentages**

| | Cooled annulus | | | | |
|---|---|---|---|---|---|
| Length of CV | CA 1 | CA 2 | CA 3 | CA 4 | CA 5 |
| 40 mm | 57% | 54% | 60% | 87% | 123% |
| 80 mm | 18% | 21% | 25% | 32% | 50% |
| 120 mm | 12% | 12% | 15% | 23% | 18% |
| 280 mm | 6% | 8% | 11% | 16% | 18% |
| | Heated annulus | | | | |
| | HA 1 | HA 2 | HA 3 | HA 4 | |
| 40 mm | 45% | 40% | 43% | 46% | |
| 80 mm | 14% | 17% | 21% | 25% | |
| 120 mm | 11% | 11% | 14% | 16% | |
| 280 mm | 5% | 7% | 10% | 12% | |

Table 7 shows a considerable reduction in the uncertainty percentages when the CVs are enlarged. The reason for this is discussed below.

### 4.12.3 Explanation of large heat transfer coefficient uncertainties

The uncertainties for the heat transfer coefficients are quite large and fall beyond the generally acceptable uncertainty ranges for heat transfer investigations. The main source of error originates from the temperature measurements taken from the measurement rod.

Although the standard error from the polynomial fit was in the order of 0.023 °C, the temperature change between two arbitrary points along the heat exchanger could only be estimated within ± 0.033 °C. This was also quite low but considering that the temperature change over a CV was in the region of 0.15 °C (in the best case scenario with $Re_a$ = 13 800), this already introduced a measurement uncertainty of 22% in the temperature difference over a CV.

By further calculating the heat transfer per CV, based on this temperature measurement, it was possible to estimate only the heat transfer per CV within an uncertainty of about 26%. The annulus bulk fluid temperature, temperature gradient over the resin and the heat transfer coefficients were based on the amount of heat transferred in a CV. All of these entities were calculated with a value which had a 26% uncertainty. Therefore, each of these entities cannot be calculated within a better accuracy range. This is why the uncertainty of the calculated heat transfer coefficients was inflated to such a high level. Some recommendations on lowering the heat transfer uncertainties are made at the end of this dissertation.

## 4.13. Data analysis summary

This chapter gives the details of the equations and techniques used for converting the raw temperature and still image data into usable results. It describes how each element of the data analysis was done.

Each of the above elements played a role in gaining knowledge of how the test section performed. Firstly, the temperature measurement stations contained in the inner rod gave the amount of heat transferred per CV section of the heat exchanger. This data, in conjunction with the surface temperature measurements as performed by the TLCs, was used in order to calculate the heat transfer coefficients.

Overall heat transfer coefficients were also calculated by using either the inlet and outlet measuring stations built into the heat exchanger or the separate measuring stations contained in the inner measuring rod.

Some reliability aspects are presented at the beginning of the chapter, which were used to gather information about the accuracy of the heat exchanger and how well it was insulated from the environment. A criterion was used to validate the accuracy of the experimental heat exchanger setup in the form of the energy balance.

As with all experimental investigations, some inaccuracies will occur in measurements. These inaccuracies or uncertainties need special attention and were also discussed in short.

# Chapter 5: Experimental results

This section contains the experimental results obtained from this study. The results are presented in terms of the local position in the heat exchanger. Averaged heat transfer coefficients are also presented near the end of this section.

It should be noted that the way in which the results are analysed does affect the physical values presented. For example, the temperatures obtained from the measuring rod are utilised by means of fitting a trend line through the data points. Choosing a 2$^{nd}$ order polynomial to fit the data appears to have been the best fit to mimic relatively well the trend of the temperatures. However, higher-order polynomials were also plausible options. Also, as mentioned above, the first two rings were not completely imaged, which has an effect on the accuracy of the surface temperature measurements. This should be kept in mind when viewing the results shown below.

## 5.1. List of flow conditions

This section contains a list of all the different test configurations. It includes the physical properties of the different scenarios including the Reynolds numbers, inlet and outlet temperatures, volumetric and mass flow rates, some thermophysical water properties and the total amount of heat transferred per side for the entire length of the heat exchanger.

As shown in section 3.5, five different flow conditions were tested for a cooled annulus with different annular Reynolds numbers and also four different conditions for the case of a heated annulus. This list is divided into two groups, one for a cooled annulus (Table 8) and the other for a heated annulus (Table 9).

**Table 8 – Cooled annulus water properties and measurements summary**

| | Unit | CA 1 | CA 2 | CA 3 | CA 4 | CA 5 |
|---|---|---|---|---|---|---|
| | Annular fluid | | | | | |
| $Re_a$ | - | 970 | 2508 | 5102 | 10 024 | 13 819 |
| $T_{a,in}$ | °C | 41.84 | 42.88 | 43.52 | 42.74 | 43.42 |
| $T_{a,out}$ | °C | 38.74 | 41.27 | 42.49 | 42.15 | 42.93 |
| $\dot{V}_a$ | l/h | 100 | 250 | 500 | 990 | 1350 |
| $\rho_{a,in}$ | kg/m$^3$ | 991.56 | 991.15 | 990.90 | 991.21 | 990.94 |
| $\dot{m}_a$ | kg/s | 0.027543 | 0.06883 | 0.137624 | 0.272582 | 0.371601 |
| $\mu_a$ | kg/ms | 6.51E-04 | 6.30E-04 | 6.19E-04 | 6.25E-04 | 6.17E-04 |
| $\dot{Q}_a$ | W | 357.0 | 463.3 | 592.7 | 672.4 | 761.3 |
| | Inner fluid | | | | | |
| $Re_{ii}$ | - | 3 628 | 3 627 | 3 620 | 3 616 | 3 601 |
| $T_{ii,in}$ | °C | 21.18 | 20.98 | 20.70 | 20.55 | 20.32 |
| $T_{ii,out}$ | °C | 22.49 | 22.66 | 22.77 | 22.84 | 22.72 |
| $\dot{V}_{ii}$ | l/h | 240 | 240 | 240 | 240 | 240 |
| $\rho_{ii,in}$ | kg/m$^3$ | 998.05 | 998.10 | 998.16 | 998.19 | 998.24 |
| $\dot{m}_{ii}$ | kg/s | 0.06654 | 0.0665 | 0.0665 | 0.0665 | 0.0665 |
| $\mu_{ii}$ | kg/ms | 9.57E-04 | 9.57E-04 | 9.59E-04 | 9.60E-04 | 9.64E-04 |
| $\dot{Q}_{ii}$ | W | 364.4 | 467.4 | 575.9 | 637.1 | 667.8 |
| $eb$ | % | 1.0 | 0.4 | 1.4 | 2.7 | 6.5 |

**Table 9 – Heated annulus water properties and measurements summary**

| | Unit | HA 1 | HA 2 | HA 3 | HA 4 |
|---|---|---|---|---|---|
| | Annulus properties | | | | |
| $Re_a$ | - | 1 027 | 2 471 | 4 983 | 8 627 |
| $T_{a,in}$ | °C | 20.79 | 20.46 | 20.47 | 20.24 |
| $T_{a,out}$ | °C | 22.60 | 21.38 | 20.98 | 20.56 |
| $\dot{V}_a$ | l/h | 155 | 380 | 770 | 1250 |
| $\rho_{a,in}$ | kg/m$^3$ | 998.14 | 998.21 | 998.21 | 998.26 |
| $\dot{m}_a$ | kg/s | 0.042975 | 0.105367 | 0.213506 | 0.346619 |
| $\mu_a$ | kg/ms | 9.60E-04 | 9.78E-04 | 9.83E-04 | 9.91E-04 |
| $\dot{Q}_a$ | W | 325.2 | 405.3 | 455.3 | 463.7 |
| | Inner tube properties | | | | |
| $Re_{ii}$ | - | 3 736 | 3 758 | 3 767 | 3 761 |
| $T_{ii,in}$ | °C | 40.87 | 41.46 | 41.80 | 41.83 |
| $T_{ii,out}$ | °C | 39.20 | 39.27 | 39.20 | 39.00 |
| $\dot{V}_{ii}$ | l/h | 170 | 170 | 170 | 170 |
| $\rho_{ii,in}$ | kg/m$^3$ | 991.93 | 991.70 | 991.57 | 991.56 |
| $\dot{m}_{ii}$ | kg/s | 0.04684 | 0.0468 | 0.0468 | 0.0468 |
| $\mu_{ii}$ | kg/ms | 6.54E-04 | 6.50E-04 | 6.49E-04 | 6.50E-04 |
| $\dot{Q}_{ii}$ | W | 327.1 | 428.8 | 509.0 | 554.0 |
| $eb$ | % | 0.3 | 2.8 | 5.6 | 8.9 |

## 5.2. Inner tube heat transfer coefficients

The average temperature of the inner tube was 21.7 °C for a cooled annulus and 40.3 °C for a heated annulus. These temperatures were used to estimate the bulk inner fluid Prandtl number and were constant throughout the different test cases by ± 1 °C. The copper tube was estimated to be smooth. The Reynolds number in the inner tube was kept constant for all the tests at roughly 3 700. The friction factor equation (Eq. 28) was solved to obtain a friction value of 0.0408.

The Nusselt number for the inner wall may now be calculated using the Gnielinski equation (Eq. 27):

$$Nu_{ii,CA} = \frac{\left(\frac{0.0408}{8}\right)(3610)(7.01)}{1.07 + 12.7\left(\frac{0.0408}{8}\right)^{0.5}(7.01^{\frac{2}{3}} - 1)} = 106$$

$$Nu_{ii,HA} = \frac{\left(\frac{0.0408}{8}\right)(3750)(4.32)}{1.07 + 12.7\left(\frac{0.0408}{8}\right)^{0.5}(4.32^{\frac{2}{3}} - 1)} = 70$$

From this the heat transfer coefficients may be calculated by using $D_2 - D_3$ as the hydraulic diameter ($D_h$):

$$h_{ii,CA} = \frac{106(0.598)}{0.0114} = 5560\ W/mK$$

$$h_{ii,HA} = \frac{70(0.631)}{0.0114} = 3874\ W/mK$$

These heat transfer coefficients may be used to give an indication of which heat transfer side (the inner tube side or the annulus side) is more dominant in the total heat transfer over the inner tube wall. These values were not used to calculate any data.

## 5.3. Temperature measurements

This section contains a sample of the calculated bulk fluid temperatures in the annulus relative to the wall temperature of the inner tube. Also presented here are some of the measured temperatures from the measuring rod with their associated trend lines used for heat transfer calculations. These are shown first.

### 5.3.1. Inner tube fluid temperature measurements

Firstly, the measured temperatures inside the inner tube are presented with their associated trend lines. These are the temperatures that were measured by the thermocouple stations contained inside the measuring rod. Only two graphs are presented

in this section (both with an annular Reynolds number of 5000); the rest of these plots are given in Appendix C.

Take note that the heat exchanger is configured to be a counter-flow heat exchanger and all the horizontal axis markings are relative to the inlet of the annulus. Therefore the flow direction of the inner tube will be in the opposite direction, as indicated by the arrows in Figure 29 and Figure 31.

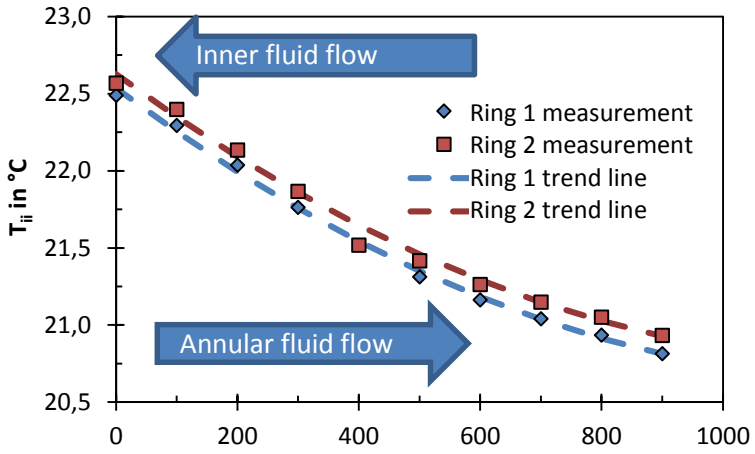


**Figure 29 – Trend line for measuring rod temperatures for a cooled annulus (Case CA 3, Re ≈ 5000)**

In the case of a cooled annulus, the fluid temperature increased as the inner tube fluid flowed through the heat exchanger, extracting heat from the annular passage. Figure 29 also shows how the curve (or trend line) fitted and how well it represented the measured temperatures. The measuring rod temperatures were taken in the time-frame in which the first ring as well as when the seventh ring was imaged. This indicates how the change over time in the inlet temperatures affected the measuring rod temperatures.

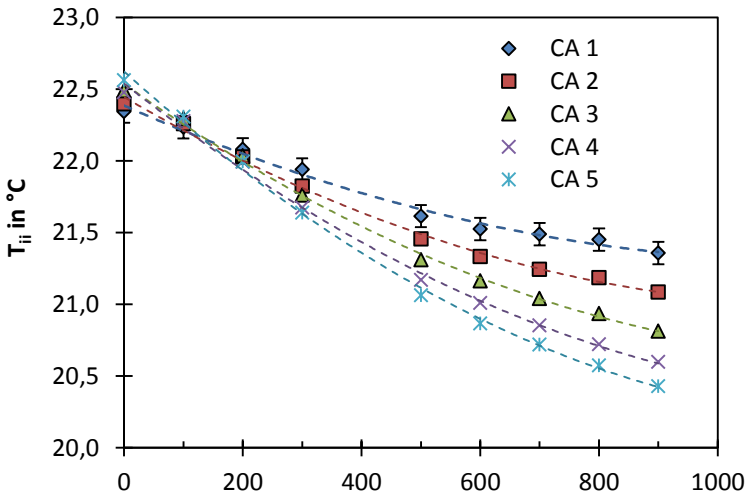


**Figure 30 – Measuring rod temperatures for all cooled annulus cases**

Figure 30 shows the measuring tube temperatures for all the cooled annulus cases. It is apparent that for higher flow rates in the annulus, the temperature change in the inner tube becomes larger.

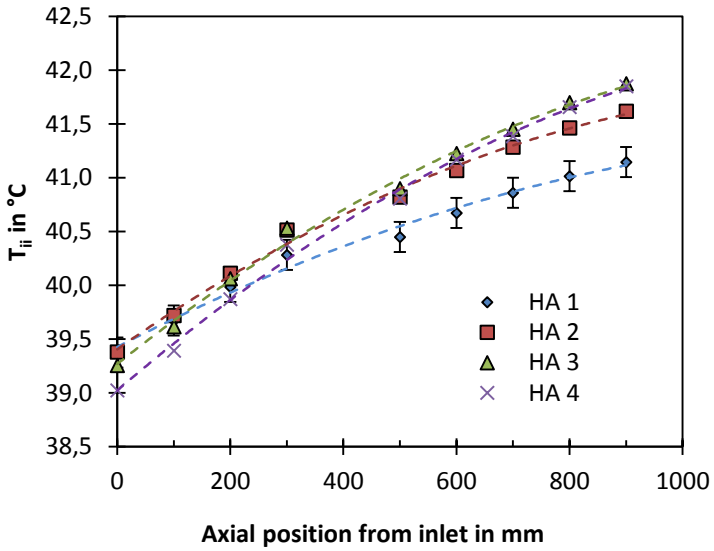


**Figure 31 – Measuring rod temperatures for the heated annulus cases**

Figure 31 shows the temperature distribution inside the inner tube for the case of a heated annulus. As expected, the temperature of the fluid decreases as it transfers heat from itself to the fluid in the annular passage. As mentioned above when discussing the calibration of the thermocouples, the thermocouples located at the fifth station did not produce reliable temperature readings, so they were excluded from any calculations.

Note in both cases that the temperature change does not follow a linear pattern. The rate of temperature change increases as the flow reaches the inlet port of the annulus. This is indicative that more heat is transferred per CV closer to the inlet port of the annular passage.

### 5.3.2. Wall temperature distributions

Presented in this subsection are some of the temperature distributions obtained while using the LCT technique. The temperatures presented here are based on the actual interpreted values obtained from the LCT and are not yet representative of the heat transfer wall temperature. For the heat transfer calculations, the temperature difference through the resin layer should also be taken into consideration. The rest of the wall temperature distributions are given in Appendix C.

The degrees column indicates the angular position at which a photo was taken relative to the inlet of the annular passage (which was situated at 0°). The numbers displayed directly under the heading are the distance from the annular passage inlet, where the inlet is at 0 mm. The blank cells indicate where the presence of the annular inlet port prevented the capturing of images.

**Table 10 – CA 3 ($Re_a \approx 5\,000$) wall temperature distribution in °C**

| deg\x | 20 mm | 60 mm | 100 mm | 140 mm | 180 mm | 220 mm | 260 mm |
|---|---|---|---|---|---|---|---|
| -144° | 27.5 | 25.1 | 25.2 | 29.4 | 28.3 | 27.7 | 27.0 |
| -108° | 27.4 | 25.0 | 24.7 | 28.7 | 27.3 | 27.5 | 27.1 |
| -72° | 27.5 | 25.1 | 24.7 | 28.1 | 26.2 | 26.3 | 25.9 |
| -36° | | | 25.2 | 27.2 | 25.8 | 25.1 | 25.4 |
| 0° | | | 25.1 | 27.2 | 25.8 | 25.3 | 25.3 |
| 36° | | | 24.6 | 27.2 | 26.0 | 25.9 | 25.4 |
| 72° | 27.3 | 25.3 | 24.3 | 28.0 | 27.0 | 27.1 | 26.3 |
| 108° | 27.3 | 24.9 | 24.8 | 30.4 | 28.5 | 29.3 | 27.9 |
| 144° | 27.5 | 25.3 | 24.9 | 32.4 | 30.9 | 30.9 | 29.7 |
| 180° | 27.5 | 27.1 | 25.8 | 30.3 | 29.1 | 29.5 | 27.7 |

**Table 11 – HA 3 ($Re_a \approx 5\,000$) wall temperature distribution in °C**

| deg\x | 20 mm | 60 mm | 100 mm | 140 mm | 180 mm | 220 mm | 260 mm |
|---|---|---|---|---|---|---|---|
| -144° | 35.8 | 35.5 | 36.0 | 34.2 | 35.5 | 33.2 | 33.2 |
| -108° | 35.9 | 35.7 | 36.1 | 35.7 | 36.3 | 35.0 | 35.2 |
| -72° | 36.2 | 35.9 | 36.5 | 36.0 | 36.6 | 35.8 | 35.7 |
| -36° | | | 36.6 | 36.3 | 36.7 | 36.1 | 36.0 |
| 0° | | | 36.7 | 36.4 | 36.7 | 36.1 | 36.2 |
| 36° | | | 36.5 | 36.4 | 36.7 | 36.1 | 36.2 |
| 72° | 36.1 | 35.9 | 36.3 | 36.3 | 36.7 | 35.9 | 35.1 |
| 108° | 35.8 | 34.8 | 36.0 | 36.3 | 36.4 | 35.9 | 35.7 |
| 144° | 35.6 | 35.7 | 35.4 | 35.9 | 36.2 | 35.6 | 35.7 |
| 180° | 35.6 | 35.7 | 35.9 | 35.4 | 35.8 | 35.0 | 35.2 |

Table 10 and Table 11 show the wall temperature distribution for two cases, one for a cooled and the other for a heated annulus, both at the same annular Reynolds number. It is clear that the wall temperature does not remain constant over the surface of the inner tube. In the case of CA 3 ($Re_a \approx 5\,000$), the temperature varied by as much 8 °C across the region that was considered, as shown in Table 10.

As the heat transfer coefficients are directly linked to the wall temperature, a change in the wall temperature affects the local heat transfer coefficients. The temperature gradients on the wall of tube 2 for a cooled annulus were observed as being much higher than for a heated annulus. This might be linked to the difference in Prandtl numbers between warmer and colder water.

### 5.3.3. Bulk fluid and wall temperatures

The driving force for heat transfer is a temperature gradient. Shown below are the measured and calculated temperatures pertaining to the bulk annular and inner fluids as well as the heat transfer wall temperatures (temperature measured by the TLCs, $T_{TLC}$, and the calculated wall temperature on the annular side, $T_{w,j}$) on tube 2. For a cooled annulus,

the bulk fluid temperature in the annulus should be higher than that of the wall in order for heat to be extracted through the tube wall. This is shown in Figure 32 and Figure 33 where the annular inlet is situated at 0 mm.

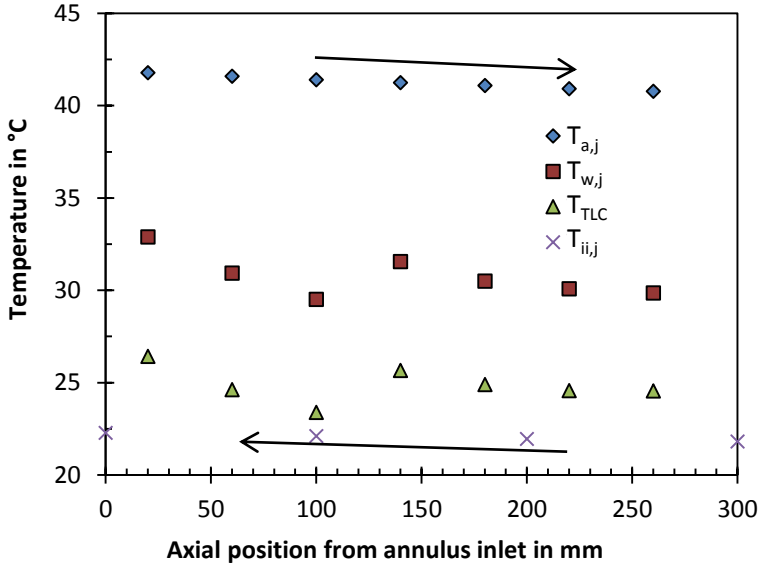


**Figure 32 – Bulk fluid and wall temperatures for CA 1 ($Re_a \approx 1000$) with flow directions indicated**

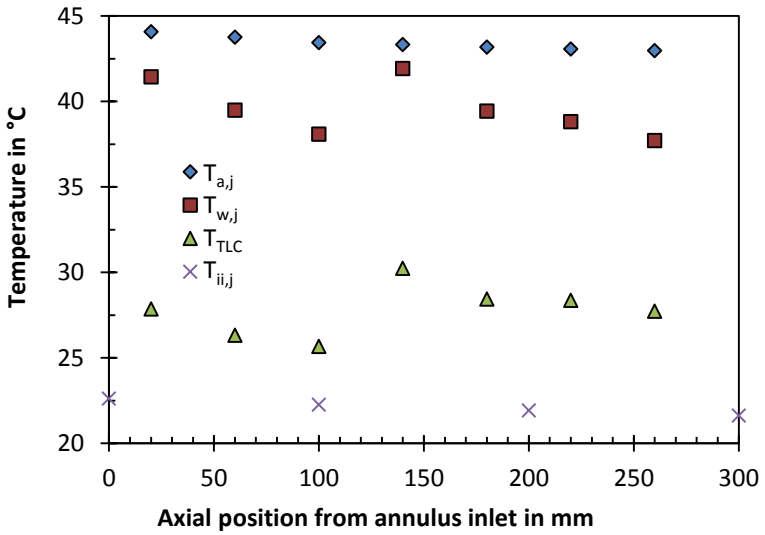


**Figure 33 – Bulk fluid and wall temperatures for CA 5 ($Re_a \approx 13\,600$)**

As the fluid flow rate was increased in the annulus, the surface temperature increased (therefore the temperature difference between the annular fluid and the wall decreased). The wall temperature is determined by the ratio of the heat transfer ability between the annular fluid and the inner fluid. This means that the annular heat transfer ability began playing a more dominant role in the overall heat transfer over the wall of tube 2. It is safe to assume that the inner fluid heat transfer coefficient remained relatively constant since the inner tube geometry remained constant along the length of the heat exchanger and the inner fluid was in the fully developed turbulent flow regime.

Figure 34 and Figure 35 are the same temperatures but for two cases of the heated annulus configuration.

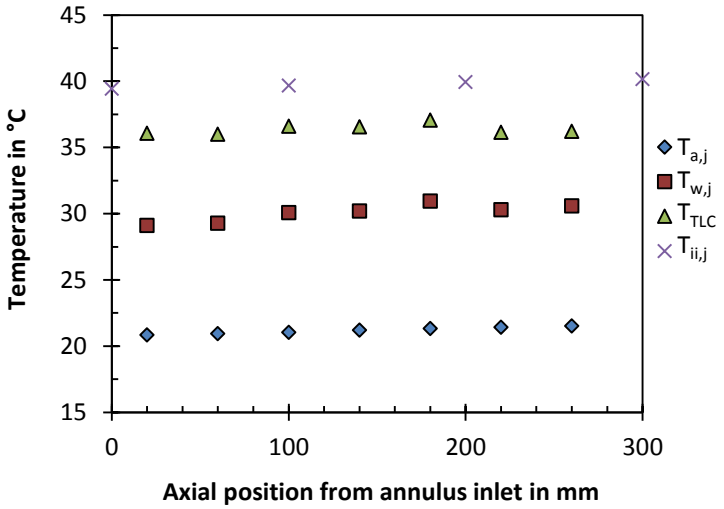


**Figure 34 – Bulk fluid and wall temperatures for heated annulus (Re ≈ 1 000)**

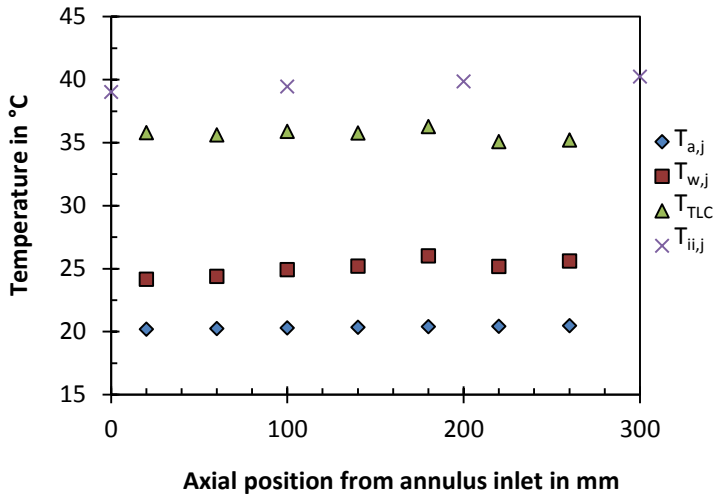


**Figure 35 – Bulk fluid and wall temperatures for heated annulus (Re ≈ 8 600)**

In order to heat up the fluid in the annulus, the bulk fluid temperature in the annulus had to be lower than that of the inner wall of the annular passage. This is illustrated in Figure 34 and Figure 35. When viewing Figure 32 to Figure 35, the difference between a cooled and a heated annulus can be seen as the temperature gradient over the tube wall switches directions. It also shows that the temperature profiles are very different between the two test cases. This is probably due to the difference in fluid viscosity (which will alter the fluid flow patterns) and the Prandtl number.

Figure 34 and Figure 35 show the same trend for the recorded temperatures as in the case of a cooled annulus. The surface temperature also comes closer to the annular bulk fluid temperature as the flow in the annulus is increased.

The areas where the temperature gradient over the resin layer was higher (the difference between $T_w$ and $T_{TLC}$) show that there is a larger heat flux since the temperature gradient over the resin layer is directly related to the heat transfer rate through it.

The closer the wall temperature to the annular bulk fluid temperature ($T_w$ and $T_{a,b}$), the higher the heat transfer coefficients ($h_{a,j}$) at that point. Therefore, at the points where the annulus bulk temperatures were close to the wall temperatures, the heat transfer coefficient (and therefore the Nusselt number) became larger. This shows that the heat transfer coefficients depend heavily on the wall temperature distribution.

## 5.4. Heat transfer rates per control volume (CV)

This section presents the results for the heat transfer rate to or from the annulus for the CVs close to the inlet of the heat exchanger. These results were calculated from the trend line fit of the measured temperature change within the inner fluid. The measuring rod temperatures were used for these calculations, therefore this data is available for the whole length of the heat exchanger, not just the portion covered in TLC's.

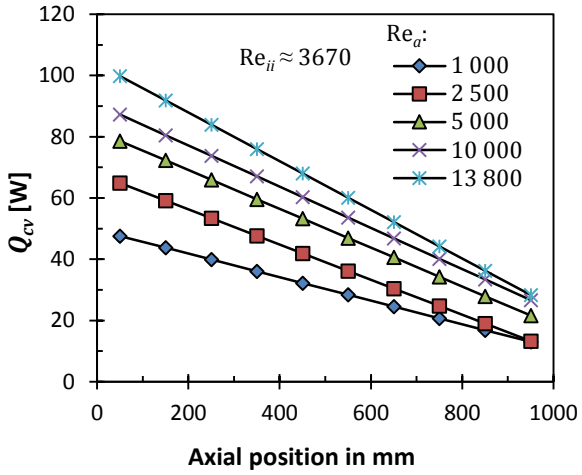


**Figure 36 – Heat transfer rates per CV for cooled annuli (Re$_{ii}$ ≈ 3670)**

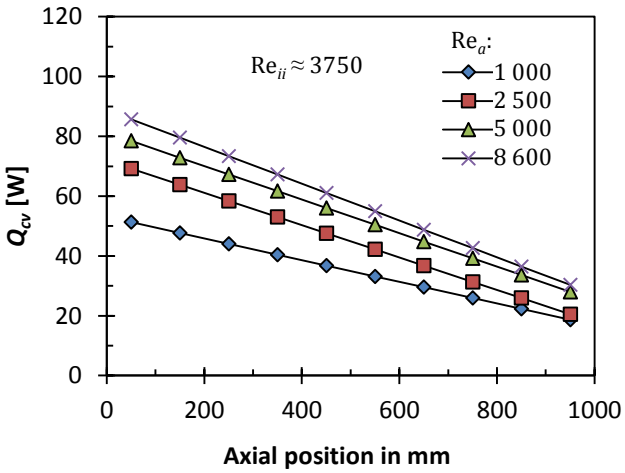


**Figure 37 – Heat transfer rates per CV for heated annulus (Re$_{ii}$ ≈ 3750)**

Figure 36 and Figure 37 show that the amount of heat transfer is larger per CV at the inlet of the heat exchanger and decreases per CV as one moves further away from the inlet.

It should be borne in mind that the inner fluid heat transfer coefficients should have been relatively constant along the length of the heat exchanger and that the only other factor which could influence the rate of heat transfer per CV, would be the heat transfer coefficient in the annulus. It stands to reason that the annular heat transfer capability must be larger at the inlet and decrease as the flow develops along the length of the heat exchanger, since the physical amount of heat transferred per CV decreases.

## 5.5. Heat transfer coefficients

This subsection contains the results for the local heat transfer coefficients obtained during the different test cases as outlined in Table 8 and Table 9. Figure 38 and Figure 39 show the local heat transfer coefficients for the CVs near the annular inlet of the heat exchanger. It should be noted that the first two data points for each of the flow rates only contain partial surface temperature data and might be inaccurate due to low surface area temperature sampling.

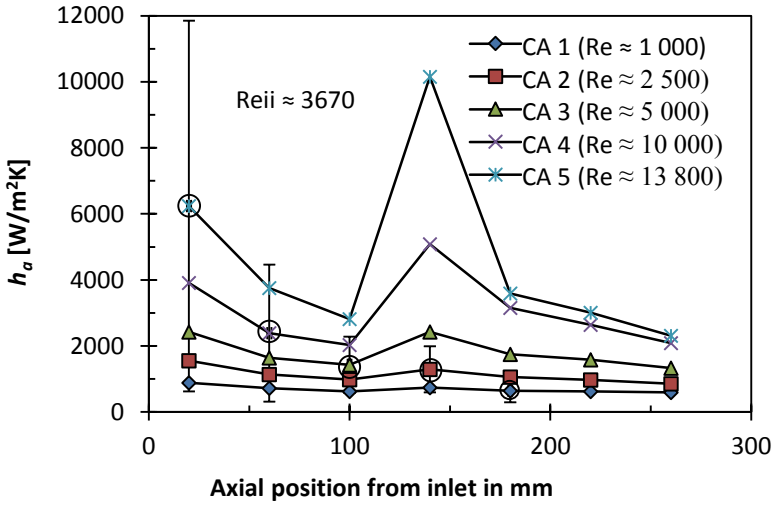


**Figure 38 – Local heat transfer coefficients at inlet for cooled annulus**

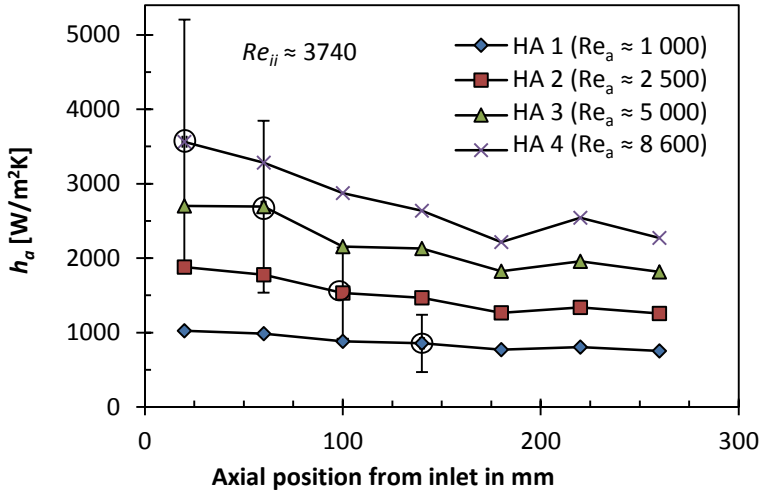


**Figure 39 – Local heat transfer coefficients at inlet for heated annulus**

The overall trend of the data is that the value of $h$ decreases in the axial direction further away from the inlet of the test section. Figure 38 shows that in the cases of the cooled annulus the maximum heat transfer coefficient is located 140 mm away from the inlet and then rapidly declines in an exponential fashion. In the cases of the heated annulus, this was not the case and no local peak at 140 mm was observed. The heat transfer coefficient did however decrease as one moved along the length of the heat exchanger. This is expected since the boundary layer grows along the length of the test section downstream from the annular inlet.

As the heat transfer coefficients rely on the surface temperature of the inner tube, the heat transfer coefficient will increase where the surface temperature approaches that of the annular fluid. The temperature distributions shown above showed large temperature gradients present at 140 mm which resulted in higher heat transfer coefficients.

The differences in heat transfer coefficient behaviour may be attributed to the fluid's Prandtl number (which is a function of the fluid viscosity). The difference in viscosity between the warmer and the colder fluid has an effect on the fluid flow paths. The differences in the Prandtl number also indicate the fluid's ability to draw heat from the heat transfer surface. These two differences also alter the surface temperature of the inner tube, resulting in the change in heat transfer coefficients.

## 5.6. Overall heat transfer coefficient

This subsection contains the local overall heat transfer coefficients for the whole length of the heat exchanger in the case of a cooled annulus. These coefficients are solely based on the temperature measurements taken from the measuring tube thermocouple stations in the measuring rod, and employ the logarithmic mean temperature differences over a CV. These temperatures were obtained from the trend line calculated from the measuring rod temperatures. Figure 40 and Figure 41 contain the local overall heat transfer data.

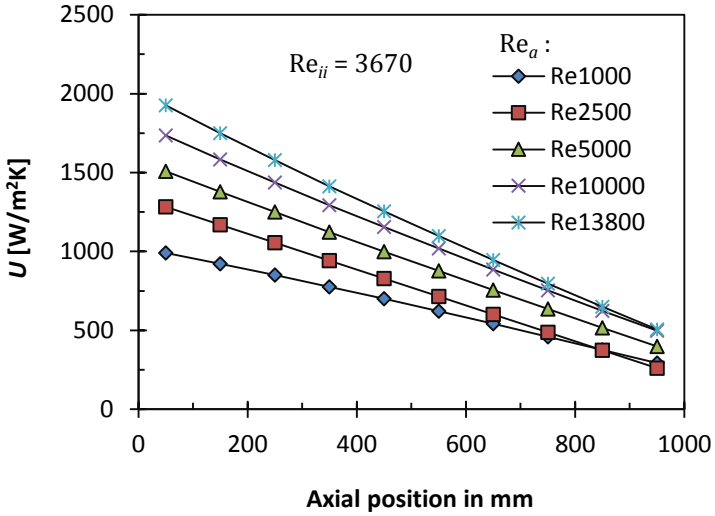


**Figure 40 – Local overall heat transfer coefficients for cooled annulus**

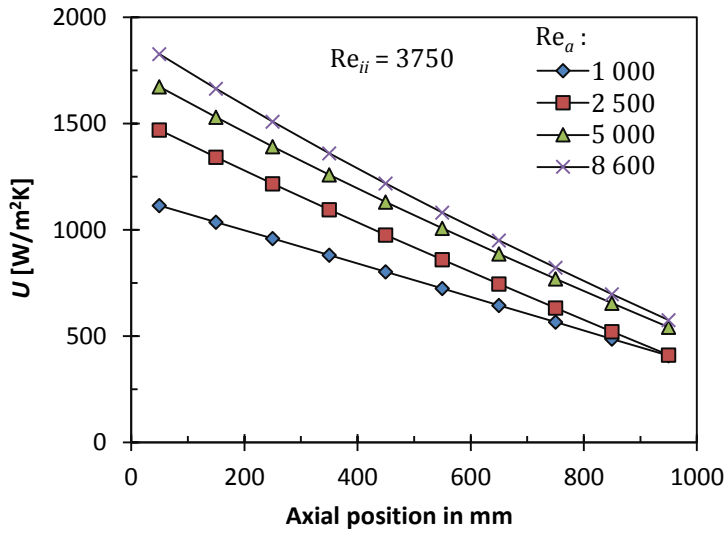


**Figure 41 – Local overall heat transfer coefficients for heated annulus**

Figure 40 and Figure 41 show a downward trend (almost linear) for the local overall heat transfer coefficient as one moves away from the annulus inlet. This shows that the overall heat transfer capability of the heat exchanger decreases as the flow develops in the annulus along the length of the heat exchanger and is highest at the inlet, where the flow is undeveloped. As this data is derived from the inner temperature trend line, it is not sensitive to locally higher or lower heat transfer coefficients but it is influenced by the heat transfer coefficient trend inside the heat exchanger. In contrast to this, the wall temperatures at the inlet are highly susceptible to local influences.

The change along the length was predicted to be more in the form of a logarithmic change (same shape as the inner rod temperature measurements). Since this heat exchanger is relatively short compared with the ones in the literature (normally around the 5 m mark), this data only represents a small portion of the data collected with long heat exchangers, where the logarithmic change in overall heat transfer coefficient should be noticeable. The

linear shape of the local overall heat transfer coefficient is probably due to observing only a small part of a larger logarithmic shape.

## 5.7. Averaged heat transfer coefficients vs. Reynolds number

This section contains the averaged heat transfer coefficients ($h$ & $U$). The $U$ values presented here are different from the previously presented $U$ values in that they take into account all the heat transferred in the heat exchanger and not only that of a specific CV contained inside the heat exchanger. This data enables one to compare the performance of the whole heat exchanger under the different flow conditions.

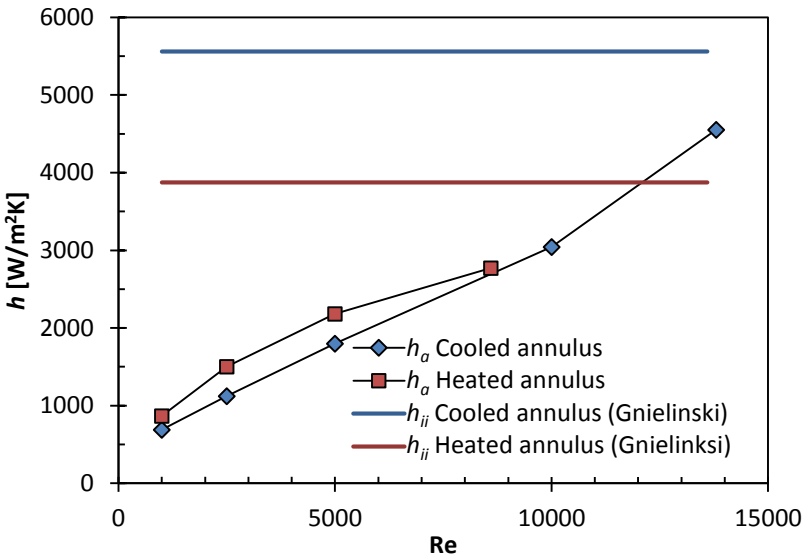


**Figure 42 – Relative annular and inner heat transfer coefficients**

The predicted heat transfer coefficients for the inner tube were calculated and presented (in the data analysis chapter) for both the cooled and heated annulus cases. These were calculated to be $h_{ii,CA} = 5\,560$ W/mK and $h_{ii,HA} = 3\,874$ W/mK, and are indicated in Figure 42. As the Reynolds number is kept constant for the inner tube for all tests, this is a constant value regardless of the Reynolds number for a cooled and heated annulus respectively.

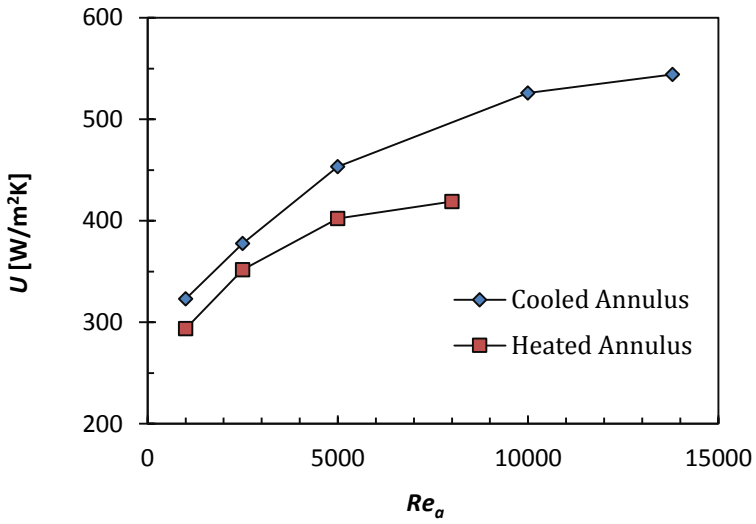


**Figure 43 – Averaged overall heat transfer coefficient vs. annular Reynolds number**

Figure 43 shows an increase in the overall heat transfer capability as the Reynolds number in the annulus is increased for both the cooled and heated annulus configurations. It seems that there may be a theoretical upper limit to the total heat exchange capability of the heat exchanger (without raising the inner Reynolds number) at $U$ around 580 W/mK. This theoretical upper limit is also described by Cengel [1] for specific flow conditions. This is due to the inner Reynolds number being kept constant and, as the heat transfer capability of the annular fluid increases (as the Reynolds number increases) and goes beyond that of the heat transfer capability of the inner tube, the lower heat transfer at the inner tube wall acts as a bottleneck for the total heat transfer. The total heat transfer is therefore limited by the lower heat transfer capability on either side.

## 5.8. Comparison with heat transfer coefficients from existing correlations

In order to compare the data obtained in this study with data in the existing literature, similar data should be used for comparison purposes. This mostly relates to data based on the same Reynolds numbers in the annulus and the annular diameter ratio (which is defined as $a = D_0/D_1$) which is equal to 0.54 in the present study.

As mentioned above, limited sources are available in the literature for local heat transfer measurements for heat exchangers of similar construction. The literature does predict that the heat transfer capability of the heat exchanger does not remain constant throughout the length of the heat exchanger, referring to the inlet and underdeveloped region of the heat exchanger. The literature also predicts that the heat transfer capability decreases as the boundary layer develops downstream from the inlet.

The correlations found in the literature, which are outlined in Table 1 (in the literature review section), are compared next with the average Nusselt numbers at the inlet region of the heat exchanger. The Nusselt number values presented in Table 12 were plotted against the correlations available as described previously. The correlation by Gnielinski was applied to a heat exchanger length of 0.28 m and 1 m respectively, to better compare the entrance

region heat transfer with that of the present study. The correlation by Gnielinski is the only correlation with a heat exchange length term in his correlation.

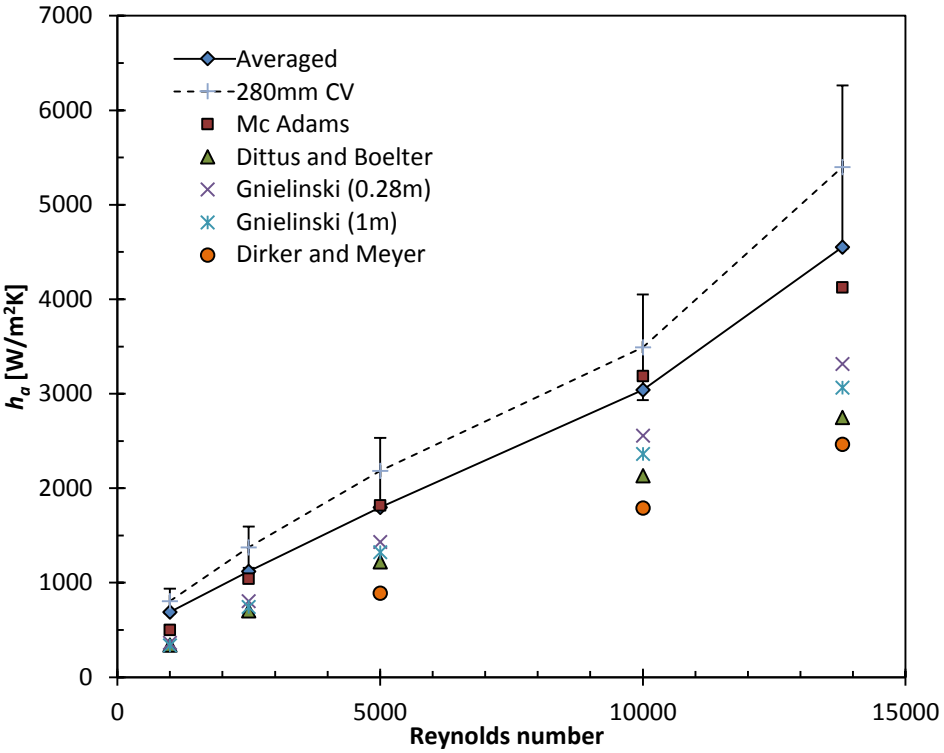


**Figure 44 – Comparison with correlations for a cooled annulus**

Figure 44 shows the averaged heat transfer coefficients for the seven CVs analysed at the inlet (notated as Averaged) in this study, as well as a single large CV (all seven CVs analysed as one, notated as 280 mm CV).

Of the currently available correlations, the one by McAdams [5] predicts the highest heat transfer coefficients. The rest of the correlations predict coefficients that are relatively close to one another. For this case of a cooled annulus, the results in this study are higher than those of most of the correlations by an average of 44% over the range presented above. Since the data presented here are only for the inlet region, it is reasonable to assume that the reason for the higher prediction by the experimentally obtained results is the higher heat transfer rates at the inlet, related to developing flow.

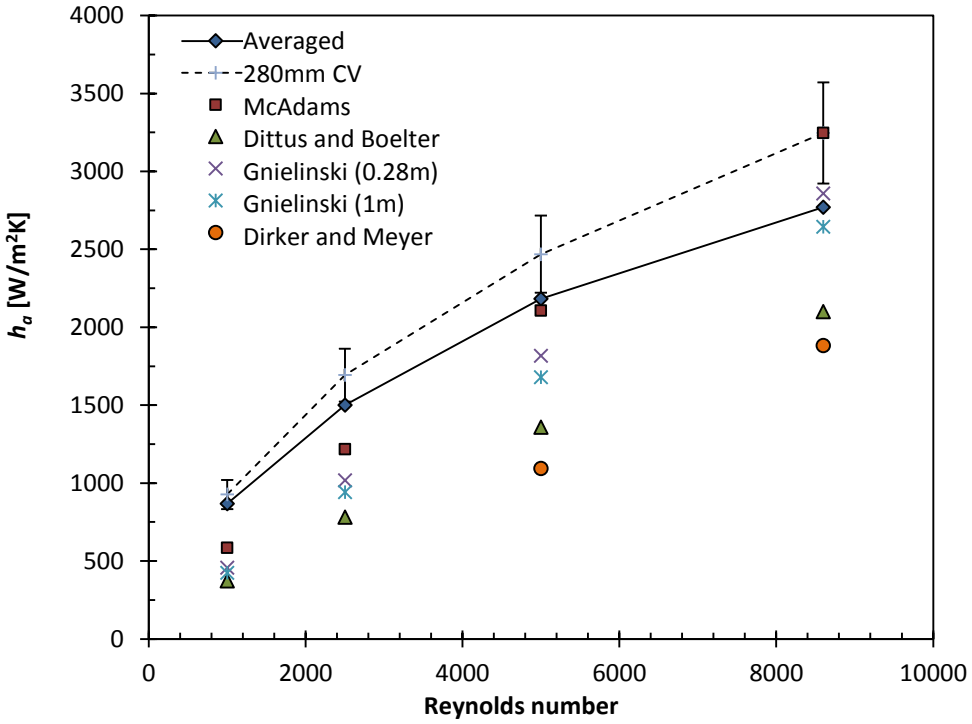


**Figure 45 – Comparison with correlation for a heated annulus**

As with the cooled annulus, the data obtained in this study for the data range shown above (Figure 45) is on average much higher (46%) than those of most of the correlations in the existing literature.

The correlation by Gnielinski for a heat exchanger of shorter length (0.28 m) did produce a slightly higher Nusselt number than for the whole (1 m long) heat exchanger, but only marginally (about 10%). This shows that Gnielinski does account somewhat for entrance effects with his correlation for heat transfer coefficients.

## 5.9. Summary of experimental results

The average value of the data points shown in Figure 38 to Figure 43 for each flow setting is given in Table 12. This shows the averaged predicted heat transfer values over the first 280 mm of the heat exchanger.

**Table 12 – Average heat transfer values at inlet regions**

| | Cooled annulus | | | | | Heated annulus | | | |
|---|---|---|---|---|---|---|---|---|---|
| $Re_a$ | 1 000 | 2 500 | 5 000 | 10 000 | 13 600 | 1 000 | 2 500 | 5 000 | 8 000 |
| $\bar{h}_{a,inlet}$ | 689 | 1121 | 1797 | 3041 | 4551 | 867 | 1501 | 2181 | 2770 |
| $\overline{Nu}_{a,inlet}$ | 15.5 | 25.2 | 40.4 | 69.8 | 102.2 | 20.5 | 35.5 | 54.6 | 65.6 |
| $\bar{U}_{overall}$ | 323 | 377 | 453 | 526 | 544 | 293 | 351 | 402 | 418 |

Table 12 therefore summarises the results of this investigation by presenting the averaged heat transfer coefficient values. It may be used as a comparison between the different flow rates and configurations tested. It shows that, on average, the heated annulus has a larger

heat transfer capability at the inlet than for a cooled annulus at a constant Reynolds number. The heat transfer capability increases as the annular Reynolds number increases.

# Chapter 6: Summary, Conclusions and Recommendations

This chapter contains some concluding remarks related to the current investigation.

## 6.1. Summary of findings

- Liquid crystal thermography may be used in a water-based heat exchanger element, provided that the thermochromic liquid crystals are adequately protected from the fluid.
- The temperature distributions extracted from the inlet regions of the heat exchanger vary by temperatures of up to 10 °C from one point to another in extreme cases which would be undetected when using thermocouples.
- Heat transfer and heat transfer coefficients do not remain constant over the length of the heat exchanger and are larger at the inlet and underdeveloped flow regions of a heat exchanger.
- The evidence suggests that the existing correlations under-predict heat transfer coefficients for short-length heat exchangers because they ignore the effects of the elevated heat transfer at the entrance region.

## 6.2. Summary of contributions

- A methodology was developed in order to facilitate the implementation of LCT for use in a tube-in-tube heat exchanger.
- A novel temperature change measurement technique is presented, although this technique has accuracy limitations when applied to small control volumes.
- It is shown that the heat transfer coefficients do not remain constant throughout the length of the heat exchanger.
- Some annular heat transfer coefficients are presented in this study.

## 6.3. Future research (recommendations)

This section contains the author's recommendations for future research in this particular topic for utilising LCT in tube-in-tube heat exchangers. Each recommendation is followed by a short rationale.

One method for lowering the uncertainties in the present study would be by enlarging the local CVs at the inlet by defining axially longer CVs. The temperature changes along the short CVs are very small, making the relative measured temperature change uncertainty very large. Another method could also include increasing the number of thermocouples per measuring station. This would lower the uncertainty of each of the measuring station readings as well as the trend line uncertainty.

Reducing the thickness of the protective coating over the TLCs could also reduce the uncertainty percentages. This was also a practical problem as it was not possible to measure

the thickness of the resin layer directly. One is only able to measure the diameter, not the concentricity of the coating. The thickness of the resin layer was assumed to be equally thick on either side, i.e. to have equal radii. The resin layer radius was therefore kept at ± 0.2 mm (for a diameter increase of ± 0.4 mm) to ensure that the TLCs would not be exposed at any point. The surface temperature uncertainty percentage would halve by halving the thickness to 100 microns. A more controlled and precise method for applying a thinner protective layer (such as the resin used in this study) over the TLCs would be very beneficial. This would lower the thermal resistance of the inner tube and result in lower uncertainties. If a resin with a higher thermal conductivity is used, the uncertainty will also be lowered.

Instead of using a second tube with the measuring tube forming a tube-in-tube heat exchanger, one could replace the inner tube with a heating element which has a constant heat flux. The heating element and an outer tube could form an annular passage. This would eliminate the need for the measuring stations inside the inner tube, which in turn would eliminate the need for calculating the heat transferred per CV ($\dot{Q}_{CV}$) from thermocouples. This is the largest source of error as determined by the uncertainty analysis. The heat transferred per CV may then be calculated as the total heat transferred by the heating element divided by the amount of CVs.

Subsequent tests should be run under similar conditions to the present study. This would be beneficial for observing the local heat transfer pattern at the inlet in order to confirm the erratic behaviour that is documented in the present study.

Another testable entity might be to see whether the total length of the heat exchanger has any effect on the heat transfer capability at the inlet. This could be tested by having multiple outlet ports for the annulus and seeing if the measured heat transfer coefficients change as the length is changed. This could test to see whether the downstream geometry has any effect on heat transfer at the inlet region.

Alternative inlet configurations could also be tested with the methodology developed in this study. By building different heat exchangers with the same annulus ratio but with different inlet configurations, one could see what difference the inlet configuration made to the heat transfer capability close to the inlet region and therefore to the total heat transfer of the heat exchanger. Other inlet configurations could include splitting the one inlet port into multiple ports around the circumference. Possibly unlimited inlet configurations could be imagined.

The experimental configuration could be changed to accommodate multiple cameras along the length of the setup, instead of only using one camera as in the present study. One practical problem faced in the present study was the rate at which the photographs could be taken. By incorporating multiple identical cameras along the length, less movement would needed, which should minimise the time needed to capture all the photographs required. This could also increase the amount of area that the thermography method could

cover. Care should be taken when setting up the lighting so that the extra light sources (needed for the extra cameras) would not influence the incident lighting angles. The author suggests using an automated computer program to switch on the light sources independently as they are needed and to control the lights as well as the cameras.

## 6.4. Conclusions

The technique of LCT was successfully employed in a tube-in-tube type heat exchanger for directly measuring tube wall temperatures. To this end, a customised heat exchanger was designed and built with a transparent outer tube. Images captured the surface of the inner tube wall and temperatures were extracted from these images.

The TLC temperatures were used to calculate the local heat transfer coefficients which had reasonable agreement with the current literature. By implementing this technique over multiple areas along the heat exchanger or covering the whole heat exchanger, the heat transfer coefficients could be determined along the whole length. LCT could be an invaluable tool for accurately measuring wall temperatures.

The calculated heat transfer coefficients were found to be inconsistent at the inlet region of the heat exchanger. The obtained coefficients had a reasonable agreement with data sources from the literature.

# Bibliography

[1] Y. A. Cengel, *Heat and mass transfer*, Third ed. New York: Mc Graw Hill, 2006.

[2] F. Systems. (2014, 10 June). *IR thermography primer*. Available: http://www1.infraredtraining.com/view/?id=40483

[3] C. Camci, *Introduction to liquid crystal thermography and a brief review of past studies*.

[4] J. Dirker and J. P. Meyer, "Convective heat transfer coefficients in concentric annuli", *Experimental heat and mass transfer,* vol. 17, pp. 19-29, 2005.

[5] W. H. McAdams, *Heat transmissions*, 3rd ed. New York, 1954.

[6] F. W. Dittus and L. M. K. Boelter, *Publications on engineering,* vol. 2, p. 443, 1930.

[7] V. Gnielinski, "Heat transfer coefficients for turbulent flow in concentric annular ducts", *Heat transfer engineering,* vol. 30, pp. 431-436, 2009.

[8] G. Maranzana, I. Perry, and D. Maillet, "Mini- and micro-channels: influence of axial conduction in the walls", *International journal of heat and mass transfer,* vol. 47, p. 3993–4004, 2004.

[9] W. R. v. Zyl, J. Dirker, and J. P. Meyer, "Single-phase convective heat transfer and pressure drop coefficients in concentric annuli", *Heat transfer engineering,* vol. 34, pp. 1112-1123, 06 Feb 2013.

[10] S. N. Singh, "Heat transfer by laminar flow in a cylindrical tube", *Applied sciences,* vol. 7, 1957.

[11] A. P. Sasmito, J. C. Kurnia, and A. S. Mujumdar, "Numerical evaluation of laminar heat transfer enhancement in nanofluid flow in coiled square tubes", *Nanoscale research letters,* vol. 6, p. 376, 2011.

[12] C. Y. Choi, "A boundary element solution approach for the conjugate heat transfer problem in themally developing region of a thick walled pipe", *Journal of mechanical science and technology,* vol. 20, pp. 2230-2241, 2006.

[13] M. E. Arici and O. Aydin, "Conjugate heat transfer in thermally developing laminar flow with viscous dissipation effects", *Heat mass transfer,* vol. 45, pp. 1199-1203, 2009.

[14] S. Cheroto, C. A. C. Santos, and S. Kakac, "Hybrid-analytical investigation of unsteady forced convection in parallel-plate channels for thermally developing flow", *Heat and mass transfer,* vol. 32, pp. 317-324, 1997.

[15] A. N. Smith and H. Nochetto, "Laminar thermally developing flow in rectangular channels and parallel plates: uniform heat flux", *Heat mass transfer,* vol. 50, 2014.

[16] H. H. Al-Ali and M. S. Selim, "Momentum and heat transfer in the entrance region of a parallel plate channel: developing laminar flow with constant wall temperature", *Applied scientific research,* vol. 51, pp. 663-675, 1993.

[17] P. K. Panigrahi. (2000, 1 April 2014). Colourful world of liquid crystals. *3(2)*. Available: http://www.iitk.ac.in/infocell/Archive/dirmar2/techno_crystals.html

[18] L. Hallcrest, "Handbook of thermochromic liquid crystal technology", RT006%20randtk_TLC_Handbook.pdf, Ed., ed. Glenview, Illinois: LCR Hallcrest, 1991.
[19] C. Camci, *Color recognition for temperature measurements on liquid crystal coated heat transfer surfaces*. Lecture Material.
[20] C. R. Smith, D. R. Sabatino, and T. J. Praisner, "Temperature sensing with thermochromic liquid crystals", *Experiments in fluids,* pp. 190-201, 2001.
[21] J. A. Stasiek and T. A. Kowalewski, "Thermochromic liquid crystals applied for heat transfer research", *Opto-electronics review,* vol. 10, pp. 1-10, 2002.
[22] H. Li, C. Xing, and M. J. Braun, "Natural convection in a bottom-heated top-cooled cubic cavity with a baffle at the median height: experiment and model validation", *Heat mass transfer,* vol. 43, pp. 895-905, 2007.
[23] T. R. Ogden and E. W. Hendricks, "Liquid crystal thermography in water tunnels", *Experiments in fluids,* vol. 2, pp. 65-66, 1984.
[24] J. Stasiek, M. Ciofalo, and M. Wierzbowski, "Experimental and numerical simulations of flow and heat transfer in heat exchanger elements using liquid crystal thermography", *Journal of thermal science,* vol. 13, pp. 133-137, 2044.
[25] L. M. Tam, H. K. Tam, A. J. Ghajar, and W. S. NG, "Heat transfer measurements for a horizontal micro-tube using liquid crystal thermography", in *International symposium on heat transfer and energy conservation*, 2012, pp. 62-66.
[26] B. K. Reddy and C. Balaji, "Estimation of temperature dependent heat transfer coefficient in a vertical rectangular fin using liquid crystal thermography", *International journal of heat and mass transfer,* vol. 55, pp. 3686-3693, 2012.
[27] M. Rao and S. Khandekar, "Simultaneously developing flows under conjugated conditions in a mini-channel array: liquid crystal thermography and computational simulations", *Heat transfer engineering,* vol. 30, pp. 751-761, 2009.
[28] R. E. Critoph, M. K. Holland, and M. Fisher, "Comparison of steady state and transient methods for measurement of local heat transfer in plate fin-tube heat exchangers using liquid crystal thermography with radiant heating", *International journal of heat and mass transfer,* vol. 42, pp. 1-12, 1999.
[29] M. K. Chyu, H. Ding, J. P. Downs, and F. O. Soechting, "Determination of local heat transfer coefficient based on bulk mean temperature using a transient liquid crystal technique", *Experimental thermal and fluid science,* vol. 18, p. 327-335, 1998.
[30] J. Rus, "Hsl-hsv models", Hsl_hsv_modles.svg, Ed., ed: GNU free documentation license, 2010.
[31] T. Moeslund, *Introduction to video and image processing*. New York: Springer, 2012.
[32] P. M. K. Jr and J. K. Eaton, "Angular effects on thermochromic liquid crystal thermography", *Experimental fluids,* vol. 43, pp. 929-937, 2007.

[33] Y. Rao and S. Zang, "Calibration and the measurement uncertainty of wide-band liquid crystal thermography ", *Measurement science and technology,* vol. 21, Article ID 015105, 2010.
[34] Y. Rao and Y. Xu, "Liquid crystal thermography measurement uncertainty analysis and its application heat transfer measurements", *Advances in condensed matter physics,* vol. 2012, Article ID 898104, 2012.
[35] A. C. E. o. T. Measurement, *Manual on the use of thermocouples in temperature measurement*, 4th ed.: ASTM International, 1993.
[36] C. O. Popiel and J. Wojtkowiak, "Simple formulas for thermophysical properties of liquid water for heat transfer calculations", *Heat transfer engineering,* vol. 19, pp. 87-101, 1998.
[37] Armacell. (2008, AP Armaflex sheet and roll insulation.
[38] D. D. L. Chung, "Materials for thermal conduction", *Applied thermal engineering,* vol. 21, pp. 1593-1605, 2001.
[39] V. Gnielinski, "New equations for heat and mass transfer in the turbulent flow in pipes and channels", *International chemical engineering,* vol. 16, pp. 359-368, 1975.
[40] S. Kline and F. McClintock, "Describing uncertainties in single-sample experiments", *Mechanical engineering,* vol. 75, pp. 2-8, 1969.
[41] R. J. Moffat, "Describing the uncertainties in experimental results", *Experimental thermal and fluid science,* pp. 3-17, 1988.

# Appendix A – Experimental design of thermal conductivity study of SP115 resin system

This study relied on wall temperature measurements obtained from tube 2. As stated previously, tube 2 has a resin layer over the TLCs in order to isolate it from the water. Resin has a very low thermal conductivity. The result is that there is a temperature gradient over the resin layer, so that the temperatures read from the TLCs between the resin and copper are not an accurate representation of the heat transfer surface temperature. It was therefore necessary to determine the thermal conductivity of the resin used in this study. An experiment was set up in order to determine the conductivity of the resin.

This experiment was based on the equation for radial heat conduction through a solid as given by Cengel [1]:

$$\dot{Q}_{cond,cyl} = 2\pi kL\left(\frac{T_2 - T_1}{\ln\left(\frac{r_2}{r_1}\right)}\right)$$

$L$ denotes the length of the cylinder, $T_2 - T_1$ is the temperature difference between radii $r_2$ and $r_1$ respectively. This equation may be rewritten so that $k$ is the subject; this was used to determine the thermal conductivity of the resin used in this study.

## Thermal study experimental design

A controlled amount of heat was added to the centre of a cylinder of cast resin with an outer diameter of 63 mm and a height of 211 mm. Thermocouples were placed at three different diameters inside the cylinder. All the thermocouples were placed in the middle with respect to the height of the cylinder. Figure 46 shows a schematic representation of the thermal conductivity study setup.

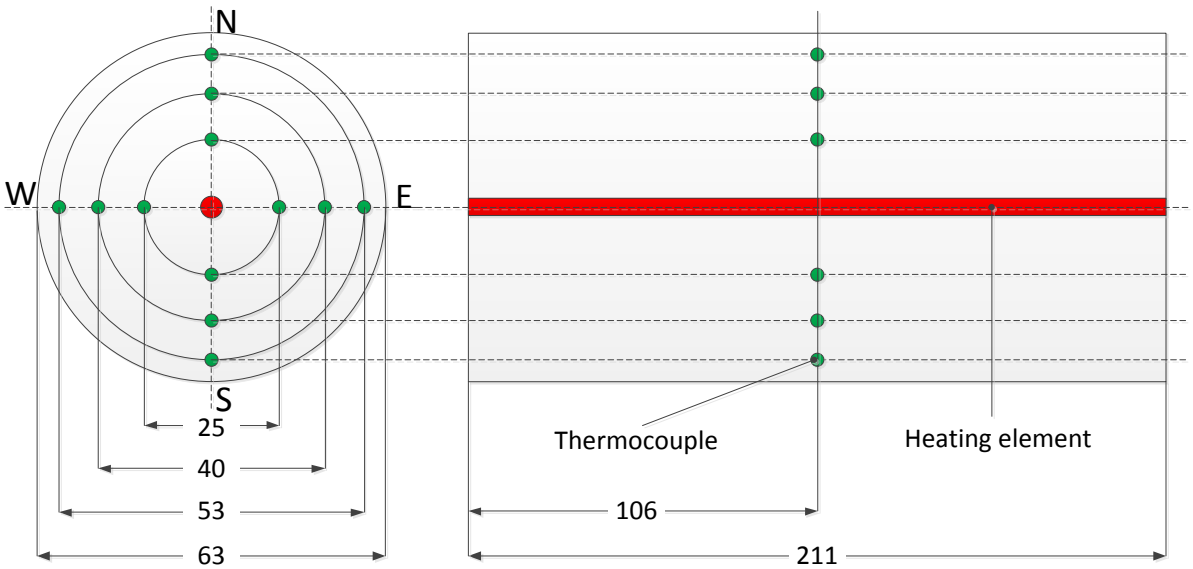


**Figure 46 – Thermocouple layout diagram of thermal conductivity experimental design**

The thermocouple wires were routed so that the wires remained at the same diameter as the positions of the thermocouples. This was done to minimise the thermal conductivity through the thermocouple wire itself as its thermal conductivity is much higher than that of the resin.

The ends of the resin cylinder were insulated in order to prevent the heat generated inside the core to flow in an axial direction, but to rather flow in the radial direction.

**Figure 47 – Photo of thermal conductivity setup**

## Determining thermal conductivity

One can calculate the thermal conductivity of the medium by using the equation for radial thermal conduction in a cylinder. Three rings of thermocouples were installed in this setup with the result that there were three different radii combinations on which the thermal conductivity could be calculated.

The heat generated by the heating wire was controlled by means of a power supply connected to the installed heating wire in the resin cylinder. Because the radii, the temperature difference measured, the length of the heating element and the heat added to the system are known, the thermal conductivity ($k$) is the only unknown. Rearranging the above equation gives:

$$k = \frac{\dot{Q}_{cond,cyl} \ln\left(\frac{r_2}{r_1}\right)}{2\pi L(T_2 - T_1)}$$

The temperatures were measured while the system was under steady operating conditions and were determined by observing the temperatures inside the resin cylinder over time. When the temperature did not vary by more than 0.1 °C over a period of two minutes, a set of temperatures ranging over 30 minutes was logged, just to be sure that the steady state had, in fact, been reached.

## Results of thermal conductivity study

Four different power settings were used for calculating the conductivity. Each of the power settings was given sufficient time to reach steady operating conditions (about 2 hours) before 30 minutes of thermocouple data was logged. Even so, some of the data displayed transient behaviour. After disregarding these two data sets, two data sets were still viable for use.

After investigating the temperatures obtained from the study, it was found that the temperatures measured on the first ring of thermocouples (located at the 25-mm diameter) did not correspond well with each other (they had a scatter of 2 °C). A decision was therefore taken to investigate each of the four directions (as depicted in Figure 46 and named after the four primary wind directions) individually.

The setup was investigated after the tests had been run in order to determine accurately the actual position of each of the thermocouples. Although all possible measures had been taken to ensure proper spacing, some shift did occur. It was therefore possible to obtain four sets of data (one for each wind direction) with three different radii each, resulting in a total of 12 $k$-values for each different heat influx value. The 12 $k$- values were averaged to give the values listed in Table 13 below:

**Table 13 – Thermal conductivity study of SP115 resin results**

| Heat added | Ave. temperature in resin cylinder | Thermal conductivity |
|---|---|---|
| 3.44 W | 36.4C | 0.218 W/mK |
| 2.97 W | 35.3C | 0.220 W/mK |
| Average | 35.8C | 0.219 W/mK |

It is clear from the data shown in Table 13 that the thermal conductivity of the resin used in the study is 0.219 W/mK. This data is used in the data analysis section used the data in Table 13 in order to calculate the heat transfer wall temperature on the annulus side.

The thermal conductivity of the resin used in this study is very low. This results in a temperature gradient over the thickness of the resin. This in turn had the result that the temperature measured using the TLCs cannot be directly used as the heat transfer surface temperature.

## Summary of thermal conductivity study

The thermal conductivity of the SP115 resin (used in this study as a protective layer for the TLC) was successfully determined. The thermal conductivity was found to be 0.219 W/mK. The process used ensured the high accuracy (within 2%) of the determined thermal conductivity value. The process utilised heat conduction through a cylinder in order to determine the $k$-value of the resin. A heating wire was run through the middle of a solid cylinder of resin with thermocouples spaced towards the outside of the cylinder. the Thermal conductivity could be calculated with the known heat input into the system and the measured temperatures at known radii.

# Appendix B – Uncertainty analysis

This appendix reports on the investigation of the method used to calculate the uncertainties of various entities in this study.

## Uncertainty theory

For each measurement, the measurement is described as the value of the measurement with its associated uncertainty band and is written mathematically as:

$$x_i = x_i(measured) \pm \delta x_i$$

where $\delta x_i$ is the uncertainty of the instrument being investigated. The actual value will therefore lie somewhere between $x_i - \delta x_i$ and $x_i + \delta x_i$. This ensures a 95% confidence level. This is the uncertainty described for a single-value experiment.

Moffat [41] describes the error of a multi-variable experiment in terms of the separate uncertainties. Let $R$ be the result of an experiment defined by:

$$S = f(x_1, x_2, x_3, \dots, x_n)$$

Kline and McClintock [40] show that the uncertainty of such experiments may be accurately described by the root sum of the error contribution of each of the respective variables. They show that the effect of a measurement error for a single experiment may be given by the partial differential in the form:

$$\delta S_{xi} = \frac{\partial R}{\partial x_i} \delta x_i$$

Expanding this equation to account for all the variables accountable for the uncertainty gives:

$$\delta S = \left\{ \sum_{i=0}^{n} \left( \frac{\partial R}{\partial x_i} \delta x_i \right)^2 \right\}^{0.5}$$

This is the basic equation used for the uncertainty analysis in the present study. This equation takes into account each separate measurement error and facilitates the calculation of the contribution of each.

## Quantifying uncertainties

Table 14 lists the uncertainties ($\delta$) of the equipment used in this study.

**Table 14 – Uncertainty of equipment used**

| Equipment | Range | Uncertainty |
|---|---|---|
| Thermocouple | -200 – 350 °C | $\pm$ 0.11 °C |
| TLCs | 20 – 41 °C | $\pm$ 0.53 °C |
| Flow meter | 0.015 – 0.603 kg/s | 0.11% of reading |
| Watt meter | 0 – 150 W | 1.9% of reading |
| Vernier calliper | 0 – 200 mm | $\pm$ 0.02 mm |

Table 15 lists the uncertainties of the thermophysical properties of water, from the equations proposed by Popiel and Wojtkowiak [36].

**Table 15 – Uncertainties of thermophysical properties of water approximations**

| Entity | Range | Uncertainty |
|---|---|---|
| $C_p$ equation | 0 °C – 150 °C | 0.06% |
| $k$ equation | 0 °C – 150 °C | 2.00% |
| $\rho$ equation | 0 °C – 150 °C | 0.04% |
| $\mu$ equation | 0 °C – 150 °C | 1.00% |

The uncertainties described by a percentage have to be converted to the same units as those in which the variable appears. This is done by simply taking a percentage of the physical value and assigning that value to the uncertainty.

## Uncertainty of a trend line

The standard error of a data sample is defined as follows:

$$SE_x = \frac{s}{\sqrt{n}}$$

The standard error is given by the Excel function “Linest” by plotting the measured values on the x-axis against curve-fit values on the y-axis. This gives a linear relationship between the measured and the curve fit values. From this the standard error (which is defined above) is calculated. This standard error is then used as the measured error for one of the thermocouple stations in the measuring tube (tube 3).

## Sample uncertainty calculation

This section presents the general solution for the uncertainty of the heat transfer coefficient and Nusselt number. To calculate the uncertainty of the hydraulic diameter:

$$D_{h,a} = D_0 - D_1$$

By applying the formula for $\delta R$:

$$\delta D_{h,a} = \{(\delta D_0)^2 + (-\delta D_1)^2\}^{\frac{1}{2}}$$

$$\delta D_{h,a} = \{0.02^2 + 0.02^2\}^{\frac{1}{2}} = 0.0283\ mm = 0.0000283\ m$$

Next the uncertainty of the heat transfer surface area is calculated:

$$A_w = \pi L_{cv} D_1$$

Which becomes:

$$\delta A_w = \{(\pi L_{cv} \delta D_1)^2 + (\pi D_1 \delta L_{cv}\}^{\frac{1}{2}}$$

$$\delta A_w = \left\{\left(\pi(0.04)(0.00002)\right)^2 + \left(\pi(0.01945)(0.00002)\right)^2\right\}^{\frac{1}{2}} = 0.00000279\ m^2$$

Since the uncertainties for the correlations for $C_p$, $\rho$, $k$ and $\mu$ are given in percentage, one has to convert this into coherent units by taking the percentage of the current value. The same goes for the mass flow, voltage and Ammeter readings:

$$\delta C_p = (\%error) C_p$$

$$\delta \rho = (\%error) \rho$$

$$\delta k = (\%error) k$$

$$\delta \mu = (\%error) \mu$$

$$\delta \dot{m} = (\%error) \dot{m}$$

$$\delta V = (\%error) V$$

$$\delta I = (\%error) I$$

For a set of thermocouples located at a single measuring station, the uncertainty of the set of thermocouples is:

$$\delta T_{ii,in} = \sqrt{\frac{1}{n}} \delta T_{thermocouple}$$

With four thermocouples located at each of the ports of the heat exchanger:

$$\delta T_{ii,in} = \sqrt{\frac{1}{4}}(0.11) = 0.055°C$$

The temperature difference over two subsequent CV boundaries is given by:

$$\Delta T_{cv} = T_{ii,n} - T_{ii,n-1}$$

For a certain number of thermocouples per station ($n$), it becomes:

$$\delta \Delta T_{cv} = \left\{ \left( \sqrt{\frac{1}{n}} \delta T_{thermocouple} \right)^2 + \left( -\sqrt{\frac{1}{n}} \delta T_{thermocouple} \right)^2 \right\}^{\frac{1}{2}}$$

By using the uncertainties of a trend line, it becomes:

$$\delta \Delta T_{cv} = \{(SE_x)^2 + (-SE_x)^2\}^{\frac{1}{2}}$$

From the temperature difference, the amount of heat transferred per CV may be calculated using:

$$\dot{Q}_{ii,cv} = \dot{m}_{ii} C_{p,ii} \Delta T_{ii,cv}$$

$$\delta \dot{Q}_{cv} = \left\{ \left( \delta \dot{m} C_p \Delta T_{cv} \right)^2 + \left( \dot{m} \delta C_p \Delta T_{cv} \right)^2 + \left( \dot{m} C_p \delta \Delta T_{cv} \right)^2 \right\}^{\frac{1}{2}}$$

In order to estimate the bulk fluid temperature in the annulus, the following formula was used:

$$\dot{Q}_{ii,cv} = \dot{Q}_{a,cv}$$

$$\dot{m}_{ii} C_{p,ii} \Delta T_{ii,cv} = \dot{m}_a C_{p,a} \Delta T_{a,cv}$$

$$T_{n+1} = T_n + \frac{\dot{m}_{ii} C_{p,ii} \Delta T_{ii,cv}}{\dot{m}_a C_{p,a}}$$

$$\delta T_{a,n+1} = \left\{ \delta T_{a,n}^2 + \left( \frac{\delta \dot{m}_{ii} C_{p,ii} \Delta T_{ii,cv}}{\dot{m}_a C_{p,a}} \right)^2 + \left( \frac{\dot{m}_{ii} \delta C_{p,ii} \Delta T_{ii,cv}}{\dot{m}_a C_{p,a}} \right)^2 + \left( \frac{\dot{m}_{ii} C_{p,ii} \delta \Delta T_{ii,cv}}{\dot{m}_a C_{p,a}} \right)^2 + \left( \frac{\dot{m}_{ii} C_{p,ii} \Delta T_{ii,cv}}{\dot{m}_a^2 C_{p,a}} \delta \dot{m}_a \right)^2 + \left( \frac{\dot{m}_{ii} C_{p,ii} \Delta T_{ii,cv}}{\dot{m}_a C_{p,a}^2} \delta C_{p,a} \right)^2 \right\}^{\frac{1}{2}}$$

To calculate the temperature rise over the resin layer:

$$\Delta T_{resin} = \frac{\dot{Q}\ \tau_{resin}}{k_{resin} A_w}$$

The thickness of the resin can be measured within an accuracy of 0.02 mm ($\delta\tau_{resin}$) and the thermal conductivity of the resin was determined within 0.219 W/mK ($\delta k$):

$$\delta\Delta T_{resin} = \left\{\left(\frac{\delta\dot{Q}\tau_{resin}}{k_{resin}A_w}\right)^2 + \left(\frac{\dot{Q}\delta\tau_{resin}}{k_{resin}A_w}\right)^2 + \left(\frac{\dot{Q}\tau_{resin}}{k_{resin}^2 A_w}\delta k_{resin}\right)^2 + \left(\frac{\dot{Q}\tau_{resin}}{k_{resin}A_w^2}\delta A_w\right)^2\right\}^{\frac{1}{2}}$$

Another temperature uncertainty needed is the uncertainty of average temperature reading by the TLC coated surface; this is similar to a set of n thermocouples:

$$\delta T_w = \frac{1}{\sqrt{n}}\delta T_{TLC}$$

One is now able to calculate the heat transfer coefficient ($h$):

$$h_a = \frac{\dot{Q}_{cv}}{A_w\left(T_w + \Delta T_{resin} - T_{a,b}\right)}$$

To simplify things, the term containing all the temperatures was investigated separately by defining:

$$T = \left(T_w + \Delta T_{resin} - T_{a,b}\right)$$

$$\delta T = \left\{(\delta T_w)^2 + (\delta\Delta T_{resin})^2 + \left(-\delta T_{a,b}\right)^2\right\}^{\frac{1}{2}}$$

The heat transfer equation then simplifies to:

$$h_a = \frac{\dot{Q}}{A_w T}$$

$$\delta h_a = \left\{\left(\frac{\delta\dot{Q}}{A_w T}\right)^2 + \left(\frac{\dot{Q}}{A_w^2 T}\delta A_w\right)^2 + \left(\frac{\dot{Q}}{A_w T^2}\delta T\right)\right\}^{\frac{1}{2}}$$

From this, the Nusselt number may be calculated:

$$Nu = \frac{hD_h}{k_a}$$

$$\delta Nu = \left\{\left(\frac{\delta h D_h}{k_a}\right)^2 + \left(\frac{h\delta D_h}{k_a}\right)^2 + \left(\frac{hD_h}{k_a^2}\delta k_a\right)^2\right\}^{\frac{1}{2}}$$

## Resin thermal conductivity uncertainty

The equation used to calculate the thermal conductivity of the resin is repeated below:

$$k = \frac{\dot{Q}_{cond,cyl} \ln\left(\frac{r_2}{r_1}\right)}{2\pi L(T_2 - T_1)}$$

There are four variables to be accounted for, $\dot{Q}_{cond,cyl}$, $\ln(r_2/r_1)$, $L$ and $(T_2 - T_1)$. The individual uncertainties of each of these variables are listed below:

**Table 16 – Variable uncertainties for resin conductivity**

| Variable | Measured by | Uncertainty |
|---|---|---|
| $\dot{Q}_{cond,cyl}$ | Power supply | ± 1% |
| $\ln(r_2/r_1)$ | Vernier Calliper | ± 0.0098 |
| $L$ | Vernier Calliper | ± 0.01 mm |
| $(T_2 - T_1)$ | Thermocouples | ± 0.16 C |

The uncertainty analysis for each calculated $k$ value then becomes:

$$\delta k = \left\{\left(\frac{\delta\dot{Q}\ln(r_2/r_1)}{2\pi L\Delta T}\right)^2 + \left(\frac{\dot{Q}\delta\ln(r_2/r_1)}{2\pi L\Delta T}\right)^2 + \left(\frac{\dot{Q}\ln(r_2/r_1)}{2\pi L^2\Delta T}\delta L\right)^2 + \left(\frac{\dot{Q}\ln(r_2/r_1)}{2\pi L\Delta T}\delta\Delta T\right)^2\right\}^{0.5}$$

The above equation gives a combined uncertainty of 2% for all the data gathered.

## Summary of calculated uncertainty values

This section contains the uncertainty values calculated. These values are of interest for gauging the accuracy of the data obtained. These uncertainties include the magnitude error of measured temperatures, LCT, the thermal conduction study and heat transfer coefficient uncertainties.

Below is a summary of the uncertainties for some common calculated values:

**Table 17 – Common calculated entities uncertainties**

| Entity | Uncertainty |
|---|---|
| Polynomial approximation of temperature | In the region of 0.05 °C, depending on fit |
| Temperature difference over two points | In the region of 0.07 °C, depending on fit |
| Single LCT pixel | $\pm$ 0.68 °C |
| Average surface temperature from LCT | $\pm$ 0.03 °C |
| Inlet and outlet temperature (four thermocouples) | $\pm$ 0.05 °C |
| Annulus bulk temperature prediction | $\pm$ 0.18 °C |
| Resin thermal conductivity | $\pm$ 2% |

## Cooled annulus uncertainties

This section contains the uncertainties calculated for the case of a cooled annulus. It tabulates the uncertainties for heat transfer measurement, the temperature gradient over the resin and all the calculated heat transfer coefficients.

**Table 18 – Tabulated uncertainties of cooled annulus results**

| Re in annulus | 1 000 | 2 500 | 5 000 | 10 000 | 13 600 |
|---|---|---|---|---|---|
| $\delta\dot{Q}_{cv}$ [%] | 49 | 38 | 32 | 29 | 26 |
| $\delta\Delta T_{resin}$ [°C] | 3.1 | 3.1 | 3.1 | 3.1 | 3.2 |
| $\delta h_{local}$ [%] | 57 | 54 | 60 | 87 | 123 |
| $\delta U$ [%] | 6 | 9 | 4 | 3 | 3 |

## Heated annulus uncertainties

This section contains all the same uncertainties as listed for the cooled annulus case, but for the case of a heated annulus.

**Table 19 – Tabulated uncertainties of heated annulus results**

| Re in annulus | 1 000 | 2 500 | 5 000 | 8 000 |
|---|---|---|---|---|
| $\delta\dot{Q}_{cv}$ [%] | 36 | 28 | 24 | 22 |
| $\delta\Delta T_{resin}$ [°C] | 2.2 | 2.2 | 2.2 | 2.2 |
| $\delta h_{local}$ [%] | 45 | 40 | 43 | 46 |
| $\delta U$ [%] | 7 | 4 | 3 | 3 |

The results listed in Table 19 show significantly lower uncertainties for heated annulus as in the case of the cooled annulus. One explanation for this that the heat transfer per CV is lower. The physical size of the heat transfer variable also plays a direct role in the calculated uncertainties of other variables. This is apparent when looking at the uncertainty for the temperature gradient over the resin layer: lower $\dot{Q}$, lower $\delta\Delta T_{resin}$.

## Explanation of large uncertainties

The main source of error originates from the temperature measurements inside tube 3.

Although the standard error from the polynomial fit is in the order of 0.023 °C, the temperature change may only be estimated within ± 0.033 °C. This is also quite low but considering that the actual temperature change over a CV is 0.15° C (in the best-case scenario with $Re_a$ = 13 800), this already introduces a measurement error of 22%.

By further calculating the heat transfer per CV based on this temperature measurement, the heat transfer per CV may only be estimated within an accuracy of about 26%. The annulus's bulk fluid temperature, temperature gradient over the resin and the heat transfer coefficients are based on of the amount of heat transferred in a CV. All of these entities are calculated with a value which only has a 26% accuracy, therefore none of these entities can be calculated within a better accuracy. This is the reason that the accuracy of the calculated heat transfer coefficients is inflated so highly.

# Appendix C – Additional data

This appendix contains additional data sets which did not appear in the main body of the dissertation. These data sets include surface temperature data, bulk fluid and wall temperature graphs and temperatures measured by tube 3.

## Wall temperature distributions

The temperature of the surface of tube 2 may be directly measured by the TLC coating applied to it. This section presents the temperature distributions obtained while using the LCT technique. The temperatures presented here are based on the actual interpreted values for the LCT and not representative of the heat transfer wall temperature. The wall temperature used in the heat transfer calculations take into account the temperature gradient present over the TLC protective resin layer.

The data is presented as though the pipe were slit open at the bottom along the length of the heat exchanger and flattened out. The degrees column indicates the angular position on which the photo was taken relative to the inlet of the annular passage (which sits at 0°). The numbers displayed directly under the heading are the distance from the annular passage inlet. The open cells indicate the inlet of the heat exchanger as these parts could not be imaged due to interference from the inlet port.

| | Cooled annulus 1 (CA 1) | | | | | | |
|---|---|---|---|---|---|---|---|
| deg\x | 20 mm | 60 mm | 100 mm | 140 mm | 180 mm | 220 mm | 260 mm |
| -144° | 26.1 | 24.7 | 23.8 | 25.4 | 25.0 | 24.6 | 24.6 |
| -108° | 26.3 | 24.5 | 23.3 | 25.3 | 24.7 | 24.5 | 24.6 |
| -72° | 26.7 | 24.5 | 23.0 | 25.2 | 24.4 | 24.1 | 24.1 |
| -36° | | | 23.1 | 24.9 | 24.4 | 23.8 | 24.1 |
| 0° | | | 23.1 | 25.0 | 24.5 | 23.9 | 24.0 |
| 36° | | | 23.0 | 25.0 | 24.5 | 24.4 | 24.6 |
| 72° | 26.4 | 24.3 | 23.2 | 25.6 | 24.8 | 24.6 | 24.6 |
| 108° | 26.3 | 24.6 | 23.6 | 26.9 | 25.6 | 25.1 | 25.1 |
| 144° | 26.5 | 25.2 | 23.7 | 27.4 | 26.5 | 25.4 | 25.2 |
| 180° | 26.7 | 24.5 | 24.1 | 26.0 | 24.7 | 25.3 | 24.8 |

| | Cooled annulus 2 (CA 2) | | | | | | |
|---|---|---|---|---|---|---|---|
| deg\x | 20 mm | 60 mm | 100 mm | 140 mm | 180 mm | 220 mm | 260 mm |
| -144° | 27.0 | 25.3 | 24.2 | 27.3 | 27.1 | 26.7 | 25.3 |
| -108° | 27.1 | 25.0 | 24.2 | 27.5 | 26.2 | 26.0 | 25.9 |
| -72° | 27.1 | 24.9 | 24.5 | 27.0 | 25.4 | 25.3 | 25.1 |
| -36° | | | 24.7 | 26.5 | 25.1 | 24.9 | 24.9 |
| 0° | | | 24.2 | 26.2 | 25.0 | 24.8 | 24.8 |
| 36° | | | 24.0 | 26.2 | 25.2 | 25.0 | 24.9 |
| 72° | 27.1 | 24.7 | 24.3 | 27.0 | 25.5 | 25.3 | 25.0 |
| 108° | 27.0 | 25.0 | 24.5 | 27.9 | 26.7 | 26.3 | 25.8 |
| 144° | 27.3 | 26.4 | 25.0 | 30.4 | 28.3 | 27.9 | 27.4 |
| 180° | 27.5 | 25.0 | 24.9 | 28.8 | 27.8 | 27.6 | 26.2 |

| | Cooled annulus 3 (CA 3) | | | | | | |
|---|---|---|---|---|---|---|---|
| deg\x | 20 mm | 60 mm | 100 mm | 140 mm | 180 mm | 220 mm | 260 mm |
| -144° | 27.5 | 25.1 | 25.2 | 29.4 | 28.3 | 27.7 | 27.0 |
| -108° | 27.4 | 25.0 | 24.7 | 28.7 | 27.3 | 27.5 | 27.1 |
| -72° | 27.5 | 25.1 | 24.7 | 28.1 | 26.2 | 26.3 | 25.9 |
| -36° | | | 25.2 | 27.2 | 25.8 | 25.1 | 25.4 |
| 0° | | | 25.1 | 27.2 | 25.8 | 25.3 | 25.3 |
| 36° | | | 24.6 | 27.2 | 26.0 | 25.9 | 25.4 |
| 72° | 27.3 | 25.3 | 24.3 | 28.0 | 27.0 | 27.1 | 26.3 |
| 108° | 27.3 | 24.9 | 24.8 | 30.4 | 28.5 | 29.3 | 27.9 |
| 144° | 27.5 | 25.3 | 24.9 | 32.4 | 30.9 | 30.9 | 29.7 |
| 180° | 27.5 | 27.1 | 25.8 | 30.3 | 29.1 | 29.5 | 27.7 |

| | Cooled annulus 4 (CA 4) | | | | | | |
|---|---|---|---|---|---|---|---|
| deg\x | 20 mm | 60 mm | 100 mm | 140 mm | 180 mm | 220 mm | 260 mm |
| -144° | 27.5 | 25.6 | 25.3 | 30.4 | 29.7 | 28.1 | 27.8 |
| -108° | 27.3 | 25.3 | 24.7 | 29.5 | 27.9 | 27.8 | 27.7 |
| -72° | 27.3 | 25.4 | 24.9 | 28.5 | 26.7 | 26.5 | 26.4 |
| -36° | | | 25.5 | 27.3 | 26.3 | 25.2 | 26.0 |
| 0° | | | 25.2 | 27.4 | 26.2 | 25.6 | 25.9 |
| 36° | | | 24.9 | 27.5 | 26.6 | 26.3 | 25.9 |
| 72° | 27.1 | 25.4 | 24.8 | 28.4 | 27.6 | 27.6 | 27.2 |
| 108° | 27.2 | 26.2 | 25.0 | 31.2 | 29.8 | 30.3 | 28.8 |
| 144° | 27.4 | 27.2 | 25.1 | 33.2 | 32.0 | 32.5 | 31.1 |
| 180° | 27.2 | 25.3 | 26.0 | 31.4 | 30.7 | 30.7 | 28.8 |

| | Cooled annulus 5 (CA 5) | | | | | | |
|---|---|---|---|---|---|---|---|
| deg\x | 20 mm | 60 mm | 100 mm | 140 mm | 180 mm | 220 mm | 260 mm |
| -144° | 27.8 | 27.2 | 24.7 | 29.2 | 26.6 | 26.4 | 26.6 |
| -108° | 27.7 | 26.1 | 24.9 | 31.3 | 27.9 | 28.0 | 27.8 |
| -72° | 27.7 | 25.9 | 26.0 | 31.1 | 30.0 | 29.0 | 28.2 |
| -36° | | | 27.3 | 32.5 | 30.6 | 31.7 | 29.1 |
| 0° | | | 25.6 | 34.1 | 32.3 | 32.7 | 31.2 |
| 36° | | | 26.2 | 32.1 | 30.3 | 31.0 | 29.5 |
| 72° | 27.6 | 25.2 | 26.0 | 29.6 | 27.5 | 27.7 | 27.2 |
| 108° | 27.8 | 25.9 | 25.5 | 27.6 | 26.6 | 26.3 | 26.0 |
| 144° | 28.1 | 27.9 | 25.3 | 27.5 | 26.3 | 25.6 | 25.8 |
| 180° | 28.2 | 26.1 | 25.2 | 27.5 | 26.4 | 25.2 | 25.9 |

| | Heated annulus 1 (HA 1) | | | | | | |
|---|---|---|---|---|---|---|---|
| deg\x | 20 mm | 60 mm | 100 mm | 140 mm | 180 mm | 220 mm | 260 mm |
| -144° | 36.0 | 35.9 | 36.6 | 36.0 | 36.9 | 34.6 | 35.1 |
| -108° | 36.0 | 36.0 | 36.6 | 36.5 | 37.0 | 36.2 | 36.2 |
| -72° | 36.5 | 36.3 | 36.8 | 36.7 | 37.0 | 36.5 | 36.4 |
| -36° | | | 37.0 | 36.5 | 37.2 | 36.0 | 36.6 |
| 0° | | | 36.9 | 36.8 | 37.3 | 36.6 | 36.6 |
| 36° | | | 36.8 | 36.8 | 37.4 | 36.7 | 36.6 |
| 72° | 36.3 | 36.4 | 36.4 | 36.9 | 37.3 | 36.7 | 36.6 |
| 108° | 36.0 | 35.6 | 36.6 | 36.8 | 37.1 | 36.6 | 36.5 |
| 144° | 35.9 | 35.9 | 35.8 | 36.7 | 36.9 | 36.1 | 36.2 |
| 180° | 35.8 | 36.0 | 36.5 | 36.0 | 36.6 | 35.5 | 35.3 |

| | Heated annulus 2 (HA 2) | | | | | | |
|---|---|---|---|---|---|---|---|
| deg\x | 20 mm | 60 mm | 100 mm | 140 mm | 180 mm | 220 mm | 260 mm |
| -144° | 35.9 | 35.7 | 36.3 | 35.7 | 36.3 | 34.0 | 34.2 |
| -108° | 35.9 | 35.8 | 36.5 | 36.1 | 36.6 | 35.8 | 35.6 |
| -72° | 36.3 | 36.3 | 36.7 | 36.4 | 36.8 | 36.2 | 36.1 |
| -36° | | | 36.8 | 36.3 | 36.9 | 35.9 | 36.3 |
| 0° | | | 36.8 | 36.5 | 37.0 | 36.4 | 36.4 |
| 36° | | | 36.6 | 36.5 | 37.0 | 36.3 | 36.2 |
| 72° | 36.2 | 36.1 | 36.0 | 36.6 | 36.9 | 36.3 | 36.1 |
| 108° | 35.9 | 35.8 | 36.5 | 36.5 | 36.7 | 36.3 | 36.0 |
| 144° | 35.7 | 35.9 | 35.5 | 36.2 | 36.6 | 35.9 | 35.9 |
| 180° | 35.7 | 35.8 | 36.0 | 35.4 | 36.2 | 35.1 | 34.8 |

| | Heated annulus 3 (HA 3) | | | | | | |
|---|---|---|---|---|---|---|---|
| deg\x | 20 mm | 60 mm | 100 mm | 140 mm | 180 mm | 220 mm | 260 mm |
| -144° | 35.8 | 35.5 | 36.0 | 34.2 | 35.5 | 33.2 | 33.2 |
| -108° | 35.9 | 35.7 | 36.1 | 35.7 | 36.3 | 35.0 | 35.2 |
| -72° | 36.2 | 35.9 | 36.5 | 36.0 | 36.6 | 35.8 | 35.7 |
| -36° | | | 36.6 | 36.3 | 36.7 | 36.1 | 36.0 |
| 0° | | | 36.7 | 36.4 | 36.7 | 36.1 | 36.2 |
| 36° | | | 36.5 | 36.4 | 36.7 | 36.1 | 36.2 |
| 72° | 36.1 | 35.9 | 36.3 | 36.3 | 36.7 | 35.9 | 35.1 |
| 108° | 35.8 | 34.8 | 36.0 | 36.3 | 36.4 | 35.9 | 35.7 |
| 144° | 35.6 | 35.7 | 35.4 | 35.9 | 36.2 | 35.6 | 35.7 |
| 180° | 35.6 | 35.7 | 35.9 | 35.4 | 35.8 | 35.0 | 35.2 |

| | Heated annulus 4 (HA 4) | | | | | | |
|---|---|---|---|---|---|---|---|
| deg\x | 20 mm | 60 mm | 100 mm | 140 mm | 180 mm | 220 mm | 260 mm |
| -144° | 35.6 | 35.5 | 35.9 | 35.2 | 35.8 | 32.7 | 33.1 |
| -108° | 35.9 | 35.6 | 36.0 | 35.7 | 36.2 | 35.2 | 35.2 |
| -72° | 36.3 | 35.9 | 36.4 | 36.1 | 36.5 | 35.7 | 35.6 |
| -36° | | | 36.5 | 36.0 | 36.6 | 35.2 | 35.9 |
| 0° | | | 36.4 | 36.1 | 36.6 | 35.9 | 36.0 |
| 36° | | | 36.3 | 36.1 | 36.6 | 35.7 | 35.8 |
| 72° | 36.1 | 35.8 | 35.3 | 36.2 | 36.5 | 35.8 | 35.6 |
| 108° | 35.6 | 35.4 | 35.9 | 36.1 | 36.3 | 35.5 | 35.5 |
| 144° | 35.6 | 35.6 | 34.8 | 35.8 | 36.0 | 35.2 | 35.2 |
| 180° | 35.4 | 35.6 | 35.5 | 34.4 | 35.6 | 33.9 | 34.1 |

## Bulk fluid and wall temperatures

The graphs below show the relative temperatures inside the heat exchanger close to the inlet of the annular passage of the heat exchanger. These relative temperatures are what drive the heat exchange between the two fluids. The temperatures shown below are the bulk fluid temperature of both the annulus (blue diamond markers) and the inner tube (purple cross markers).

The other temperatures shown are the average surface temperatures as measured by the TLC (green triangle markers) and the last temperature shown is the calculated wall temperature on the annular side of tube 2, taking into account the temperature gradient over the protective resin layer (red square markers).

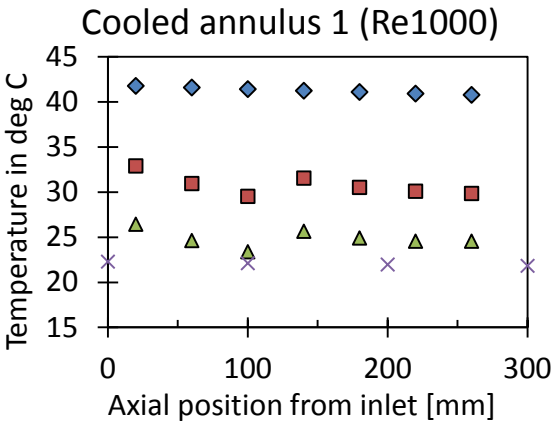


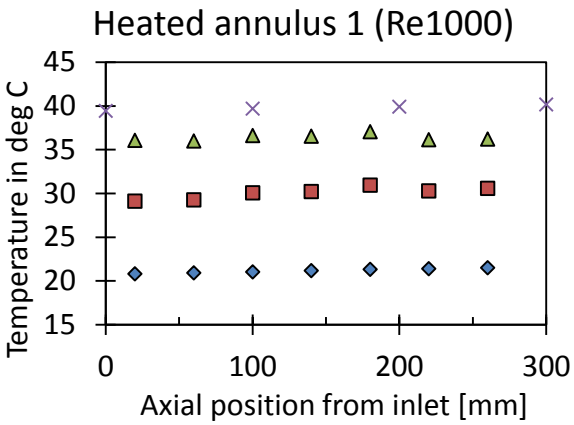


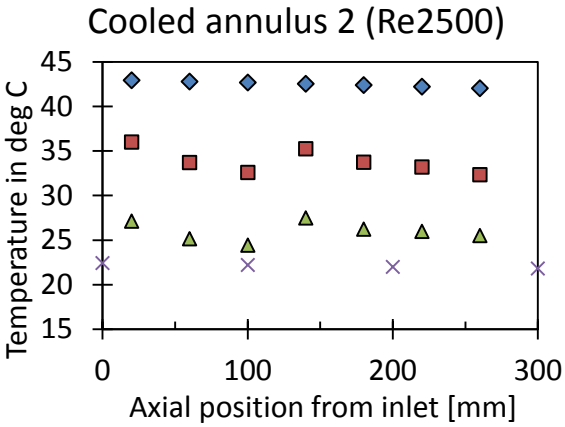


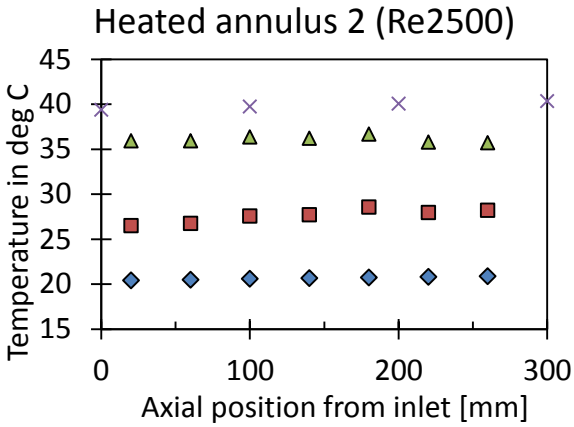


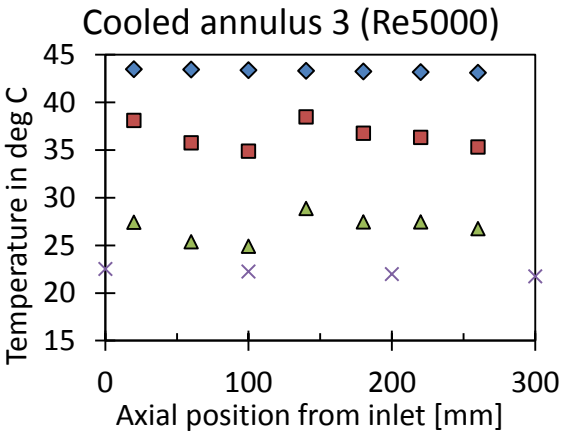


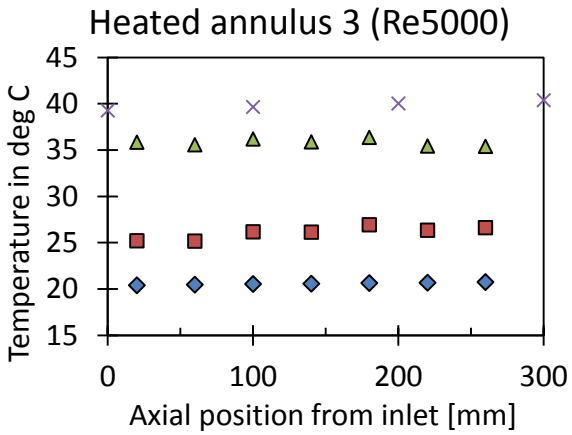

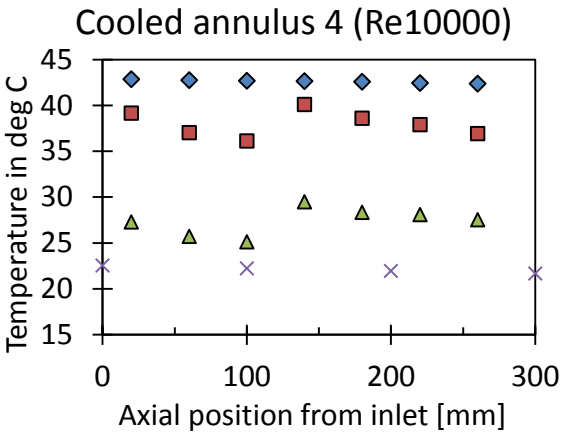


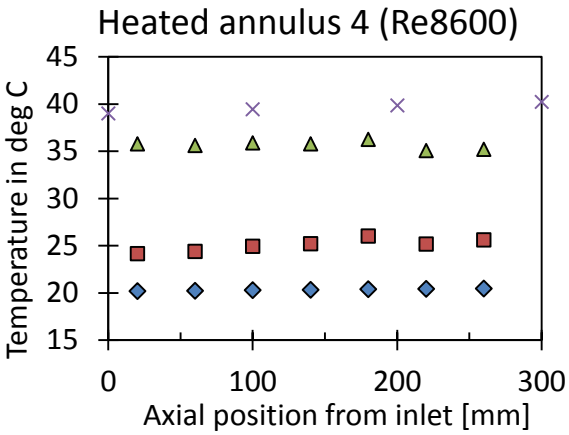


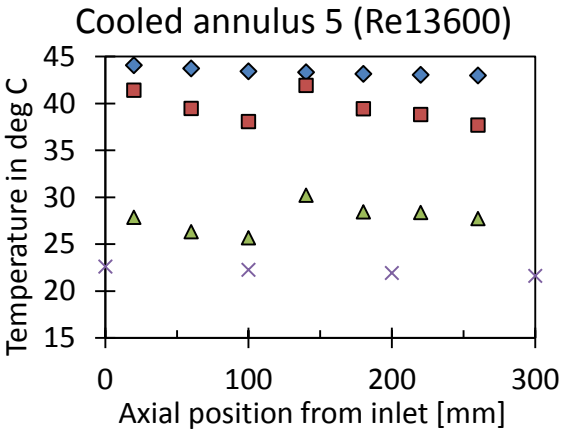


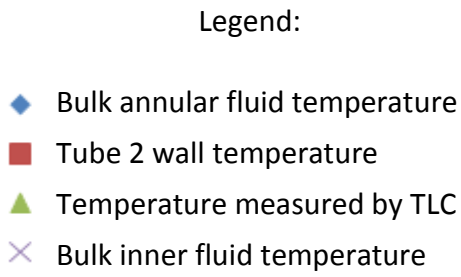


## Tube 3 – measured temperatures and associated trend lines

Displayed here are the temperatures measured at the thermocouple stations contained inside rod 3. There are eleven thermocouple stations along the length of the heat exchanger, spanning 1 m. The readings are shown in the blue diamond markers. The red triangles are the temperatures calculated from the trend line (dotted red line) fitted to the measured temperatures.

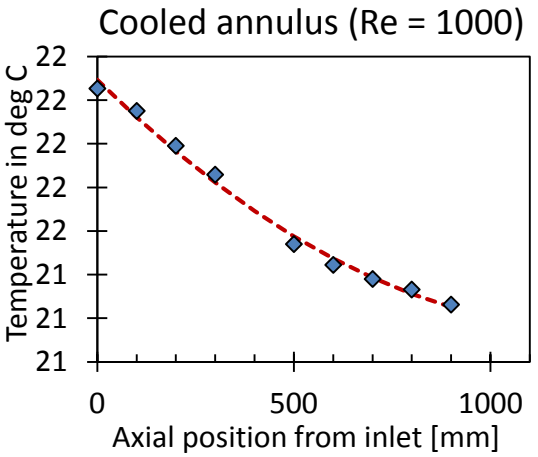


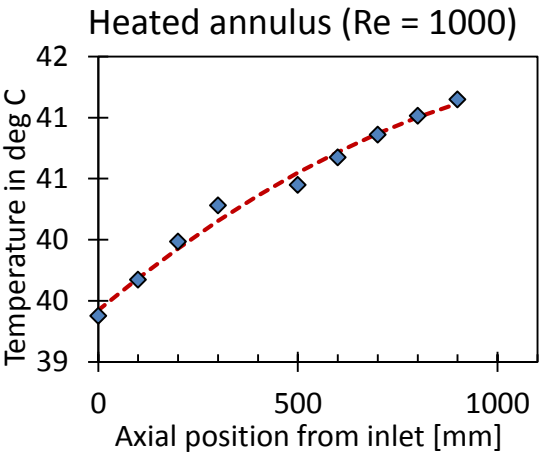

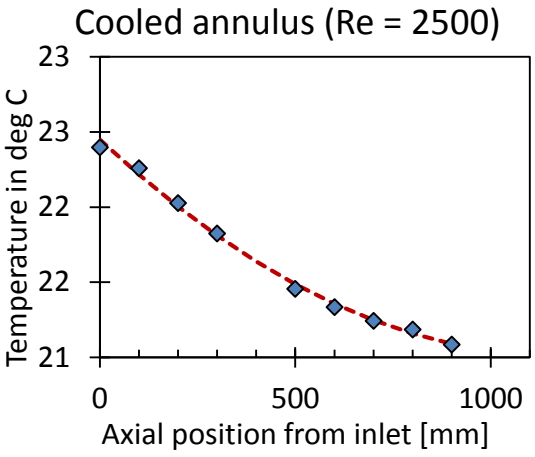


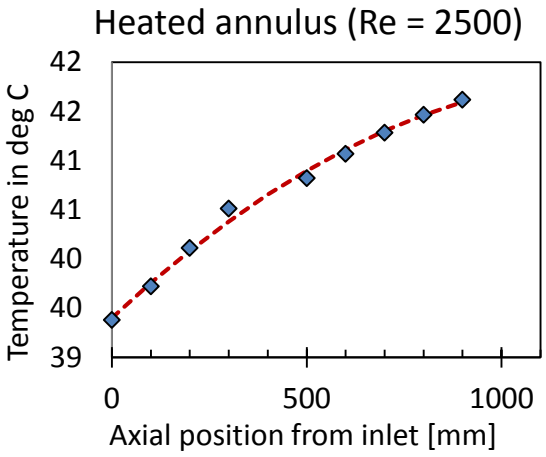


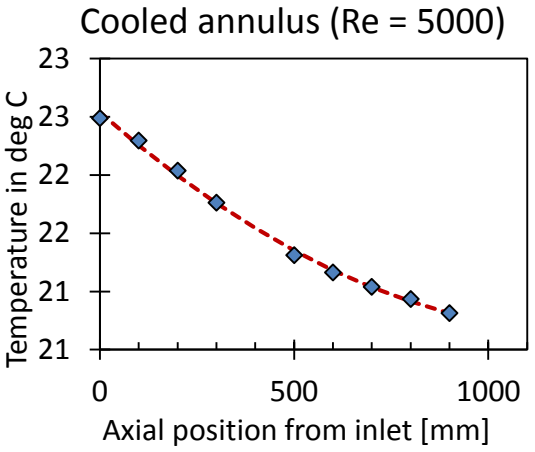


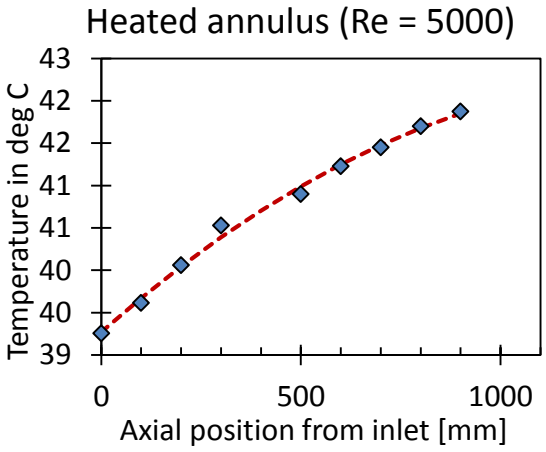


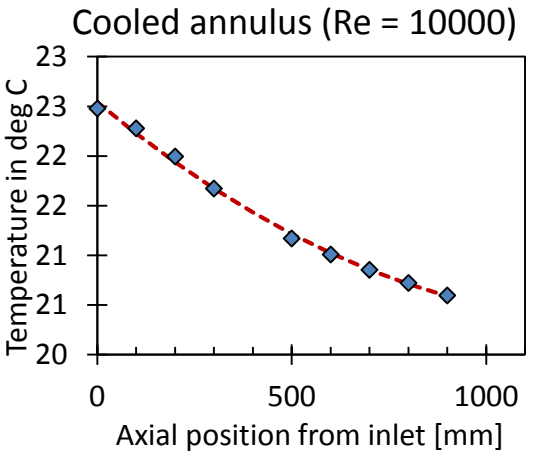


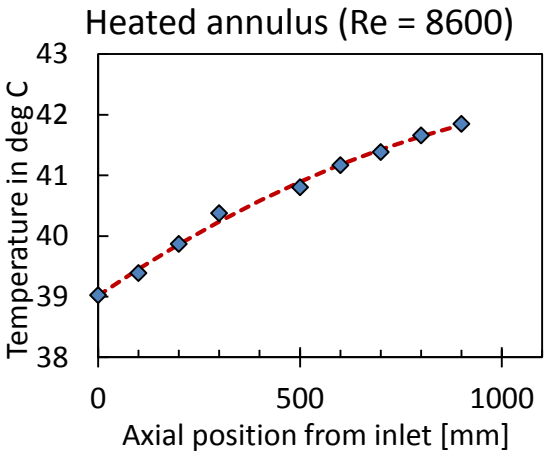

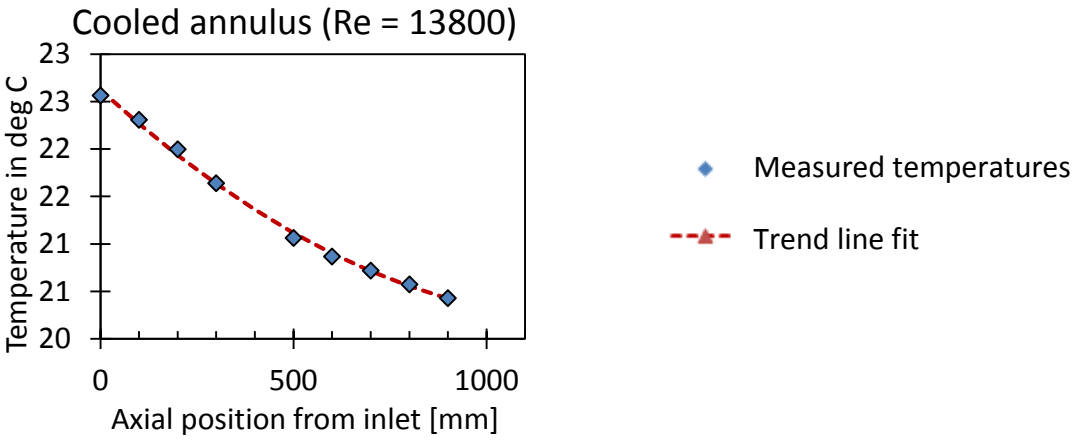

# Appendix D – Thermocouple calibration curves

This appendix presents the calibration curves for all the thermocouples used in this study. All the graphs show the temperature response for a known temperature after applying calibration. The "ideal" lines on the figures below represent a perfect thermocouple which reads exactly the temperature it is at throughout the spectrum.

## Measuring rod thermocouples

This subsection shows the calibration curves for the thermocouples used in the measuring rod of the heat exchanger. Since there were two thermocouples present at each of the measuring stations, two thermocouple calibrations are shown for each station (e.g. M 1.1 and M 1.2). The graphs below show by how much the thermocouple deviated from the PT100 measured temperature at different temperatures.

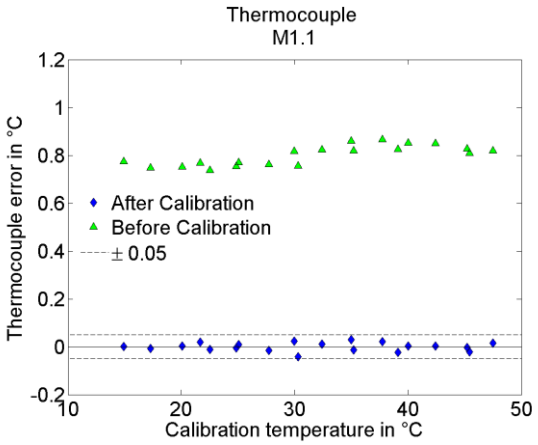


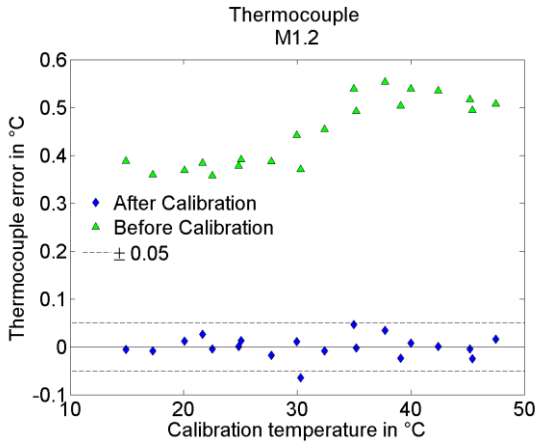


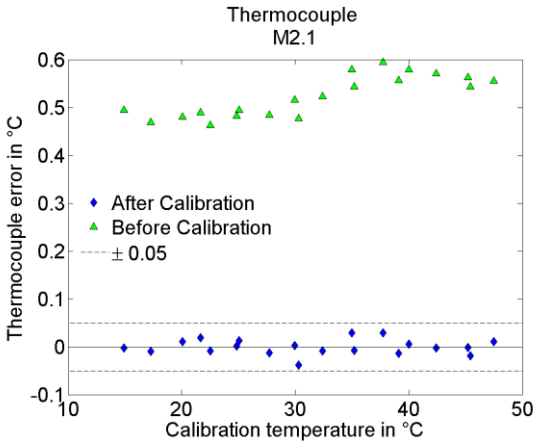


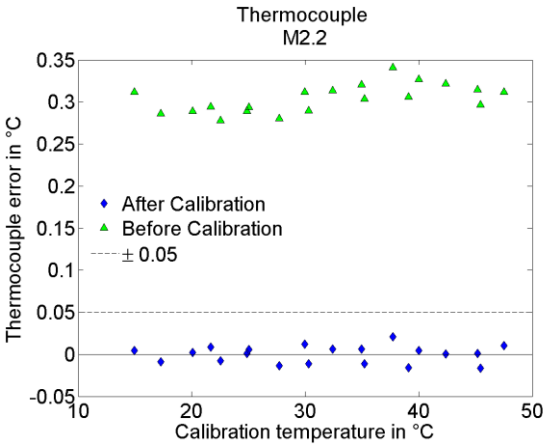

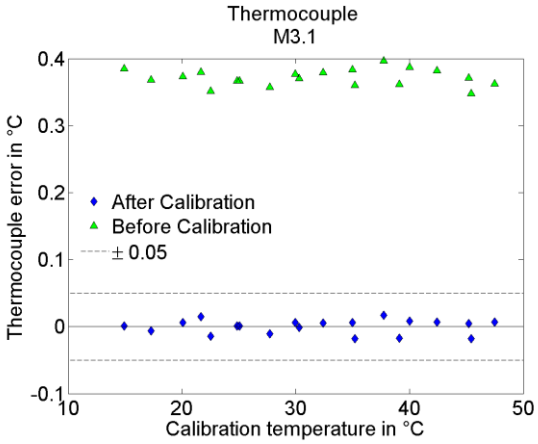


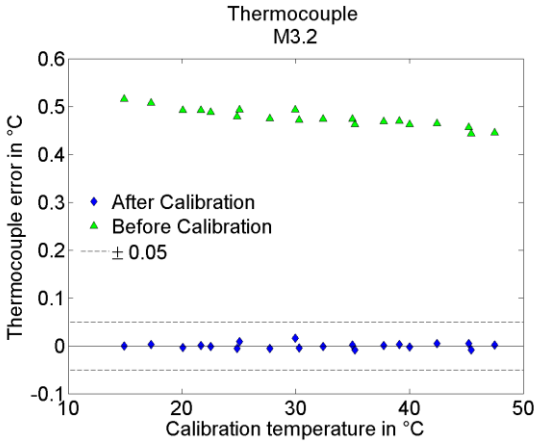


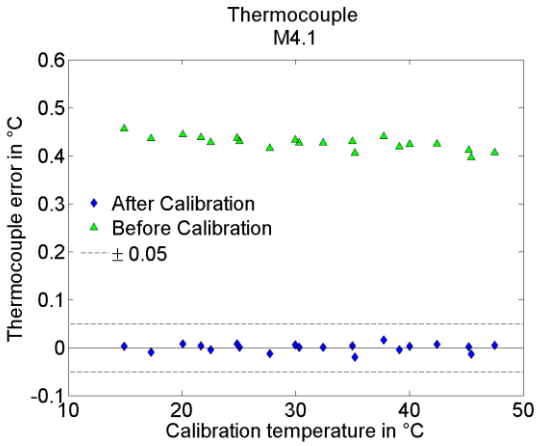


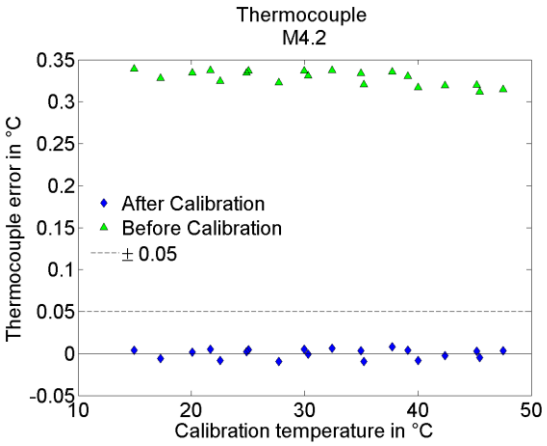


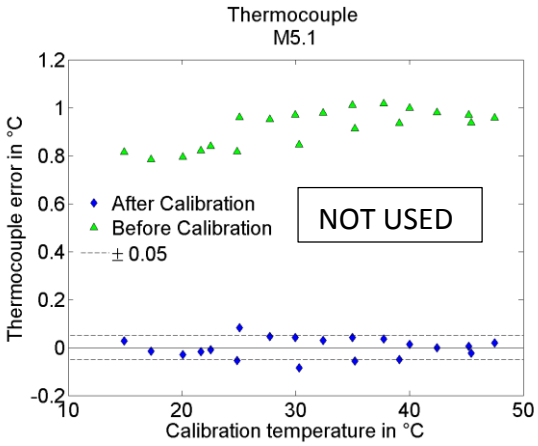


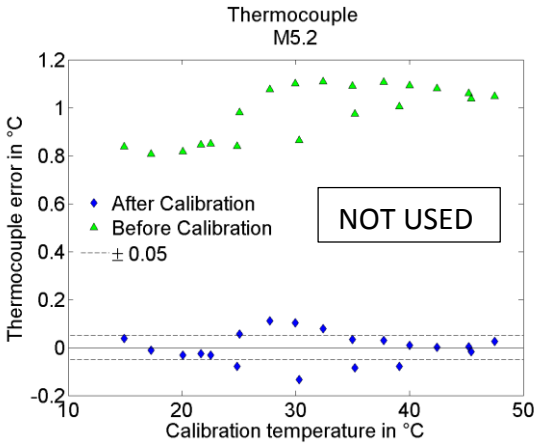

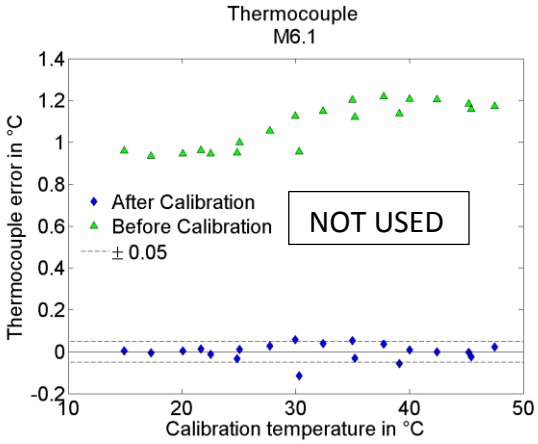


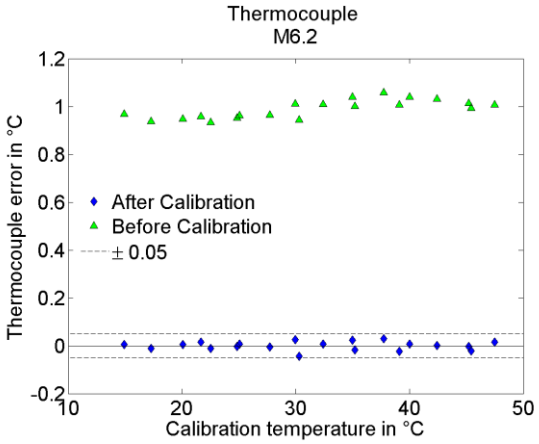


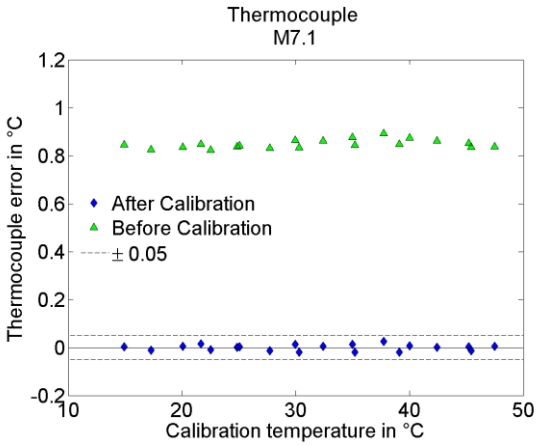


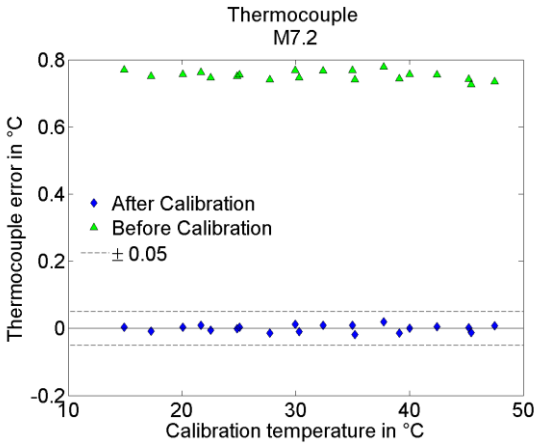


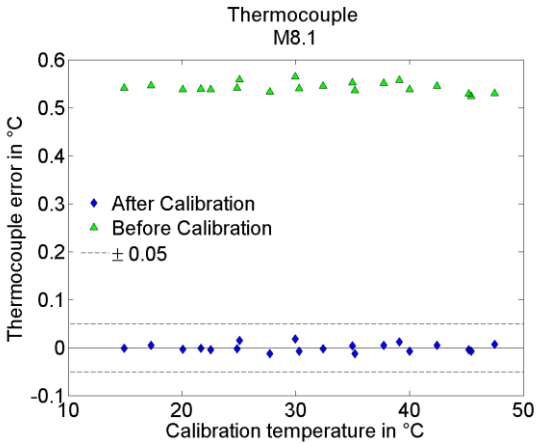


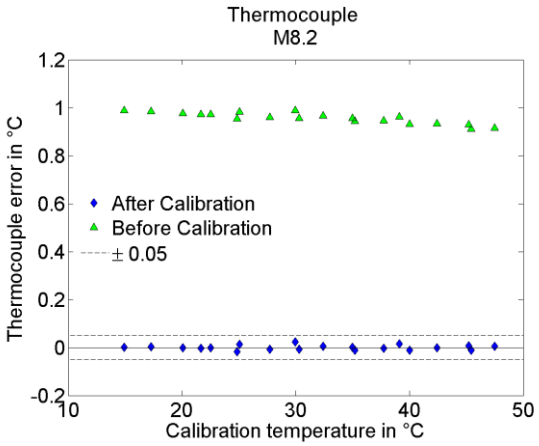

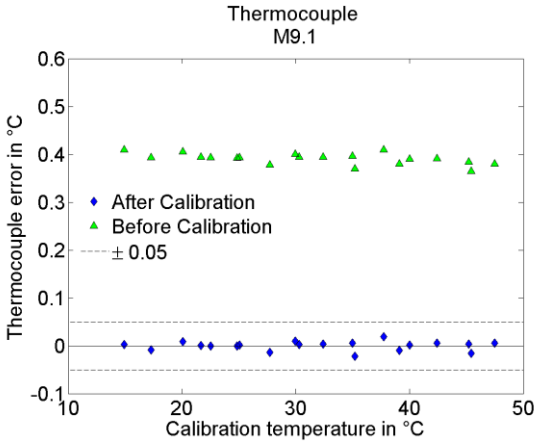


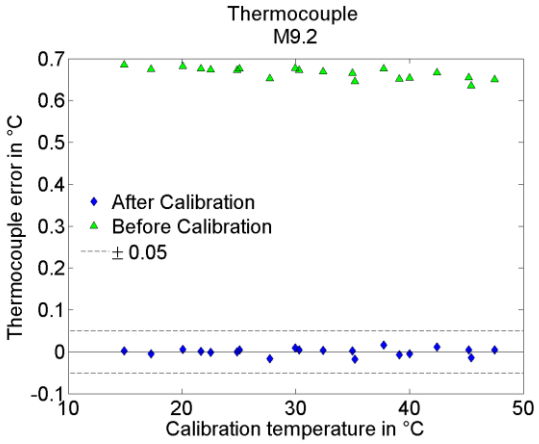


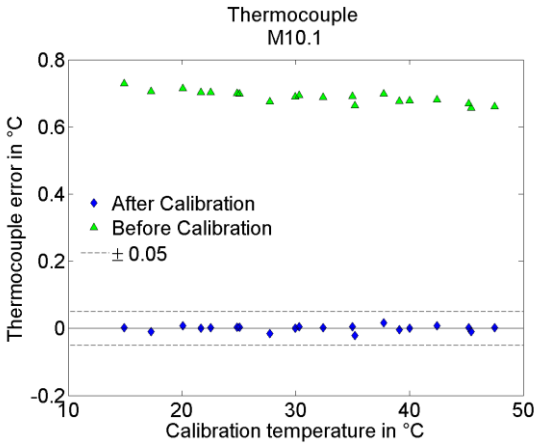


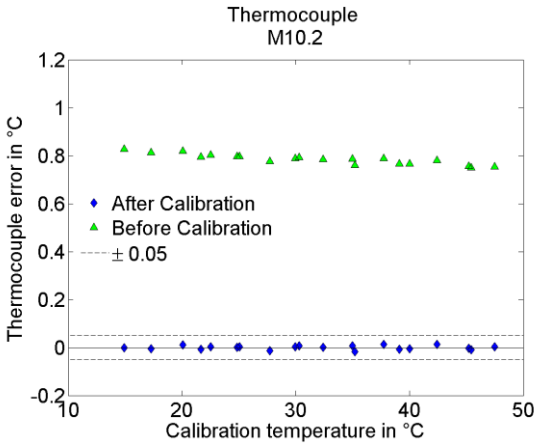


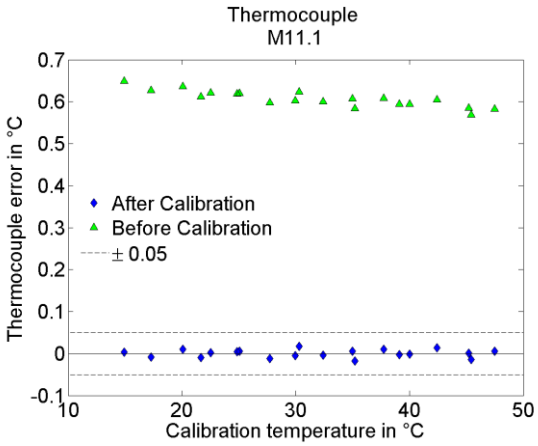


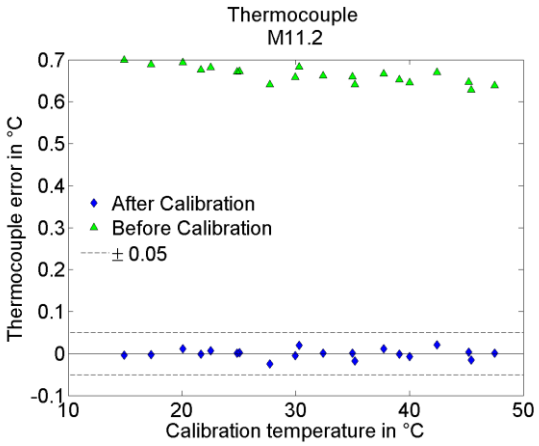

## Inlet and outlet thermocouples

Another set of 16 thermocouples were used to measure the inlet and outlet temperatures of the fluid at all the inlet and outlets. There were four thermocouples at each of the inlet and outlet positions. Each of the separate thermocouple calibration curves are shown below.

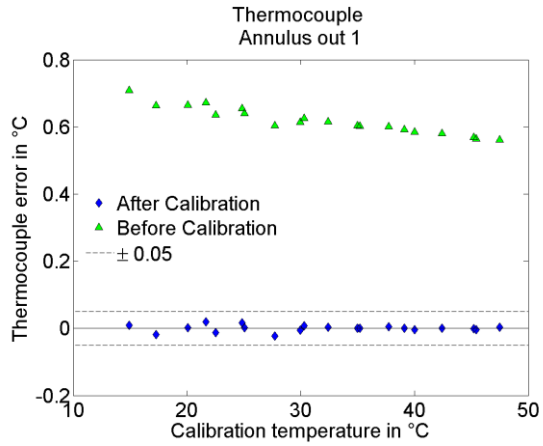


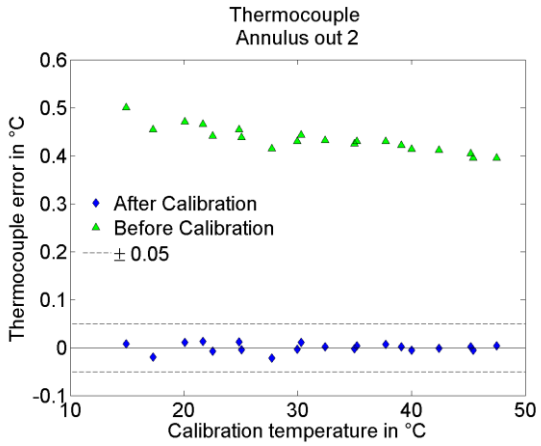


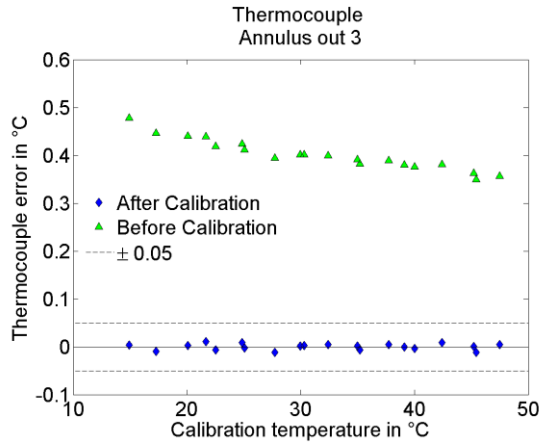


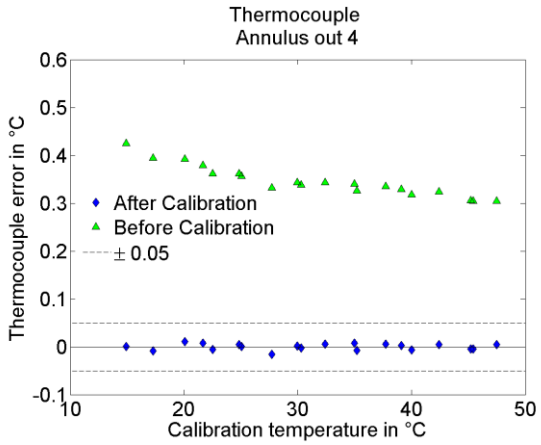


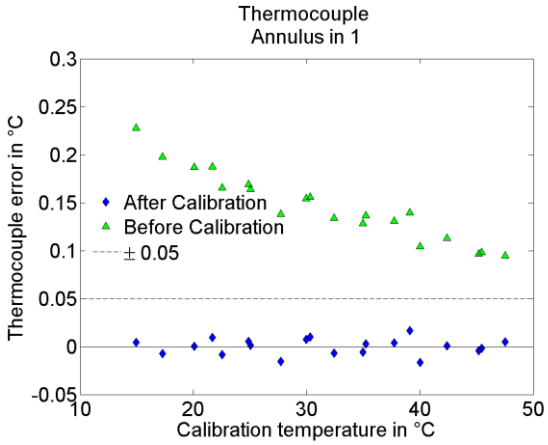


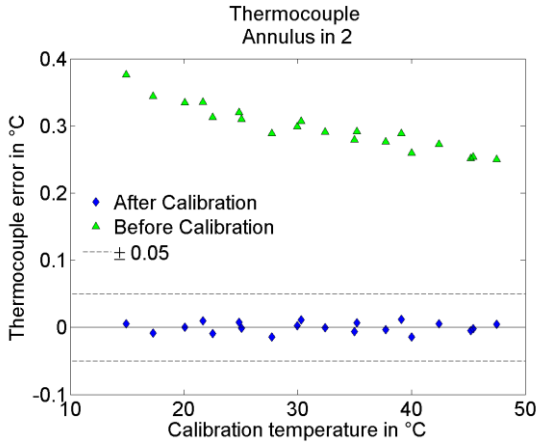

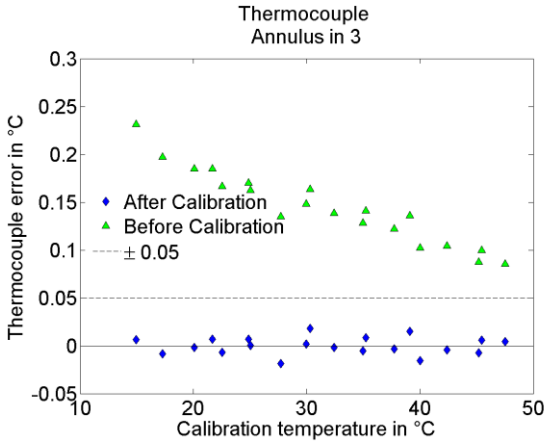


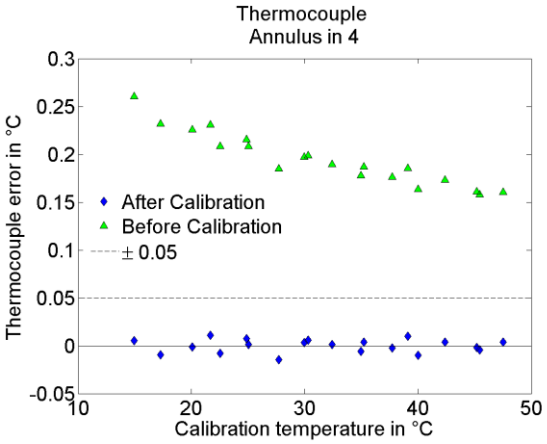


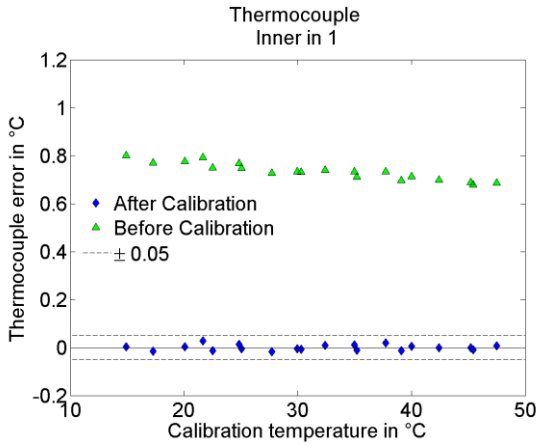


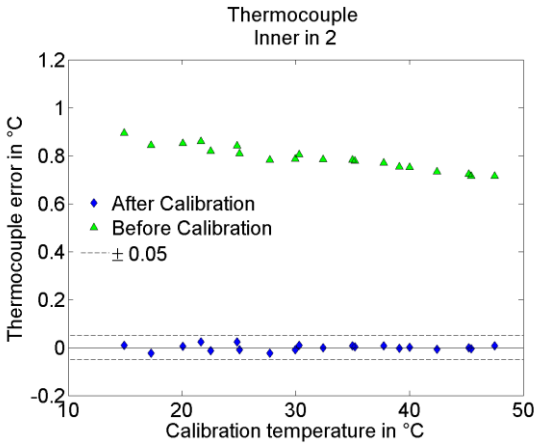


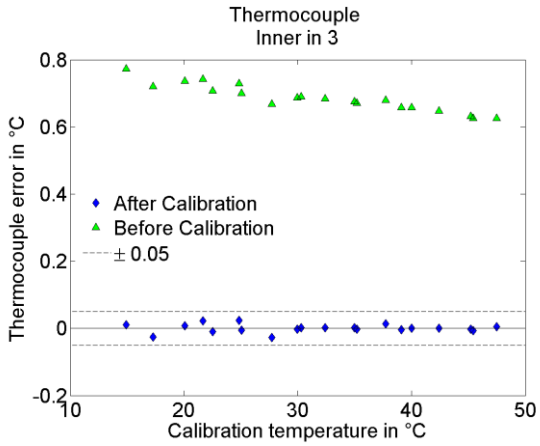


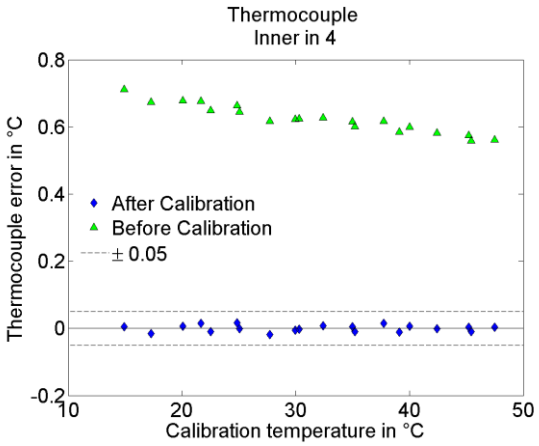

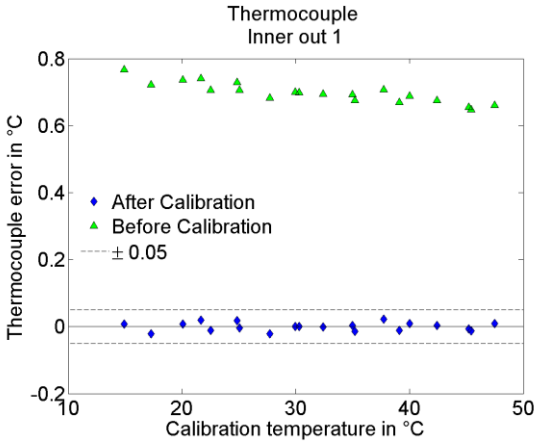


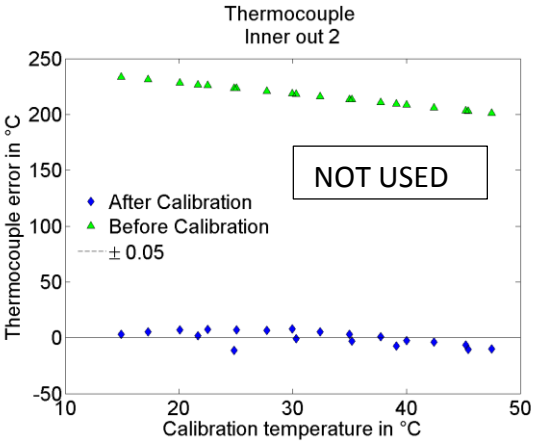


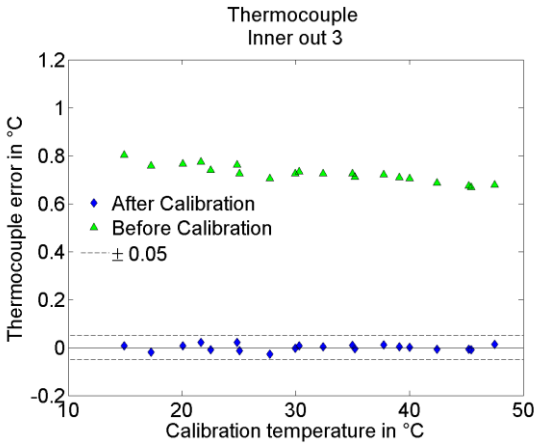


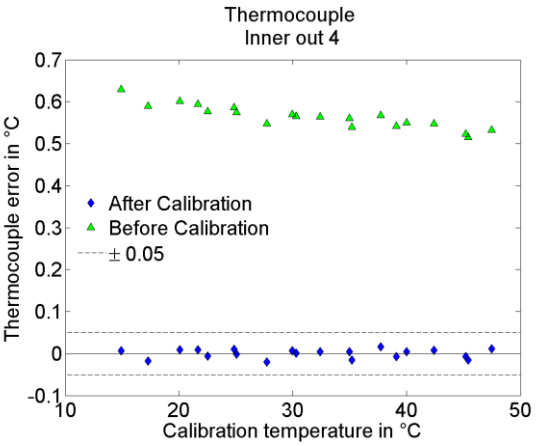

## Standard deviation of thermocouples

Perhaps a better indication of each of the separate thermocouple performance, is to observe the standard deviation of the thermocouples. This is shown below: